

Sidsel Meli Hanetho

Hybrid Aminopropyl Silane-based Coatings on Steel

Thesis for the degree of Philosophiae Doctor

Trondheim, October 2012

Norwegian University of Science and Technology
Faculty of Natural Sciences and Technology
Department of Materials Science and Engineering



NTNU – Trondheim
Norwegian University of
Science and Technology

NTNU

Norwegian University of Science and Technology

Thesis for the degree of Philosophiae Doctor

Faculty of Natural Sciences and Technology
Department of Materials Science and Engineering

© Sidsel Meli Hanetho

ISBN 978-82-471-3865-6 (printed ver.)
ISBN 978-82-471-3866-3 (electronic ver.)
ISSN 1503-8181

Doctoral theses at NTNU, 2012:276

IMT-report 2012:162

Printed by NTNU-trykk

Acknowledgements

Five years have past since I began my PhD studies, and yet it feels like yesterday. I could not have completed my PhD work had it not been for my exceptional supervisor, Prof. Mari-Ann Einarsrud. Thank you for all the encouragement, support, patience and guidance you have given me during my thesis work. The numerous times you have corrected my papers and in the end my thesis is greatly appreciated. Thank you!

During the years as a PhD student, I have also been fortunate to have Dr. Christian Simon as one of my co-supervisors. Your enthusiasm, inspiring words and your contribution to my papers is truly acknowledged. My co-supervisor Prof. Tor Grande has provided valuable thoughts to my papers and thesis, which is greatly appreciated.

Furthermore, as SINTEF has been a collaborator during my PhD, I have had the pleasure of working with and meeting many SINTEF employees. I would especially like to thank Aud M. Bouzga and Dr. Ingeborg Kaus for all the invaluable support and help you have given me. Huaitian Bu, Dr. Ferdinand Männle, Dr. Ole Øystein Knudsen, Dr. Astrid Bjørgum, Ann-Karin Kvernbråten, Juan Yang, Sivakanesar Luxsacumar, Dr. Sverre Gullikstad Johnsen and Dr. Monika Pilz are also greatly acknowledged for the numerous discussions regarding sol synthesis and coating characterization you have provided me. The assistance I have received from the technical staff in KII and Nanolab is greatly appreciated. I would also like to express my gratitude towards Dr. Lars-Erik Owe and PhD student Morten Tjelta for never hesitating with assisting me with software related issues. During my thesis work, I have had the pleasure of sharing office with Assoc. Prof. Sverre M. Selbach, Dr. Per Martin Rørvik and PhD student Ky-Nam Pham. It's been fun being your office-mate!

A good working environment is always important. Hence I truly appreciate and acknowledge all the wonderful people in KII. You have all made these years fun and inspiring!

Finally, my family and friends deserve attention for always supporting and encouraging me. Thank you for diverting my mind off the thesis, but most importantly for always being there for me.

Preface

This thesis has been submitted to the Norwegian University of Science and Technology (NTNU) in partial fulfillment of the requirements of the degree of Philosophiae Doctor.

This doctoral work has been performed at the Inorganic Materials and Ceramics Research Group, Department of Materials Science and Engineering, NTNU, Trondheim, with Prof. Mari-Ann Einarsrud as main supervisor and Prof. Tor Grande and Dr. Christian Simon, SINTEF Materials and Chemistry, as co-supervisors.

The project has been a part of the "Smoothpipe" KMB project financed by the Research Council of Norway (grant no. 180038) and the industrial partners Statoil, Total, BrederoShaw, Inpex, Tuboscope, Jotun, Carboline, 3M and AkzoNobel.

Sidsel Meli Hanetho
Trondheim, August 2012

Summary

Thin coatings applied to metals is a material-saving process to improve the surface properties such as abrasion and corrosion resistance of the substrate. Pure inorganic coatings are generally too thin to offer long-term protection, and thick coatings are prone to crack formation during processing. However, by incorporating an organic moiety, thicker and more flexible coatings can be developed. Hence sols and coatings based on 3-(aminopropyl)triethoxysilane, γ -APS, have been synthesized as part of the PhD work.

Initially, pure inorganic alkoxide-based silica coatings were fabricated. These coatings displayed poor abrasion resistance and were poor alternatives with respect to corrosion protection of carbon steel.

The need for thicker coatings was thus proposed, and hybrid inorganic-organic coatings were suggested as a probable solution. Thus in Paper I, hybrid inorganic-organic γ -APS-based sols were synthesized and characterized. Molar ratios of water (or solvent) and silane ratios and sol hydrolysis pH were varied. ^{29}Si NMR was used to study the hydrolysis and condensation reactions. The kinetic mechanisms of the hydrolysis and condensation of the sols showed a difference in the structures formed depending on the water/silane ratio and the sol pH. Increasing the water/silane ratio promoted a faster condensation reaction as evidenced by the early evolution of more condensed species. Reducing the sol pH enabled the condensation reaction to slow down thus facilitating a more complete hydrolysis reaction. Furthermore, hypostoichiometric sols were shown to consist of linear structures while stoichiometric and hyperstoichiometric sols were more cross-linked as evidenced by the higher viscosity and the combination of T^2 and T^3 species detected by ^{29}Si NMR.

In Paper II, coatings were fabricated from the sols described in Paper I. Transparent and homogeneous hybrid aminopropyl silane-based coatings on steel were prepared by the sol-gel method using the hydrolyzed γ -APS sols as precursors. The coatings were fabricated by dip coating, and the effect of pH, water/silane ratio and solvent/silane ratio during the coating process was investigated with respect to thermal stability, coating thickness, roughness, porosity, contact angle and abrasion resistance. The thickness of the coatings varied between 0.17 and 4.1 μm and was controlled by the preparation conditions of the sol as well as the viscosity of the sols. The coatings were in general smooth and the roughness in the order of a few nanometers. The contact angles with water of the coatings varied from 60 to 80 $^\circ$. Organic pentadecane was shown to wet the coatings, which suggested that the coatings also displayed hydrophobic properties. The abrasion resistance improved with decreasing pH of the water used during hydrolysis of the silane. The coatings were characterized with respect to delamination and smearing. Thicker coatings

were delaminated while thinner coatings were smeared and displayed lubricating properties. Gels of the hybrid aminopropyl silane-based sols were thermally stable up to 350 °C, and the gels displayed a low pore volume and a low surface area.

In Paper III, hybrid aminopropyl silane-based sols with a variation in the molar ratios of water and silane, the molar ratios of solvent and silane and pH, were applied as a bond coat to carbon steel substrates. Fracture strength, abrasion resistance and electrochemical polarization studies have been conducted on these bond coats. Furthermore, the bond coats were applied a top coat consisting of a polyaspartic paint, and the combination coatings were subsequently exposed to an ageing resistance test for 5 weeks. The bond coat-top coat combination coatings were demonstrated to significantly improve the corrosion protection behavior of carbon steel. The thickness of the bond coats varied from 0.35 to 4.1 μm , while the bond coat-top coat combination coatings were all in the range of 100 μm .

Contents

Acknowledgements	iii
Preface	v
Summary	vii
The author's contribution	xi
1 Background	1
2 Aim of the work	5
3 Introduction	7
3.1 Sol-gel synthesis	7
3.1.1 Silica alkoxide system	8
3.1.2 Hybrid inorganic-organic systems	14
3.2 Dip coating	22
3.3 Drying of coatings	24
3.4 Corrosion protection of steel	28
3.4.1 Conventional corrosion protection of steel	28
3.4.2 Novel hybrid inorganic-organic materials as anticorrosive coatings	28
3.4.3 Summary of corrosion protective capability of hybrid inorganic-organic silane-based coatings	30
3.5 Prevention of wax deposition	31
3.5.1 Conventional means of wax removal	31
3.5.2 Build-up of wax layer	31
3.5.3 Surface modification with hybrid inorganic-organic silane-based coatings	33
3.5.4 Important parameters for prevention of wax deposition	33
4 Extended summary of the work	35
4.1 Preliminary studies	35
4.1.1 Alkoxide-based silica coatings	35
4.2 Structure of the hybrid aminopropyl silane sols	37
4.3 Rheological properties of the hybrid aminopropyl silane-based sols	47
4.4 Coating thickness of the hybrid aminopropyl silane-based coatings	48

4.5	Physical properties of the hybrid aminopropyl silane-based coatings .	50
4.6	Abrasion characterization of the hybrid aminopropyl silane-based coatings	53
4.7	Corrosion protection of hybrid aminopropyl silane coatings on carbon steel	55
4.7.1	Electrochemical polarization studies	55
4.7.2	Ageing resistance studies	57
4.7.3	Summary of the corrosion protective properties of the hybrid aminopropyl silane-based coatings	59
4.8	Prevention of wax deposition by hybrid aminopropyl silane-based coatings	59
5	Conclusions	61
6	Outlook	63
7	References	65
Papers		79
	Paper I: Structural Characterization of Hybrid Aminopropyl Silane-based Sols	80
	Paper II: Synthesis and Characterization of Hybrid Aminopropyl Silane-based Coatings on Stainless Steel Substrates	94
	Paper III: Corrosion Protective Aminopropyl Silane-based Coatings on Carbon Steel	120
Appendix		133
	Paraffin Wax Deposition Studies on Coated and Non-Coated Steel Surfaces	134

The author's contribution

The author wrote Papers I-III, while the Appendix was mainly written by Sverre Gullikstad Johnsen (SINTEF). The author has conducted most of the laboratory and characterization work except the nuclear magnetic resonance spectroscopy (NMR) experiments, the ageing resistance tests and the wax deposition study. Most of the sols characterized by NMR were synthesized by the author, but the NMR experiments (Paper I) were conducted by Aud M. Bouzga (SINTEF). Furthermore, all the sols for the ageing resistance tests (Paper III) were prepared by the author, but the dip coating of the sols onto carbon steel substrates was performed by Luxsacumar Sivakanesar (SINTEF), while Ann-Karin Kvernbråten (SINTEF) conducted the ageing resistance experiments. The wax deposition study (Appendix) was conducted by Sverre Gullikstad Johnsen, while the author fabricated the sol and deposited it on carbon steel substrates by dip coating.

Chapter 1

Background

The oil production on the Norwegian continental shelf has throughout the last 40 years contributed with approximately 9000 billion Norwegian kroner to the Norwegian GNP [1]. In 2010 alone, the petroleum sector contributed to 21 % of the nation's added value. Norway is the 7th largest exporter and the 14th largest producer of oil in the world, and in 2010 Norway ranked as the world's 2nd largest exporter and the 7th largest producer of natural gas. There are currently 70 operational oil fields on the Norwegian continental shelf, which in total produced more than two million oil drums per day in 2011.

Crude oil is composed of paraffins, aromatics, naphthenics, resins, asphaltenes and other impurities such as gas hydrates [2, 3]. In subsea installations, the crude oil/fluid initially has a high temperature when extracted, but the pipeline used for transportation of crude oil is cooled down by seawater and the sea bed [2, 4]. The pressure drop and the temperature change along multiphase pipelines are the main obstacles to transportation of unprocessed or partly processed oil wellstream over long distances. Several parameters contribute to the pressure drop, e.g. surface roughness, liquid hold-up, precipitations and gas-liquid drag forces. The temperature change greatly affects the precipitation of wax as the solubility of the paraffins in the crude oil is reduced with decreasing temperature, and the wax precipitates at the wax appearance temperature (WAT), which is lower than the bulk fluid temperature [5]. Precipitation and deposition may decrease the effective inner diameter of the pipe, as well as increasing the surface roughness. The most important precipitations are wax, hydrates, asphaltenes and scale, depending on properties of the fluid, pressure and temperature [6]. Wax deposition occurs on the internal surface of a subsea flowline when the pipe wall temperature falls below the WAT of a paraffinic hydrocarbon liquid [7].

The wax is composed of high-molecular weight paraffins, and the paraffins can be further distinguished into linear and slightly branched alkanes (n-alkanes, isoalkanes and naphthenes) with a carbon number between 20 and 60 [8]. The WAT depends on the paraffin distribution in the crude oil.

So far, the wax deposition problem has been dealt with by mechanical removal, addition of chemicals or by thermal insulation of the pipeline [7, 9]. However, for long pipelines such solutions are very costly, and other solutions are sought.

Corrosion of the pipeline is also a serious problem causing increased roughness

of the surface. Phosphate or chromate conversion treatments have been widely used in the corrosion protection of steels [10–12]. However, due to the toxicity of chromium and its salts, an extensive search for alternative methods to prevent corrosion has been initiated. Furthermore, silane-based inorganic-organic coatings have shown improved protection ability of steel [10, 13–15]. These types of coatings could thus be good candidates with respect to corrosion protection and prevention of wax deposition in pipelines.

Degradation of the pipeline is problematic for subsea transportation of crude oil. Possible degradation mechanisms are outlined in Figure 1.1, which describes two plausible scenarios; material can either be removed from the pipeline (corrosion and particle impact) or material can deposit on the surface of the pipeline (wax precipitation, particle adsorption or oil adsorption). Whereas the latter mentioned mechanisms will decrease the inner diameter of the pipeline, corrosion and particle impact will result in a significant increase in the pipeline roughness. Figure 1.1 thus illustrates the need for protection of the pipeline from mechanical and chemical attack.

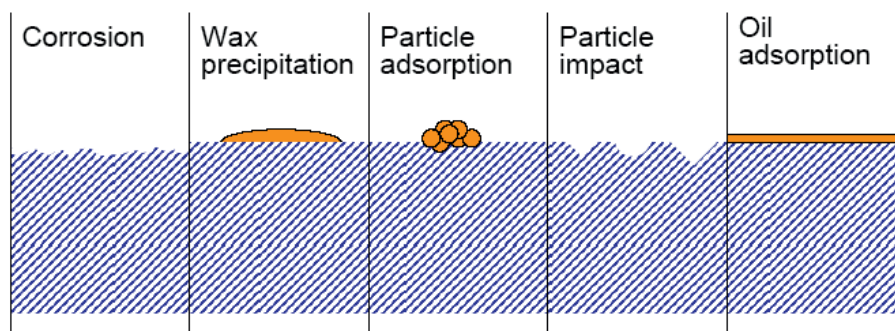


Figure 1.1: Illustration of the inner surface of a pipeline after use demonstrating five different possible scenarios leading to a change in surface roughness and degradation of the pipeline.

Coatings are used to protect and improve properties of materials like metals, plastics and glass. Parameters such as coating thickness, porosity, morphology, surface roughness, chemical (e.g. corrosion), mechanical (e.g. abrasion) and electrical properties can be designed to cover a wide range of applications [16, 17].

The sol-gel method is a cost-efficient, low temperature synthesis route, which can be used to fabricate coatings [18, 19]. The synthesis method allows molecular control of the composition. The use of alkoxide precursors enables control of hydrolysis and condensation, which densifies the coating structure. Furthermore, silica-based alkoxides have the possibility of functionalization, which implies unhydrolyzable organic groups with particular properties such as a specific surface tension, carbon number (the number of carbon atoms in a molecule), hydrophobicity, polarity, etc. Thus material properties of the coatings such as hydrophobicity and density can be optimized.

This PhD work has been a part of SINTEF's Smoothpipe project [20], which originated in order to define and solve problems associated with wax deposition during transportation of crude oil. The project has consisted of five parts, referred to as Part 1-5. A plausible solution to the problem was to fabricate smooth coatings, which this PhD work (Part 4) has been attempting to achieve. Furthermore, it was also suggested that Smoothpipe would work towards understanding the mechanisms involved in wax deposition in multiphase pipelines, such as the effect of flow shear stress, cooling rate, deposit morphology, etc., as a function of coating properties (Part 1-3, 5). It was also deemed important to study the corrosion protective properties of the smooth coatings (Part 4), and to obtain an understanding of the degradation mechanisms of the coatings (Part 3). Another aspect of the project was to investigate the possibility of tailoring already commercial paints with the use of nanosized particles and capsules (Part 4, but conducted by SINTEF).

Chapter 2

Aim of the work

The main goal of this study was to prepare hybrid inorganic-organic coatings with good adhesion to steel substrates, which displayed anti-adhesive properties towards wax and which were able to protect the steel against corrosion. Furthermore, the overall goal was divided into several sub-goals where the first sub-goal concerned the synthesis of the coatings. As a first approach, pure inorganic alkoxide-based silica sols were synthesized using the sol-gel method. However, these coatings were shown to provide inadequate protection against corrosion, and a new approach based on hybrid inorganic-organic sol-gel synthesis was commenced. SINTEF [21] had previously been able to synthesize stable and translucent hybrid aminopropyl silane-based sols by the sol-gel method. Thus this PhD work set forth to fabricate and evaluate the potential use of the hybrid aminopropyl silane-based sols as coatings on steel. The hybrid aminopropyl silane-based sols were structurally characterized (Paper I), whereupon the feasibility of sol application by dip coating was studied along with the potential use of the hybrid sols as coatings on steel was investigated (Paper II). Abrasion and hydrophobic properties of the coatings were evaluated. Finally, the corrosion protective properties were identified (Paper III). Since one of the objectives of the work was to investigate the ability of the coatings to withstand wax deposition, simulation of the wax deposition process was conducted in collaboration with SINTEF (Appendix).

Chapter 3

Introduction

3.1 Sol-gel synthesis

There are several excellent reviews regarding the sol-gel chemistry [19,22], and only a short summary is presented here. The sol-gel method is a low temperature synthesis route used to produce homogeneous materials with a high purity [19,23]. The sol-gel method generally constitutes a hydrolysis and condensation step whereupon the network structure develops. The sol-gel method uses precursors, which allow the formation of complex and homogeneous shapes [18]. The resulting structures vary greatly in physical appearance, composition and application as illustrated in Figure 3.1. Figure 3.1 (a) illustrates the fabrication of a thin coating on a substrate by sol-gel synthesis of an alkoxide precursor. At first, the sol is hydrolyzed and polymerized whereupon a polymer-like structure develops. The sol is then deposited on a substrate and gelled as the coating is formed. Owing to the resilience of the sol-gel route, the coating can be thin or thick, dense or porous, etc., and the chemical and mechanical properties can be tailored by altering the sol parameters. For instance, dispersions consisting of rough colloids can also be used as precursors (Figure 3.1 (b)). The sol-gel method enables the fabrication of e.g. aerogels with specific physical properties such as pore size. Another possible sol-gel synthesis approach involves the use of a smooth colloidal dispersion (Figure 3.1 (c)), which allows microstructural control of pore size due to the uniform and homogeneously dispersed colloids. Thus dense ceramics can be obtained. The versatility of the sol-gel method further allows reaction products, which have a specific particle size, morphology, density and viscosity [22,24,25]. The reaction parameters can easily be controlled allowing the application of the sol to different kinds of substrates [26,27].

The precursor solutions used for sol-gel synthesis generally consist of either (i) non-network forming metal ions in solution (inorganic approach) or (ii) network-forming polymers in solution (organic approach) [18,19]. The non-network forming metal ions have low solubility in water, and the solubility is usually enhanced by the addition of a complexing agent. The network-forming polymer solutions predominantly contain hydrolyzed alkoxides dissolved in alcohol solution, but aqueous oxide solutions can also be used [19,29,30].

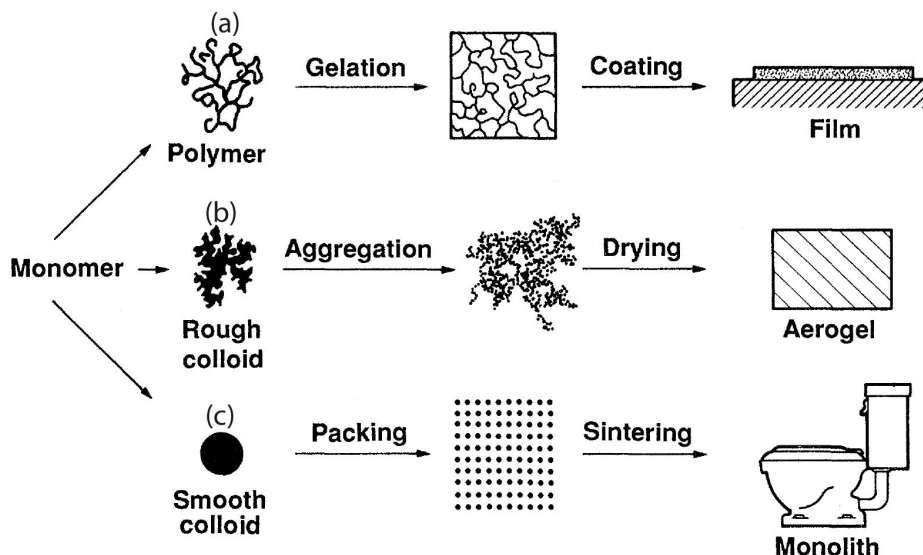


Figure 3.1: Sol-gel route illustrating the ease of making porous gels, dense ceramics and thin, dense films [28]. Examples showing (a) formation of a coating, (b) aerogel formation and (c) fabrication of a dense ceramic material.

3.1.1 Silica alkoxide system

Background

Early in the 1950's, Aelion et al. [31] studied the hydrolysis of tetraethoxysilane (TEOS), and they discovered that strong acidic or basic catalysts affected the reaction kinetics of TEOS, and hydrolysis was promoted at acidic pH. Immiscibility between water and TEOS had been known for some time, and thus the need for a mutual solvent was mentioned. The polymerization reaction of monosilicic acid was further studied by Alexander [32] in 1953 by using a freezing point method. At low pH, polymerization of monosilicic acid was found to be of third order while at higher pH, the polymerization was proposed to follow a second order reaction rate and to depend on the number of functional groups. In addition, Iler [33] has also greatly contributed to the understanding of silica chemistry. Furthermore, Brinker et al. [34, 35] studied a two-step sol-gel synthesis route with either acid- or base-catalysis of TEOS and were able to relate the reaction rate of hydrolysis to the gel structure that formed by using small angle x-ray scattering (SAXS) as characterization technique. The first step (acid and water) resulted in a wide distribution of silane species, while the second step (acid and water or base and water) resulted in completely hydrolyzed and highly condensed polymers in an acidic sol, while the base-catalyzed sol yielded incomplete hydrolysis and less condensed polymers. Pouxviel et al. [36] and Vega and Scherer [37] studied acid-catalyzed TEOS at varying molar ratios of TEOS and water by using ^{29}Si nuclear magnetic resonance (NMR) spectroscopy. Their findings disclosed a great effect of pH on the hydrolysis rate,

which confirmed the results obtained by Aelion et al. [31] and Brinker et al. [34, 35]. Chen et al. [12] further studied the effect of changing the chain length of the alkoxy groups, and they discovered increased reaction rates with decreasing alkoxy chain length, which they ascribed to a difference in concentration due to the specific volumes of the starting compounds. To sum up, previous research has identified the important sol parameters, which will affect the formed structure to be the type of alkoxide and its functionality, the choice of and pH of catalyst (acidic or basic), the molar ratio of water and alkoxide and the reaction temperature [38–40].

Synthesis of silica alkoxide sol

Silica sols can be synthesized using the sol-gel route, and most often silicon alkoxides, such as tetramethoxysilane (TMOS) and tetraethoxysilane (TEOS, $\text{Si}(\text{OC}_2\text{H}_5)_4$), are used as precursors [36].

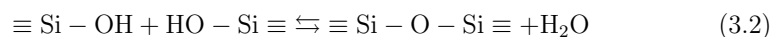
The reaction types involved in sol-gel synthesis of TEOS are hydrolysis and condensation as depicted in Equations 3.1, 3.2 and 3.3, in which OR represents an alkoxy group. It is generally accepted that hydrolysis occurs via an $\text{S}_{\text{N}}2$ reaction mechanism with a pentacoordinated Si as the intermediate species and ROH as the leaving group, which is simplified in Equation 3.1.

Hydrolysis [22]:

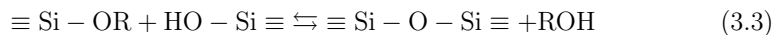


Furthermore, the condensation reactions (Equations 3.2 and 3.3) can follow two different routes which either produces water or alcohol (solvent).

Water producing condensation:



Alcohol producing condensation:



Alkoxides and water are immiscible liquids, and thus phase separation occurs [22]. A common solvent, which is usually the parent alcohol, is therefore chosen as homogenizing agent [22, 31, 41]. The miscibility of TEOS in ethanol and water is shown in the ternary phase diagram displayed in Figure 3.2. The phase diagram shows the area of miscibility, which dictates the amount of solvent needed for a given concentration ratio of water and alkoxide, in order to prevent phase separation.

Even though Figure 3.2 shows a large area of immiscibility, it is still possible to manufacture transparent sols and gels within this area because miscibility can

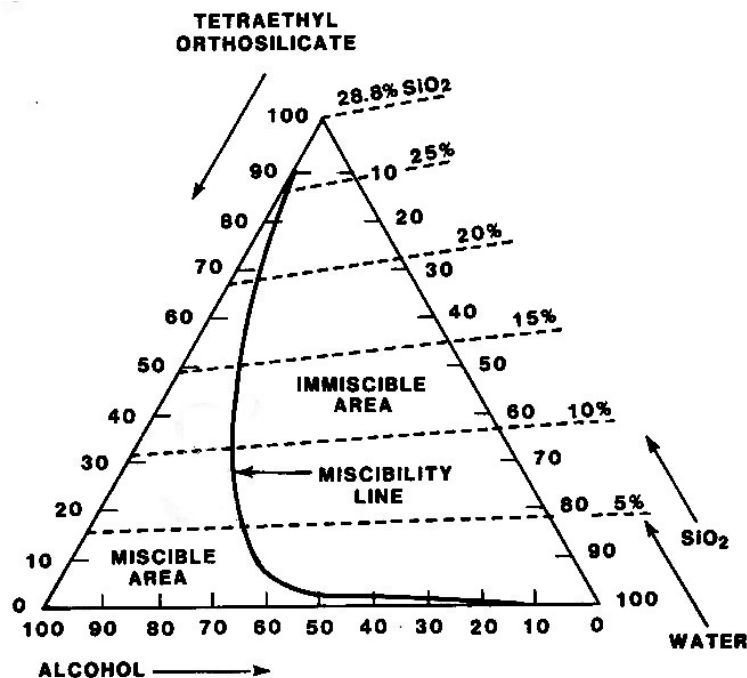


Figure 3.2: Ternary phase diagram for tetraethoxy silane (TEOS), water and alcohol showing the miscible and immiscible regions of TEOS in water [22].

be triggered by prolonged reaction time at an elevated temperature. Equation 3.1 explains how this is possible. As the reaction proceeds, an increasing amount of solvent (ROH) will be produced. The solvent will thus increase the solubility and shift the equilibrium to the right in Equation 3.1. Furthermore, condensation reactions will either produce water or solvent as shown in Equations 3.2 and 3.3, respectively. Whereas the water producing condensation reaction will reduce the solubility, the alcohol producing will, similarly to hydrolysis, increase the solubility. It is generally accepted that the water and alcohol producing condensation reactions occur for water/silane ratios below or above 2, respectively.

The hydrolysis and condensation rates of TEOS are presented in Figure 3.3, which clearly shows hydrolysis as the dominant reaction at low pH while condensation governs at high pH due to increasing solubility of silica [22]. The reaction rates are comparable in the pH range of 4-5. Hydrolysis is governed by protonation or deprotonation of the silanols (alkoxide group). At acidic pH, the hydrolysis reaction is fast due to protonation of silanols. Increasing the pH results in a mixture of deprotonated and protonated silanols as deprotonation is facilitated at higher pH. Furthermore, at pH 7, the hydrolysis rate is the lowest owing to the fact that the concentrations of protonated and deprotonated silanols are equal. At higher pH, the amount of deprotonated silanols exceeds the amount of protonated silanols, and the hydrolysis rate is seen to increase. Similarly, the condensation rate exerts a maxi-

mum around pH 7 due to the presence of both protonated and deprotonated silanols. Moreover, the condensation rate is also linked to the dissolution rate of silica. As a result of the solubility, the silica condensation occurs by a cluster-cluster aggregation at low pH (low solubility), while at higher pH monomer-cluster aggregation prevails due to more available monomers [42].

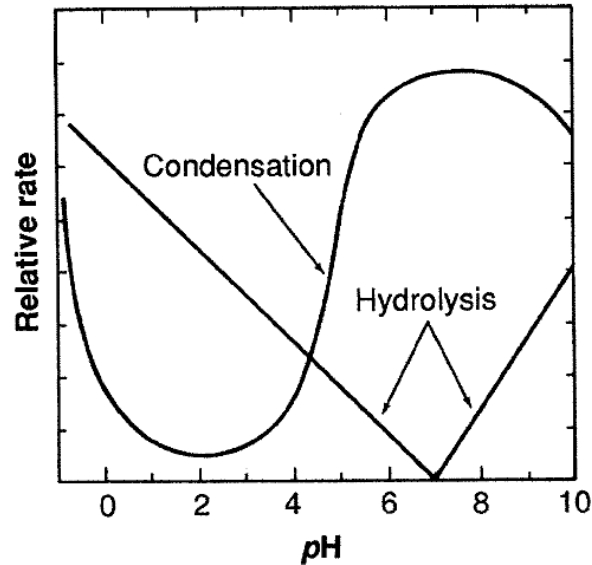


Figure 3.3: Schematic comparison between the rates of hydrolysis and condensation of silicon alkoxide solutions as a function of pH [22, 28].

The effect of pH on the reaction kinetics is further shown in Figure 3.4. The hydrolysis of an acid-catalyzed silicon alkoxide reaction is fast whereas at base-catalyzed conditions the condensation reaction predominates. The resulting gel network of either of these catalysis conditions is also outlined in Figure 3.4. Acid catalysis generates linearly chained and slightly branched networks, while basic catalysis promotes self-condensation of monomers and thus results in aggregated clusters of cross-linked molecules. Base-catalyzed sol synthesis yields water in addition to the polymerized silane, while acid-catalyzed condensation produces ethanol as a by-product. The base-catalyzed reaction deprotonates the surface of the silanol, which upon further reaction with another silanol, produces water as the leaving group. The role of the acid in acid-catalyzed reactions is to protonate the silanols. The reaction of a protonated silanol with another silanol will thus produce an alkoxy group (ROH) as illustrated in Figure 3.4. These reaction mechanisms are generally referred to as water or alcohol producing condensation, respectively, as described by Equations 3.2 and 3.3.

Whereas acid-catalyzed TEOS has been shown to polymerize by reaction-limited cluster-aggregation, base-catalyzed TEOS polymerizes by monomer-cluster growth due to slow hydrolysis and fast condensation reaction kinetics [28], as illustrated in Figure 3.5. Figure 3.5 describes the general sol and coating structures which

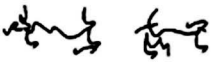

	Acid catalyzed	Base catalyzed
Reaction mechanism	<p>Hydrolysis</p> $\text{H}^+ + \text{>Si-OR} \xrightleftharpoons{\text{fast}} \text{>Si-O}^+\text{H-R}$ $\text{H}_2\text{O} + \text{>Si-O}^+\text{H-R} \xrightarrow{\text{slow}} \text{>Si-OH} + \text{ROH} + \text{H}^+$ <p>Condensation</p> $\text{H}^+ + \text{>Si-OR} \xrightleftharpoons{\text{fast}} \text{>Si-O}^+\text{H-R}$ $\text{>Si-OH} + \text{>Si-O}^+\text{H-R} \xrightarrow{\text{slow}} \text{>Si-O-Si<} + \text{ROH}$	<p>Hydrolysis</p> $\text{OH}^- + \text{>Si-OR} \xrightarrow{\text{slow}} \text{>Si-OH} + \text{OR}^-$ $\text{H}_2\text{O} + \text{OR}^- \xrightarrow{\text{fast}} \text{ROH} + \text{OH}^-$ <p>Condensation</p> $\text{>Si-OH} + \text{OH}^- \xrightarrow{\text{fast}} \text{>Si-O}^- + \text{H}_2\text{O}$ $\text{>Si-OR} + \text{>Si-O}^- \xrightarrow{\text{slow}} \text{>Si-O-Si<} + \text{RO}^-$
Gel structure		

Figure 3.4: Effect of sol pH on the hydrolysis and condensation rates and the resulting sol structure of a silicon alkoxide, adapted from [38].

develop as a result of the catalyst used during hydrolysis. Acid-catalyzed hydrolysis generates linearly chained molecules in the sol state. During substrate deposition, the linear chains are aligned due to the applied shear thus forming dense coatings. Furthermore, a combination of acid (cluster-cluster) and base (monomer-cluster) catalysis promotes the formation of cross-linked random aggregates that tend to form porous coatings when deposited on a substrate. Base-catalyzed sols form particular networks, which upon deposition generally produce thick coatings. Hence changing the pH conditions during sol synthesis will significantly alter the sol and coating structures.

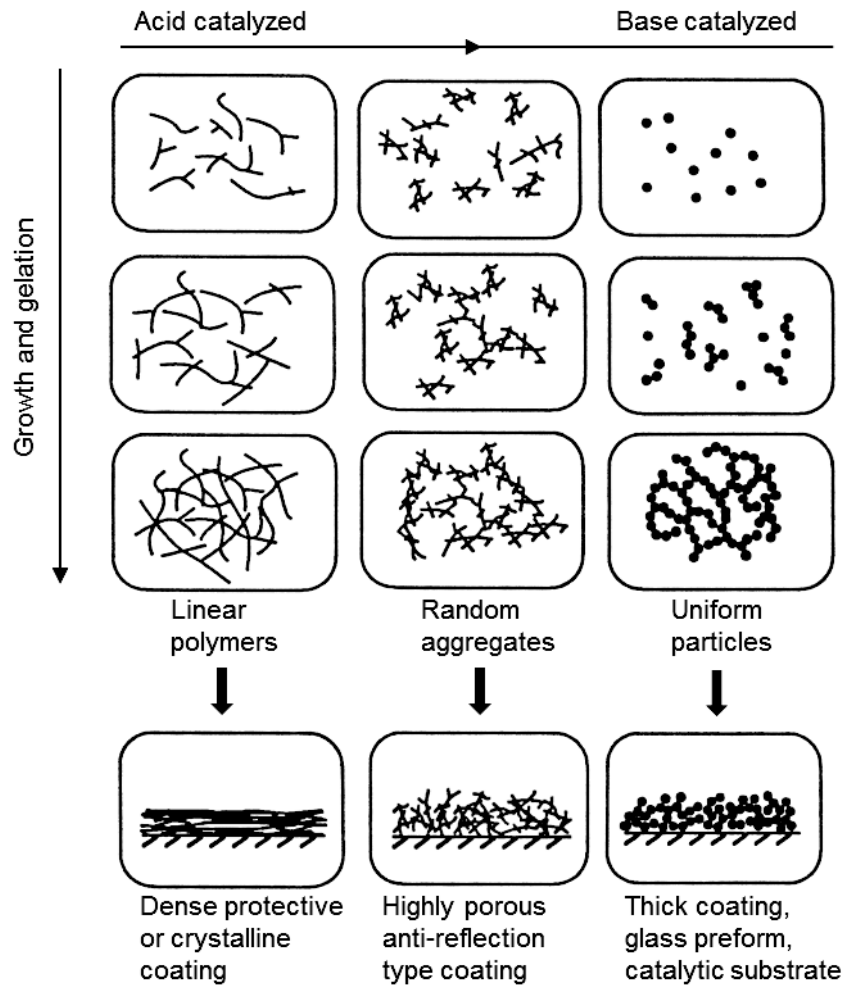


Figure 3.5: Schematic diagram visualizing the effect of pH on the growth and gelation of TEOS, modified from [19]. The relationship between the gel and coating structures is illustrated.

3.1.2 Hybrid inorganic-organic systems

The downside of pure inorganic coatings is that they are brittle, and due to a high potential for crack-formation, thicker coatings than 1 μm are difficult to obtain [18, 22, 43]. However, this problem can be counteracted by hybrid inorganic-organic chemistry, which is further elaborated in this section of the thesis.

The hybrid inorganic-organic materials constitute a field in chemistry that combines the hardness, brittleness and high chemical and thermal stability of the inorganic moiety with the flexibility and elasticity of the organic constituent. The result is materials with a wide range in properties such as different morphology, hardness, flexibility, physical and optical appearance, etc. The driving force for synthesizing hybrid inorganic-organic materials has been to improve material properties compared to traditional composites and conventional materials [25].

The history of hybrid inorganic-organic sol-gel synthesis

In the late 1970's organofunctionalized alkoxy silanes found their research ground as coupling agents between an inorganic, usually a metal or glass, and an organic phase in order to enhance adhesion [44]. The organofunctionalized alkoxy silanes are bifunctional; the alkoxy groups ideally react with hydroxyl groups at the substrate surface forming Si-O-Si bonds, while the functional organic groups extend away from the surface [45] and serve as a potential reaction site for other molecules to attach to the surface.

Schmidt et al. [46] reviewed the research of organoalkoxy silanes in the middle of the 1980's and were followed by Brinker [42], Novak [47] and Wen and Wilkes [25] a few years later.

As the requirements for the hybrid materials grew more demanding and challenging, the need for more advanced and sophisticated solutions arose. One concept that gained research interest was to incorporate a polymer (e.g. polydimethylsiloxane, PDMS) in an (organo)alkoxy silane (e.g. TEOS) network. This was achieved simply by dissolving the organic molecules or dispersing the particles in the precursor (inorganic matrix) solution [48]. The concept arose out of a need to be able to increase the flexibility of the silica structure while retaining most of the strength. Huang et al. [49, 50] therefore studied the effect of polymer concentration on the mechanical behavior of the material. True enough, they discovered increased flexibility with increased polymer concentrations, but the material stiffness was compromised. The structure of these organically modified silanes (ormosils) were further studied by Mackenzie et al. [51], who found a relationship between the sol acidity and the microstructures that evolved, especially concerning the chemical bonding between TEOS and the polymer. This group further studied these "rubbery ormosils" with respect to typical silica sol-gel parameters such as concentration ratios of catalyst, TEOS and water, effect of gelation rate and catalyst concentrations [52, 53]. Reviews on different ormosil systems have been provided by Sanchez et al. [24, 54–56].

Classifications of hybrid inorganic-organic silane-based materials

The hybrid inorganic-organic systems are usually categorized with respect to the chemical bonds present between the inorganic and organic units. Hence the two main classes of characterization are (i) the organic moieties are embedded in the inorganic matrix through weak bonds such as hydrogen bonds or van der Waals forces and (ii) the inorganic and organic phases are strongly connected by covalent bonds [24,25,54]. The categorization of the inorganic-organic materials is summarized in Figure 3.6.

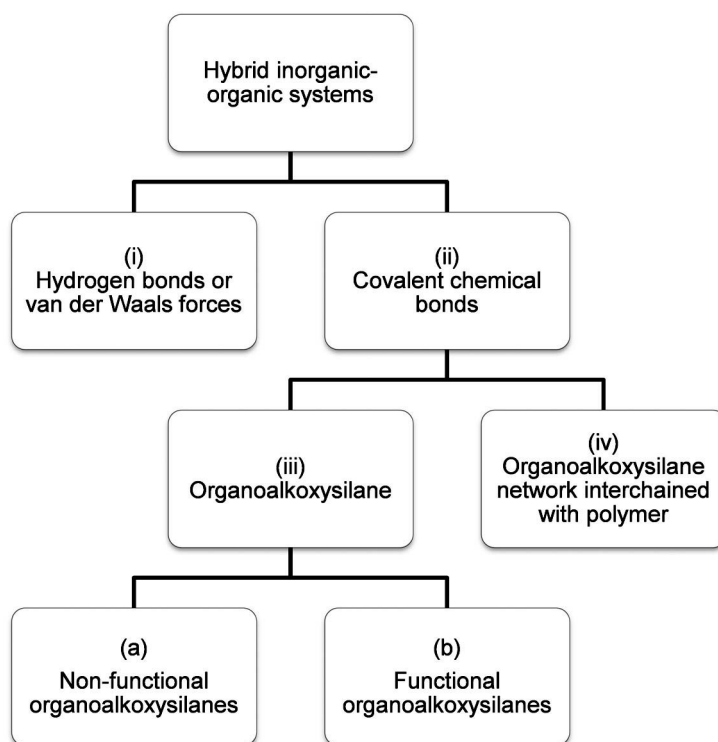


Figure 3.6: Different types of hybrid inorganic-organic silane-based materials based on the origin of the chemical bond between the phases, embedding of the organic phase and functionality of the alkoxy silane.

Within category (ii), there are two further distinctions that can be made. The organic groups can either be directly attached to the silicon, group (iii), or the organic composition can be embedded in the inorganic matrix at regular or random intervals, group (iv). The concept of embedding the organic component in the inorganic matrix is illustrated in Figure 3.7. Figure 3.7 (a) represents a random network which can consist either of pure silica, as in TEOS, or of more functionalized silanes, such as a trialkoxysilane. Figure 3.7 (b) displays a random and disordered structure, while the structure in Figure 3.7 (c) is ordered, and the organic moiety is embedded at controlled intervals. Since Si-C and Si-O bonds are hydrolytically stable, the

organic groups will be retained in the final material thus providing flexibility to the coating [48].

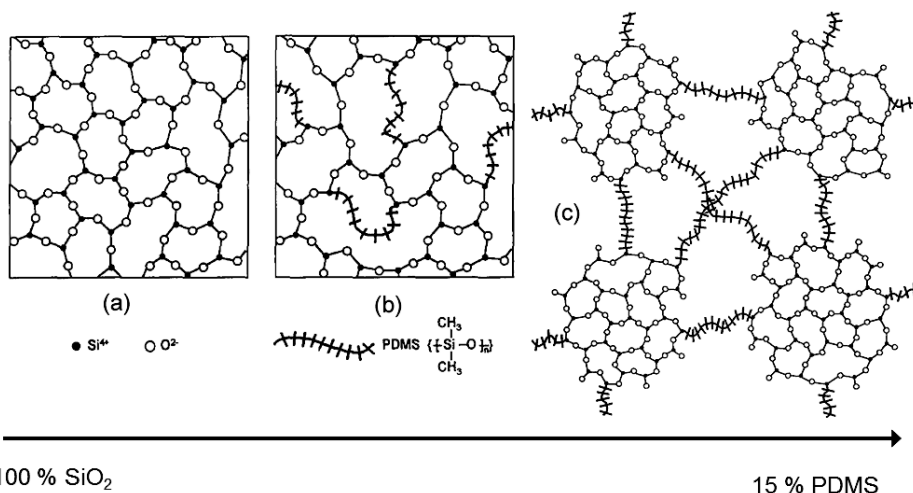


Figure 3.7: Two dimensional structures of (a) pure, amorphous silica (or an organoalkoxysilane), (b) silica (or an organoalkoxysilane) network interchained randomly with for instance polydimethylsiloxane, PDMS, and (c) ordered embedding of an organic composition (PDMS) in an inorganic matrix. The arrow points in the direction of increased addition of polymer as shown in (c). The Figure has been modified from [53].

It is possible to sub-divide group (iii) further based on the type of organoalkoxysilane into (a) non-functional organoalkoxysilanes such as methyl triethoxysilane, or (b) functional organoalkoxysilanes where (3-aminopropyl)triethoxy silane, γ -APS, is a good example [57]. By using the terminology derived for TEOS, the organofunctionalized silanes can be denoted $X_n\text{Si}(\text{OR})_{4-n}$ where X represents an organofunctional group such as an alkyl, aryl, acrylic, methacrylic, amino, methacryloxy, glycidoxy or epoxy group. Furthermore, the organofunctional groups are network modifiers [58], and the functional group will provide a variation in properties to the hybrid materials. The alkoxy silane, OR, can consist of methoxy, ethoxy, propoxy groups, etc., which will affect the reactivity of the silane.

One of the advantages of hybrid inorganic-organic chemistry is that tailoring can be achieved depending on the material requirements, such as mechanical (e.g. abrasion) and chemical properties (e.g. electrochemical corrosion). For instance, TEOS coatings are generally thin, and the coating thickness can be increased by the incorporation of organic species into the inorganic network. Substituting an ethoxy group in TEOS with an alkyl group, such as methyl, allowed the fabrication of thick and dense coatings [58, 59]. Furthermore, Murakami et al. [60] showed that the methyl substituted $(\text{CH}_3\text{Si}(\text{OC}_2\text{H}_5)_3)$ coatings were more flexible compared to TEOS-derived coatings on stainless steel substrates. The increased flexibility, which they observed, was suggested to be due to the CH_3 group.

It is thus clear that, as for general alkoxysilanes, hybrid inorganic-organic silane-based materials can also be tailored by optimizing the choice of alkoxy groups, altering the pH, varying the molar ratios of water and silane and the composition and amount of functional organic groups [22].

Characterization of silane-based sols

Liquid state ^{29}Si NMR spectroscopy has proven to be a useful tool for studying silane-based sols [22, 36]. As illustrated in Figure 3.8, a certain Si-O coordination environment can be assigned to a specific T^n notation, which can be detected by ^{29}Si NMR. The technique thus enables kinetic studies of the sol-gel mechanisms of an alkoxide through detection of hydrolyzed and condensed silane species.

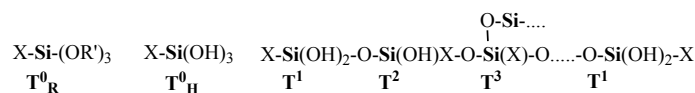


Figure 3.8: The different T^n species that may form during the reaction between water and a trialkoxysilane, modified from [61]. X denotes an alkyl group whereas OR' is an alkoxy group (Si-C).

Figure 3.9 (a) illustrates the hydrolysis and condensation reactions of a trialkoxysilane. Initially, the trialkoxysilane has three alkoxy groups, and this initial state is assigned T^0_R as the alkoxysilane is unhydrolyzed. However, as the hydrolysis reaction commences, several reaction routes are possible. One (monosilanol), two (silanediol) or three (silanetriol) alkoxy groups can be hydrolyzed before the onset of the condensation reaction. The hydrolyzed alkoxy group(s) is assigned T^0_H . The silanetriol is completely hydrolyzed and will thus give rise to a more intense signal than either the monosilanol or the silanediol. Condensation of the silanols leads to more condensed species such as T^1 (one siloxane bond), T^2 (two siloxane bonds) and finally T^3 (three siloxane bonds). The different T^n species are detected at different chemical shift values in a ^{29}Si NMR spectrum as shown in Figure 3.9 (b).

Furthermore, Fourier transform infrared (FTIR) spectroscopy registers the stretching and bending vibrational frequencies of chemical bonds, in which Si-OH and Si-O-Si bonds are characteristically detected in the range of $1000\text{-}1200\text{ cm}^{-1}$, which is illustrated in Figure 3.10. Figure 3.10 shows the location of the Si-O bands in a transmission spectrum. The location of the NH_x and CH_x bands are also shown. Owing to the sharp detection of the Si-O bands, FTIR is thus a suitable technique for studying the hydrolysis and the condensation reactions in silane-based sols.

^{29}Si NMR and FTIR characterization of the hydrolysis and condensation mechanisms of different organoalkoxysilanes have extensively been conducted [61, 62, 64–71].

Three dimensional structures of silane-based sols

It has since the 1950's been recognized that the structure of silane-based compounds constitute cages of different polyhedral structures. These structures are generally

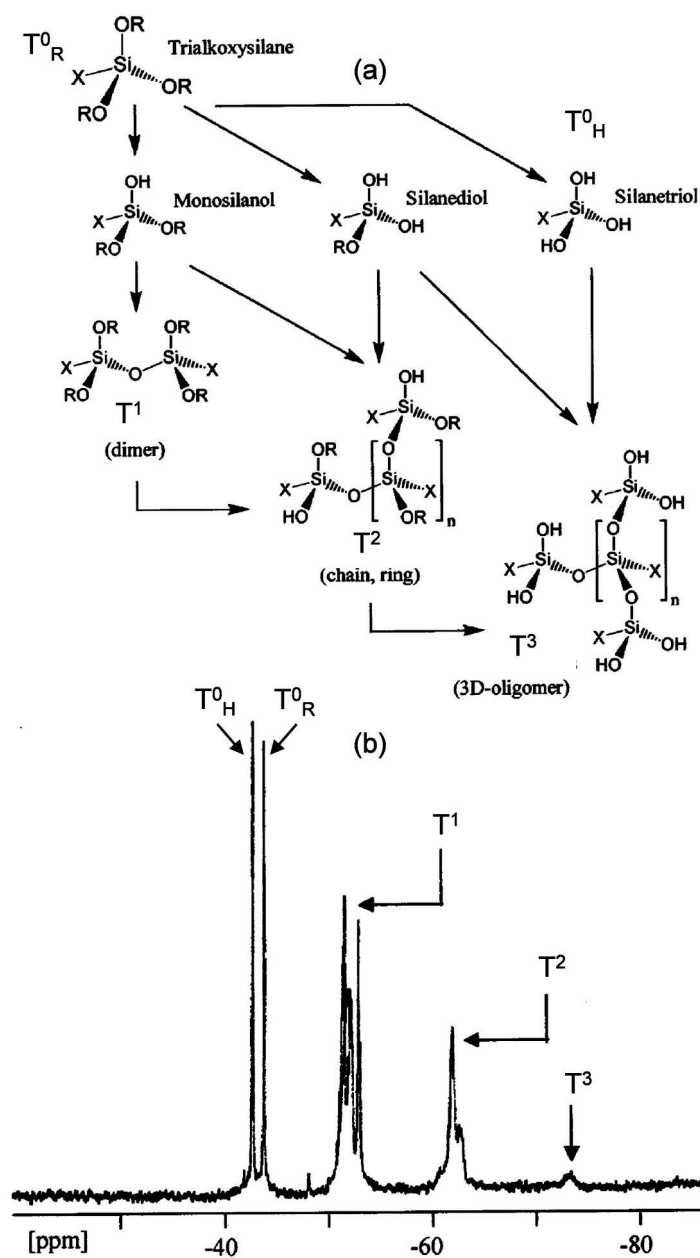


Figure 3.9: (a) Hydrolysis and condensation reactions of an organotrialkoxysilane. (b) Typical ^{29}Si NMR spectrum of an organotrialkoxysilane, modified from [62]. The T^0_H , T^0_R , T^1 , T^2 and T^3 notations are assigned.

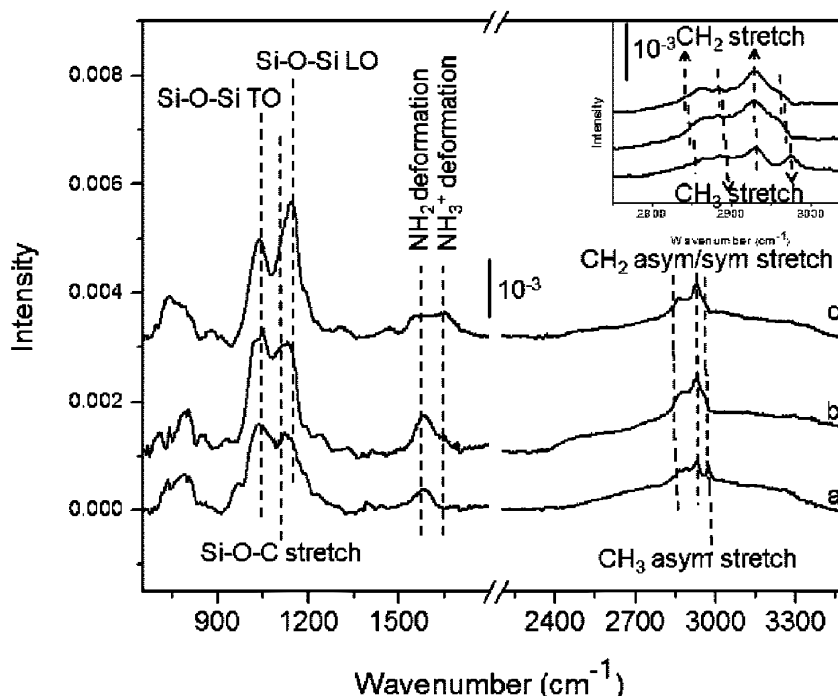


Figure 3.10: Transmission IR spectra of γ -APS-derived coatings, adapted from [63]. (a) Prepared at room temperature, (b) 50 °C in situ and (c) 70 °C in situ. The inserted Figure displays details of the CH_x species.

referred to the generic term silsesquioxanes owing to the $\text{SiO}_{1.5}$ structural backbone, which reflects a fully condensed structure [72, 73]. Liquid and solid state ^{29}Si NMR in combination with mass spectroscopy [62, 73, 74] have been used to determine the polyhedral structure of silane-based sols and gels. Extensive reviews of silsesquioxanes and their polyhedral structures have been provided by Baney et al. [75] and Cordes et al. [76]. However, several authors have contributed to the understanding of the formation of these cage structures [42, 70, 73–80]. Figure 3.11 gives a general overview of the possible three dimensional structures that can exist in silsesquioxanes, ranging from random amorphous structures (Figure 3.11 (a)) to ordered cages (Figure 3.11 (c)-(e)). Ladder-like and partial cage structures are also possible as indicated in Figure 3.11 (b) and (f). The cage structures (Figure 3.11 (c)-(e)) comprise three siloxane bonds and will thus appear as T^3 in the ^{29}Si NMR spectrum, which is also the case for the random structure in Figure 3.11 (a). The ladder-like and the partial cage structures additionally display two siloxane bonds (Figure 3.11 (b) and (f)), which will give rise to a detection of T^2 in the ^{29}Si NMR spectrum. However, the most common polyhedral structure for trialkoxysilanes is the T_8 cage shown in Figure 3.11 (c).

The "T" in the cage structures in Figure 3.11 refers to the number of Si atoms connected to three oxygen atoms in the cage [76]. The preferential presence of T_8

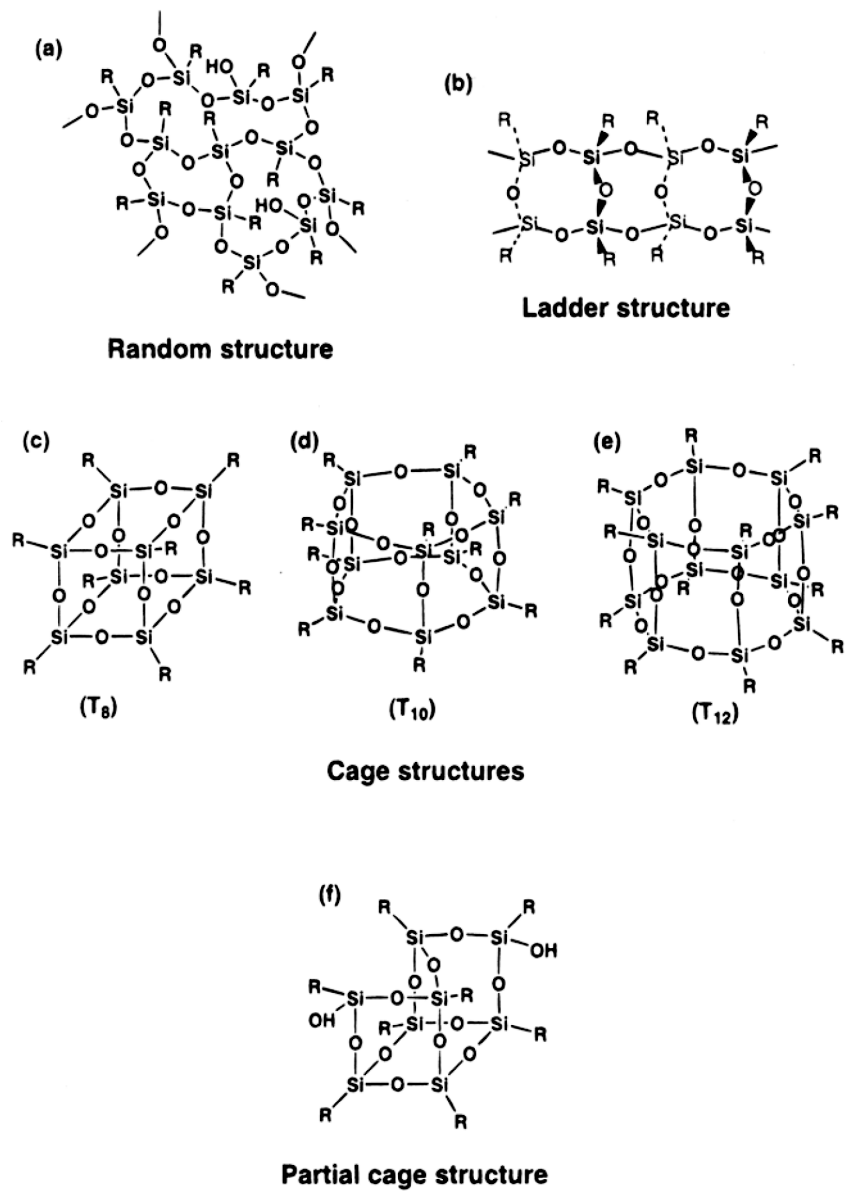


Figure 3.11: Possible cage structures of silsesquioxanes, adapted from [75].

as opposed to T_{10} or T_{12} was suggested by Cordes et al. [76] to be due to the stability of the Si_4O_4 ring structure. However, usually T_{10} and T_{12} cages, although in smaller amounts, are also present. According to Asuncion and Laine [77], the T_8 cage structures can be prepared by hydrolytic condensation of organosilanes using either acid or base catalysis. The resulting polymerized structures are shown in Figure 3.12. Polymerization through the use of organic cross-linkers (e.g. polymeric units) is illustrated in Figure 3.12 (a), while Figure 3.12 (b) displays the route to polymerization of the silsesquioxane cages.

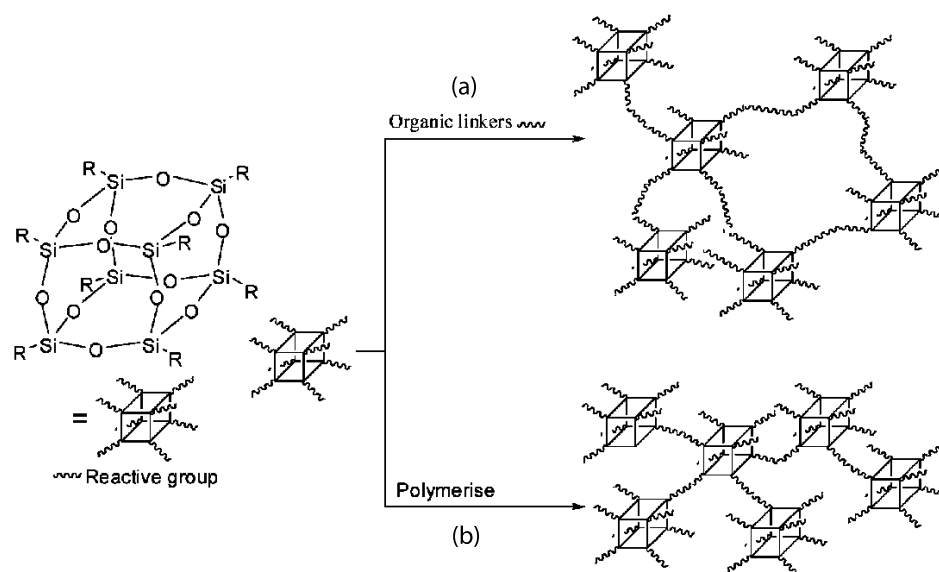


Figure 3.12: Schematic representation of (a) polymerization through the use of organic linkers and (b) cross-linked polymeric networks of silsesquioxanes, adapted from [76].

Applications of hybrid inorganic-organic silane-based coatings

Organofunctional alkoxy silanes find the use as adhesion promoters, surface modifiers, cross-linking agents and as a means to reinforce ceramic surfaces [62]. Organofunctional alkoxy silanes have also been used to improve the properties of polycarbonate surfaces [81]. Aegerter et al. [82] have provided a review of possible applications of different sol-gel systems, whereupon the use of silane-based hybrid inorganic-organic materials is especially elaborated. Owing to the wide range of possibilities of functionalization and properties of hybrid materials, the inorganic-organic silane-based hybrid materials find applications in several conventional fields such as coatings for anti-reflective glass for architectural structures [82], automotive window shields and mirrors with contact angles with water in the range of 90 to 110 °, protective layers for wood structures [58], functionalizing textiles, as dental fillers [83] and in bone cement [84], to mention but a few. Furthermore, hybrid epoxy-functionalized

organoalkoxysilanes can have a potential as an abrasion-resistant coating on automotive clearcoats and as a coating on structural glass [57]. The latter coatings were also shown to be UV resistant, and it was proposed that they could find areas of application such as anti-graffiti coatings and biocide-free fouling-release coatings for ships. Hybrid inorganic-organic coatings are also commonly used for corrosion protection of steel, which will be further addressed in this thesis.

3.2 Dip coating

Several coating deposition techniques exist that allow the use of liquid precursors, e.g. electrophoretic deposition, spray coating, spin coating and dip coating.

To obtain coatings from a sol in general, there are a few requirements that have to be met comprising wettability of the sol on the substrate (low wetting contact angle, θ , and low surface tension), and the sol has to remain constant in composition when aged [19]. The sol wets the substrate when $\theta \leq 90^\circ$ and when the surface tension is low [85]. Alcohol solutions generally have a low surface tension and are preferred for sol deposition as opposed to aqueous solutions that display higher surface tension values [19].

Dip coating is a useful means of applying a coating to substrates. The technique involves immersing a substrate into a bath containing a sol and withdrawing the substrate at a controlled speed, as indicated for a flat substrate in Figure 3.13. One of the advantages to dip coating is that all sides of the substrate can be coated simultaneously.

Surface tension and capillary forces on the substrate surface form a meniscus, which clings to the substrate as it is withdrawn from the sol bath, as seen in Figure 3.13. Initially, the sol structure, which can for instance be a silane, contracts because the solvent starts to evaporate simultaneously as the excess sol is drained off due to gravity [86]. The sol viscosity, water and silane concentrations significantly influence the coating thickness. Networks form during condensation, and eventually, the molecules will be so tightly compressed and bonded together that the gravitational flow stops [86, 87]. The sol viscosity can effectively be increased by either increasing the silane or organic component concentration (assuming inorganic-organic hybrid sols). Furthermore, the molar ratio of water and silane has been found by Guglielmi et al. [88] to affect the surface tension of the sol and the thickness of dip coated layers of silane-based coatings.

There are several models that have been developed for predicting the coating thickness. One model is based on reactions taking place when the excess liquid is drained from the substrate, and this scenario is depicted in Equation 3.4 [86, 89, 90]. At high withdrawal speed, the deduced coating thickness, h , was expressed as depending on viscosity (η), substrate velocity (u), sol concentration (c_1), density (ρ) and gravity (g).

$$h = c_1 \left(\frac{\eta u}{\rho g} \right)^{1/2} \quad (3.4)$$

Furthermore, c_1 is approximately 0.8 for Newtonian liquids. When the substrate

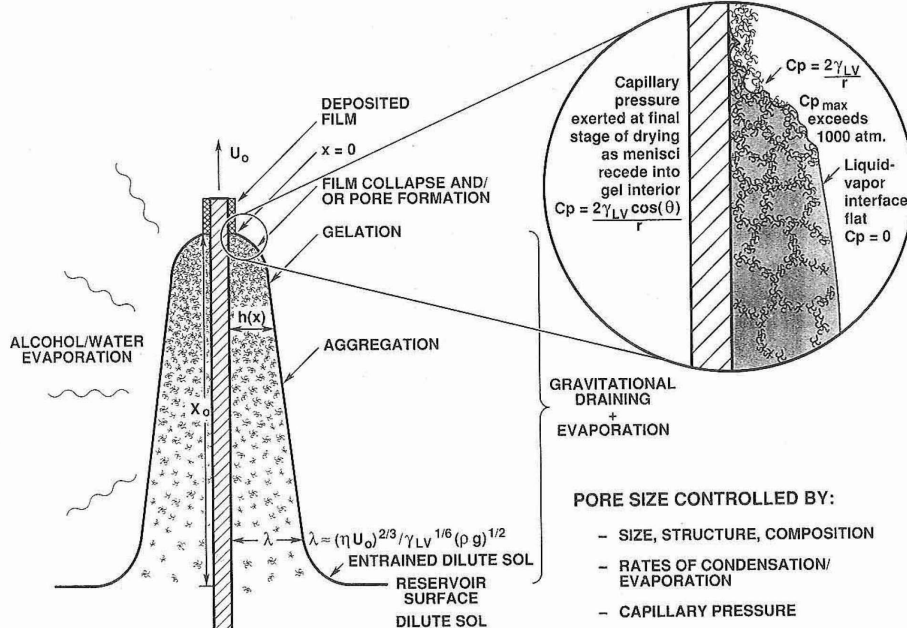


Figure 3.13: Fundamentals of the dip coating process during the withdrawal of a substrate from a sol bath, which can be silane-based [86].

speed and viscosity are low, this balance is modulated by the ratio of viscous drag to liquid-vapor surface tension, γ_{lv} , according to the relationship shown in Equation 3.5. This model is illustrated in Figure 3.14 where it is clear that the thickness depends on the substrate withdrawal speed and the sol viscosity.

$$h = 0.94 \frac{(\eta u)^{2/3}}{\gamma_{lv}^{1/6} (\rho g)^{1/2}} \quad (3.5)$$

Whereas the first studies used one model for the whole range of withdrawal speeds, recent work has shown that the dip coating process can be divided into regions where evaporation (capillarity, low speed) and draining (Landau-Levich, high speed) are the governing processes [91–93]. At low speed, the choice of solvent is crucial for the coating thickness while at high speed, in the Landau-Levich regime, viscosity is more important. Generally, viscosity increases with increasing silane concentration [22]. Viscosity also increases with the mass fraction of polymer (resin) [94] and acidity of the solution [95].

Doumenc and Guerrier have found that the dry coating thickness at low withdrawal speed is dependent on the evaporation flux measured with pure liquid (F_{ev}), substrate velocity (u) and bulk solute volume fraction (ϕ_0) as shown in Equation 3.6 [92].

$$h_d = \frac{F_{ev} \phi_0}{u} \quad (3.6)$$

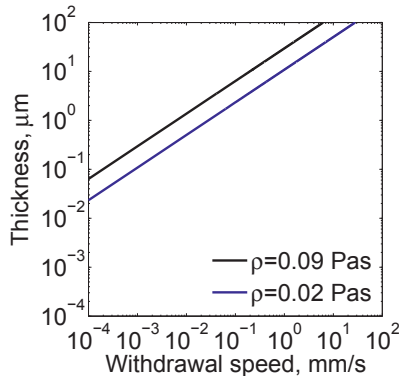


Figure 3.14: The effect of substrate withdrawal speed on coating thickness using the conventional model given in Equation 3.5 [22] assuming a density of $1 \text{ g} \cdot \text{cm}^{-3}$ and water γ_{lv} of 0.072 Jm^{-2} . The viscosities correspond to two different hybrid aminopropyl silane sols.

Combining the two aforementioned regimes led Faustini et al. [91] to deduce Equation 3.7 for the overall velocity range, which depends on the precursor concentration (c_i), molar weight (M_i), density (ρ_i), fraction of material (α_i), rate of solution evaporation (E), substrate velocity (u), coating width (L) and a global constant (D).

$$h_0 = \left(\frac{c_i M_i}{\alpha_i \rho_i}\right) \left(\frac{E}{Lu} + Du^{2/3}\right) \quad (3.7)$$

Even though, dip coating is a versatile deposition technique, there are still some obstacles to the process. Depending on the sol viscosity, draining and evaporation during the deposition will result in a thickness gradient along the substrate length. This, of course, causes a non-uniform coating thickness. In addition, advanced geometries are difficult to coat.

3.3 Drying of coatings

Initially during coating deposition, strong van der Waals bonds are formed between the metal substrate and the coating [59]. During thermal curing, this bond develops into a stable, covalent Si-O-metal (substrate) bond resulting in excellent adhesion properties for silane-based hybrid inorganic-organic coatings [59, 96]. The need for a drying stage is thus understandable. However, in order to avoid a critical pressure building up in the green coating, the heating rate has to be controlled. A comprehensive and detailed description of the drying process has been provided by several authors [23, 87, 97–99], and only a short outline is provided in this thesis.

There are two critical parameters during the drying of a green coating worth mentioning. Firstly, the drying (evaporation) process is surface tension driven. This concept implies that the liquid will try to wet the surface of the green coating during all the drying stages. As the volume percent of liquid decreases, the solid

has to contract in order to reduce the surface tension. The result of this is a high capillary pressure when the surface liquid has evaporated. Secondly, the radius of the liquid meniscus is important. As the liquid meniscus recedes into smaller and smaller pores caused by the green coating contraction, the capillary pressure increases significantly as depicted in Equation 3.8 and illustrated in Figure 3.15. Keeping these two parameters in mind, there are generally four main drying stages, namely the constant rate period, the critical point, the first falling rate period and finally the second falling rate period [23, 87]. These stages are outlined in Figure 3.16, and the microstructural changes that occur at each stage are illustrated in Figure 3.17.

$$P_c = -2\gamma_{lv} \frac{\cos\theta}{r} \quad (3.8)$$

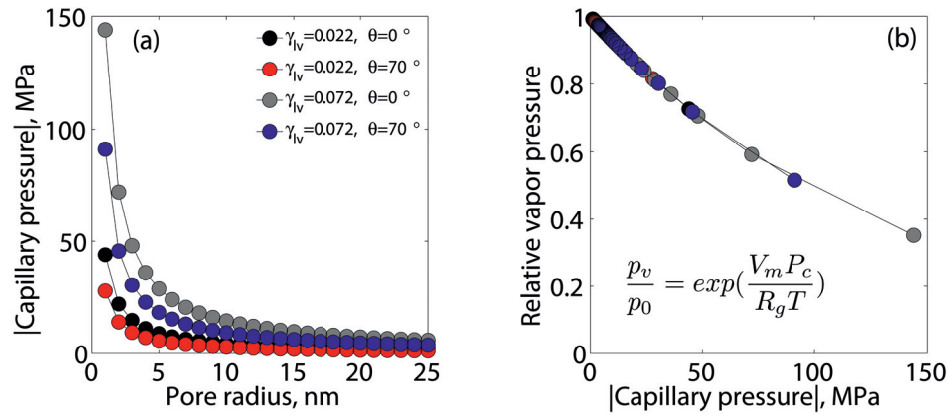


Figure 3.15: (a) Effect of pore radius on the liquid capillary pressure, $|P_c|$, calculated from Equation 3.8 by using $\gamma_{lv}=0.072$ J/m² (blue and gray dots) and $\gamma_{lv}=0.022$ J/m² (red and black dots) simulating water and alcohol as the liquid, respectively, at two different contact angles. (b) Effect of liquid capillary pressure, $|P_c|$, on the relative vapor pressure. The inserted Equation has been used to calculate the relationship with the assumptions that $T=298$ K and $V_m=18$ cm³/g. The Figure has been modified from [22].

Initially, the green coating is wet with a flat meniscus (Figure 3.16 (A)), and the structural coating components are homogeneously distributed in the liquid (Figure 3.17). Evaporation initiates the constant rate period depicted in Figure 3.16 (B). During this stage, the green body shrinks due to evaporation as evidenced by the significant weight loss in Figure 3.17. The green coating contracts in order to keep the surface tension at a minimum, which causes the formation of a concave liquid meniscus. The radius of the liquid meniscus decreases as the drying time increases and as the green coating is reduced in size. During the constant rate period, the green coating shrinks non-uniformly causing a deformed structure (Figure 3.17). At the critical point, the sol structural components are in contact, and no further shrinkage occurs. Further evaporation can only take place from the liquid which is

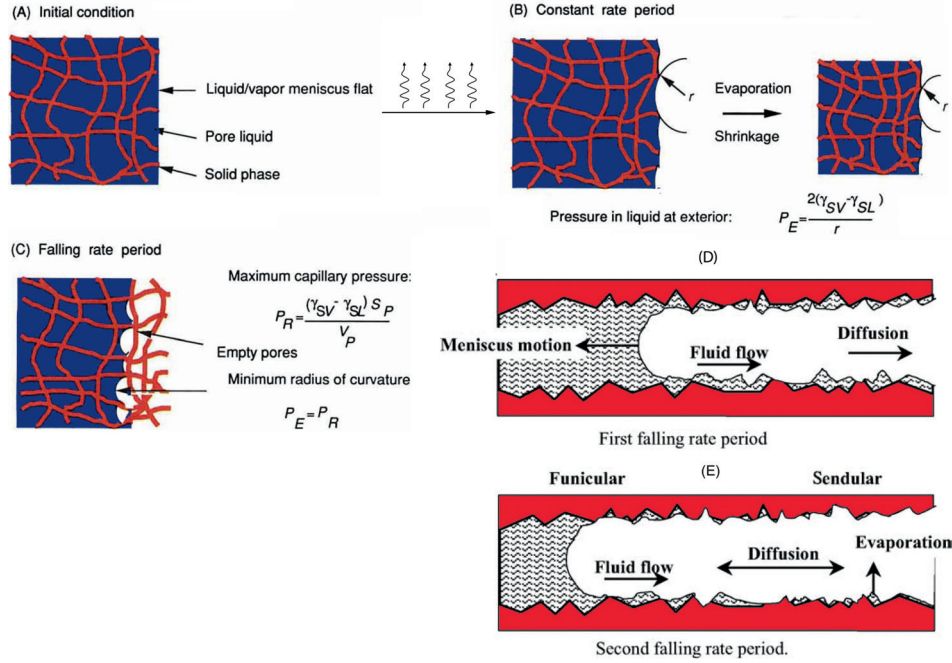


Figure 3.16: Schematic illustration of the drying process of a bulk gel modified from [87, 98]. (A): The initial wet condition of the bulk gel surrounded by liquid. (B) and (C): The liquid starts to evaporate as it tries to spread on the solid surface causing the gel network to contract. The drying stages are related to the pore and meniscus radii. (D) and (E): The final stages of drying describing evaporation of entrapped liquid in the pores.

present in the pores. This marks the beginning of the falling rate period, which is illustrated in Figure 3.16 (C). At this stage, as the meniscus recedes into the pores, a capillary pressure builds up (Equation 3.8), which will greatly affect the drying process. Figure 3.15 (a) illustrates the drastic increase in the capillary pressure with decreasing pore size, and Figure 3.15 (a) also demonstrates the significance of the wetting contact angle. Higher contact angle reduces the capillary pressure, and the effect of the contact angle becomes more pronounced at lower pore size. Additionally, as shown in Figure 3.15 (b), the wetting contact angle influences the relative vapor pressure and will thus increase the evaporation rate. Furthermore, a lower surface tension will promote evaporation as can be deduced from Equation 3.8. At the beginning of the falling rate period, the liquid in the pores is in contact with the surface of the green coating (Figure 3.16 (D)), and the liquid is non-uniformly distributed in the green coating (Figure 3.17). During the last stage, which is the second falling rate period depicted in Figure 3.16 (E), the liquid is no longer in physical contact with the surface of the green coating. Evaporation thus occurs in two steps, whereupon the first step comprises diffusion of the liquid to the surface followed by evaporation. When all liquid has evaporated, the green coating is

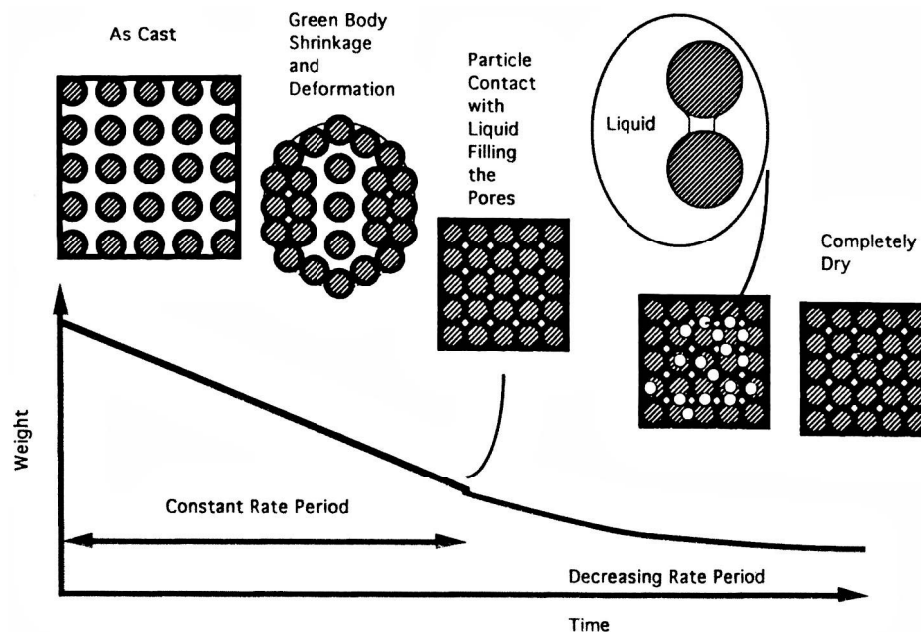


Figure 3.17: Drying of a green body adapted from [97]. The weight loss with time at the different drying periods as well as the microstructure of the gel is depicted.

completely dry as presented in Figure 3.17.

Furthermore, the evaporation rate is influenced by the choice of solvent, which is illustrated in Figure 3.15. Figure 3.15 (a) shows the combined effects of surface tension and contact angle on the capillary pressure in Equation 3.8. Increasing the contact angle and reducing the surface tension greatly reduces the capillary pressure. Furthermore, Figure 3.15 (b) depicts the higher relative pressure which can be achieved by reducing the surface tension of the liquid. Thus the choice of solvent will significantly affect the magnitude of the capillary pressure exerted by the liquid entrapped in the pores during the falling rate period.

In addition to optimizing the choice of solvent, it is also possible to reduce the capillary pressure by the addition of surfactants [43, 87]. The mechanism of the surfactants is also to reduce the surface tension. Due to the drying stresses that evolve and owing to the fact that inorganic materials are brittle, the typical crack-free thickness limit of inorganic coatings is $1\ \mu\text{m}$ [18, 22, 43]. However, the coating thickness can be increased by applying hybrid inorganic-organic chemistry because the organic moiety introduces flexibility and elasticity to the structure and thus makes it more compliant.

Furthermore, the final structure of the dry coating is shown in Figure 3.5. Depending on the sol synthesis, three possible coating structures are described. Acid-catalyzed sol-gel synthesis was shown to promote a linearly chained sol structure, which upon substrate deposition formed thin and dense coatings. A combination of acid and base sol-gel catalysis is analogously shown to fabricate porous coatings

due to an extended and random cross-linking of the networks in the sol. Colloidal sol dispersions are similarly demonstrated to result in thick coatings.

3.4 Corrosion protection of steel

3.4.1 Conventional corrosion protection of steel

The use of carbon steel finds many areas of application. It is used for marine constructions, as a transportation material and in pipelines [10], to mention but a few. Water, oxygen and chloride ions are potential corrosion species that will destroy the metal when exposed [59]. Corrosion of steel causes problems both from an economic and an environmental perspective, and methods to prevent corrosion have to be sought.

Conventionally, phosphate and chromate conversion coatings have been used for corrosion protection of steel [10–12]. Addition of corrosion inhibitors, such as Ce^{3+} salts, to sol-gel coatings have also improved the corrosion protection capability [100]. However, it has been shown that the corrosion inhibitors can affect the barrier properties of the sol-gel coatings and thus to increase the corrosion rate. An efficient method to prevent this is to use corrosion inhibitor-containing capsules that are homogeneously distributed in the coating. By this way, the inhibitor will only be released when in contact with the electrolyte, and the inhibitor can diffuse to the damaged site and heal the coating.

3.4.2 Novel hybrid inorganic-organic materials as anticorrosive coatings

Silane-based hybrid inorganic-organic coatings have good adhesion towards steel, and they improve the corrosion protective properties of metals [11]. The organic components repel water and since they remain in the coating they partake in the formation of dense and thick coatings thus limiting the diffusion of the corrosion species through the coating to the metal surface [11, 59]. Additionally, silane-based inorganic-organic coatings have been shown to possess a high water resistance [11], and should thus be suitable for corrosion protection of steel.

Organofunctional alkoxysilanes as anticorrosion barriers

Subramanian et al. [101] studied the use of γ -APS (4 % in methanol solution) derived coatings and other silanes for corrosion protection of steel. They found that γ -APS alone provided inadequate protection because the coatings acted as porous membranes hence the electrolyte was able to diffuse through the membrane causing coating dissolution and disruption. However, the coatings were thin and less than 100 nm. Trabelsi et al. [102] suggested the orientation of the amino groups in γ -APS to be important for the corrosion protection properties of γ -APS-derived coatings. When the amino groups extend away from the substrate surface, the amino groups on the γ -APS (4 % in methanol solution) coated surface form a protective layer.

Exposure to an acidic electrolyte, protonates the amino groups, which improves the corrosion resistance. The protonated surface amino groups may attract chloride ions hence depleting chloride ions from the electrolyte. The corrosion resistance is thus improved until the remaining chloride ions in the electrolyte solution diffuse through pores and defects in the hybrid coating to the coating/substrate interface.

Even though a γ -APS-derived coating is not able to withstand long-term electrolyte exposure, it can still provide an initial protection of the steel substrate due to the formation of a protective barrier on the surface. Tailoring the sol parameters (such as pH) can promote NH_2 surface groups. For instance, NH_2 is less likely to be protonated at pH 10-12. At high pH, NH_2 -groups are more likely to interact with silanol groups of adjacent molecules. Upon substrate deposition, the NH_2 -groups can then interact with the substrate through hydrogen bonds. Studies have shown that it is possible to improve the corrosion protection performance by using γ -APS as a top coat on steel, but it appears that the general consensus is that more tailored systems are required.

Dave et al. [103] studied the corrosion behavior of different trialkoxysilane-derived coatings on steel and discovered that the functional groups will significantly affect the corrosion resistance of the coating. For instance a cyano functional group showed best corrosion protection capability while a benzyl functional group provided a more hydrophobic coating.

The extent of condensation of silanol groups to form -Si-O-Si- networks during curing at 150 °C in silane-based coatings was found to significantly affect the corrosion resistance in vinyltriethoxysilane (4 % and 10 % ethanol solutions) coatings [104]. This was also documented by Zandi Zand et al. [15] for 3-glycidoxytrimethoxy silane coatings. Furthermore, these coatings improved the corrosion resistance of steel by forming a physical barrier as was observed by electrochemical polarization and salt spray tests.

Mixed (organo)alkoxysilanes for improved corrosion protection

The use of more than one alkoxysilane has also been studied for corrosion protection with TEOS as the main component. For instance a mixture of acid-catalyzed TEOS and 3-methacryloxypropyl trimethoxysilane formed a physical barrier, which protected the stainless steel substrate from corrosion [105–107]. Castro et al. [108] further showed that the coating thickness of a mixture of TEOS and methyltriethoxysilane was an important parameter for corrosion protection of stainless steel substrates. Electrophoretic deposition allowed coatings up to 12 μm , while dip coating was limited to 3.5 μm . TEOS and methyltriethoxysilane offered good corrosion protection initially during immersion, but after 48 h, localized corrosion at the substrate surface was observed [109]. Qian et al. [10] discovered that hybrid inorganic-organic coatings, which consisted of a pre-hydrolyzed amino silane mixed with an epoxy siloxane, could improve the anticorrosive properties of steel.

More sophisticated hybrid systems involved co-polymerization of organofunctional alkoxysilanes (e.g. 3-(trimethoxysilyl)propyl methacrylate with methyl methacrylate monomer into organic poly(methyl methacrylate) (PMMA)) whereupon they reacted further with TEOS [110]. Embedding of PMMA in TEOS produced smooth

coatings which were able to improve the corrosion resistance of cold rolled steel. Methyl substituted trialkoxysilane (methyltriethoxysilane) was shown to have superior corrosion protective capabilities of stainless steel as opposed to phenyl substituted trialkoxysilane (phenyltrimethoxysilane) [111]. The proposed explanation was that the use of the methyl substituted trialkoxysilane promoted an increase in the rates of hydrolysis and condensation.

Although γ -APS as a top coat alone provided insufficient corrosion protection, the combination with a bis-silane was shown to improve the corrosion resistance of galvanized steel significantly [14, 102]. The role of γ -APS was suggested to function as a catalyst for the hydrolysis reaction of the bis-silane thus increasing the amount of silanols and the degree of condensation. Figure 3.18 illustrates (a) a mono- and (b) a bis-silane, and it is clear that the amount of Si-O bonds are twice as many in a bis-silane as opposed to a mono-silane.

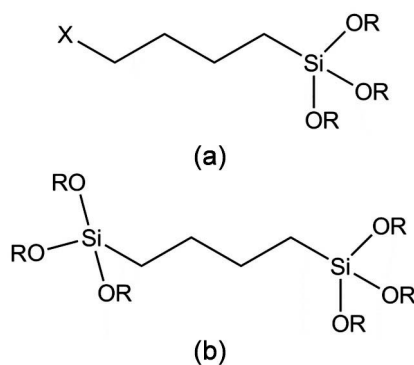


Figure 3.18: Structures of (a) mono-silane and (b) bis-silane modified from [112].

A top coat consisting of paint over a functionalized alkoxy silane has also proven to be a fruitful approach. Chico et al. [113] deposited γ -APS on steel substrates, applied a top coat of an alkyd/polyester aminoplast paint and found through electrochemical impedance spectroscopy, salt fog test and outdoor exposure that the anticorrosive properties of these coatings were comparable to phosphate treated steel.

3.4.3 Summary of corrosion protective capability of hybrid inorganic-organic silane-based coatings

The corrosion protection ability of hybrid inorganic-organic silane-based coatings can be improved by tailoring functional groups. For instance, cross-linked aminofunctionalized silanes have shown improved corrosion protection behavior by reducing the corrosion current density significantly compared to bare metals [59]. Another interesting feature was that increasing the amount of amino groups assisted in further improvement of the corrosion protection. However, more advanced hybrid inorganic-organic systems allow better control and tailoring of properties specifically aimed at preventing corrosion.

There are a few concepts that can be used to obtain better corrosion protection of coatings on steel, and these comprise longer $-\text{CH}_2-$ chains, fully condensed $-\text{Si-O-Si}$ -networks, more NH_2 -groups and finally thicker coatings. Furthermore, the organic constituent in the hybrid inorganic-organic coatings introduces hydrophobicity (and low surface tension) and assists in forming dense coatings with reduced porosity because the alkyl chains fill the pores [59, 103]. The surface hydrophobicity is an important parameter for corrosion protective coatings [114].

Surface pretreatment of metals with silanes (silanization) has proven competitive to chromate-pretreatment [11, 12, 14], where mono- and bis-silanes have been most studied [14, 115]. Corrosion protection was best achieved by a mixture of mono- and bis-silane.

3.5 Prevention of wax deposition

3.5.1 Conventional means of wax removal

The flow characteristics of the crude oil change when solid wax particles appear, and the fluid displays non-Newtonian behavior, which renders the oil thixotropic with plastic properties [116]. Wax deposition and thickness of the deposited layer are governed by pipe wall and oil temperatures, flow rate, concentration gradient, reaction time, wax composition with respect to carbon number, heat conductivity of the wax layer, shear stress (which depends greatly on the pipe diameter) and the pressure drop in the pipeline [4, 116]. The formed wax deposits are hard and solid, and they are conventionally removed by mechanical pigging [117]. The deposits are generally inert to acids, bases and oxidizing agents [116], but thermal treatment and chemical inhibitors can be used to prevent the formation of the wax [117]. The chemical inhibitors are usually comprised of either detergents, dispersants or wax crystal modifiers [118]. The detergents and dispersants are surface-active agents, and they modify the surface of the pipe wall and keep the wax crystals well dispersed in the fluid. The crystals are thus prohibited from interacting with the cold surface of the pipe wall. The crystal modifiers affect the nucleation process of the wax nuclei by altering the surface characteristics and the growth properties of the wax. However, these methods have to be tailored for each oil well because every crude oil composition is unique. A more general method applicable to all crude oils is therefore sought.

3.5.2 Build-up of wax layer

Paraffins constitute the fraction of the crude oil that causes wax precipitation. During transportation from the oil well, where the temperature is in the range 70-150 °C [119], the temperature drops drastically due to cooling caused by the sea water and the sea bed. When the temperature of the fluid drops below the wax appearance temperature (WAT), wax crystals deposit. Figure 3.19 illustrates the inside of a pipeline, which transports crude oil. A temperature gradient inside the pipeline arises from the warmer crude oil and the colder pipe wall, which is governed

by the sub sea temperature.

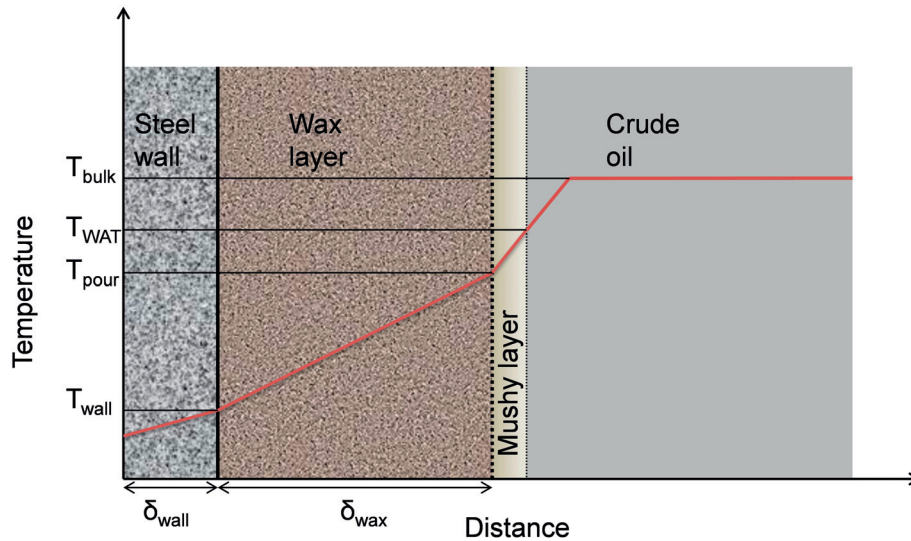


Figure 3.19: Temperature profile as a function of the distance from the pipe wall. Redrawn from [120]. T_{bulk} is the temperature of the crude oil, T_{WAT} the temperature at which the wax is first detected when cooled, and T_{pour} is defined by the temperature at which the crude oil loses its flow characteristics. δ_{wall} and δ_{wax} correspond to the thickness of the pipe wall and the wax layer, respectively.

The crystal growth of the wax nuclei are governed by the Gibbs energy, and initially a thin wax layer deposits on the colder pipe wall [116], as illustrated in Figure 3.19. A gel-like composition, which is a mixture of wax and fluid, forms at the interface between the crude oil and the wax deposit, which is referred to as the mushy layer in Figure 3.19. The temperature in this layer is higher than the pour point (the temperature at which the crude oil loses its flow characteristics), but lower than the WAT. As the wax deposits, a fraction of the oil is entrapped within the wax phase. The wax layer close to the crude oil has a higher wax content and faster ageing rate than the wax layer at the pipe wall-wax layer interface [121], and these conditions result in a temperature gradient through the wax layer (Figure 3.19).

The mechanisms of the wax deposition have been extensively studied [116, 119, 121–123]. Generally, carbon numbers between 20 and 70 are the main concern with regards to wax deposition. Singh et al. [124] have studied the effect on wax layer build-up with respect to ageing. They found that the mass fraction of hydrocarbons in the wax layer with carbon numbers greater than 28 increased with time whereas decreasing concentration for carbon numbers less than 28 was observed. This was caused by diffusion in the entrapped oil phase. Molecular diffusion is believed to be the main mechanism for formation of the wax layer on the pipe wall, but the composition with respect to alkanes also displays a significant effect [2, 4]. The appearance of the wax deposit can be altered by for instance increasing the velocity

of the fluid [125], which results in harder deposits, but with a thinner wax deposit thickness. A review of thermodynamic studies of the wax deposition has been provided by Ji et al. [117], and mathematical models to determine the thickness of the wax layer have been proposed [126].

3.5.3 Surface modification with hybrid inorganic-organic silane-based coatings

Adhesion between two surfaces is minimized when the interfacial surface energy is low [127]. The work required to separate a liquid droplet from a solid surface is given by Equation 3.9 and is determined by the interfacial energies.

$$W = \gamma_{sv} + \gamma_{lv} - \gamma_{sl} = \gamma_{lv}(1 + \cos\theta) \quad (3.9)$$

θ in Equation 3.9 is the wetting contact angle, while γ_{sv} , γ_{sl} , γ_{lv} correspond to the solid-vapor, solid-liquid and liquid-vapor interfacial energies, respectively.

The surface energy (γ_i) can further be distinguished as a contribution from a dispersive (γ_i^d) and a polar (γ_i^p) component as given by Equation 3.10 [128].

$$\gamma_i = \gamma_i^d + \gamma_i^p \quad (3.10)$$

Furthermore, the total solid-liquid interfacial energy can be expressed by Equation 3.11 [127, 128], which can be determined by measuring the wetting contact angles of two distinguishable liquids.

$$\gamma_{lv}(1 + \cos\theta) = 2(\gamma_{sv}^d \gamma_{lv}^d)^{1/2} + 2(\gamma_{sv}^p \gamma_{lv}^p)^{1/2} \quad (3.11)$$

Paso et al. [127] have identified physical requirements for anti-adhesive coatings to be related to a low surface free energy. Previous studies have shown surface wetting to depend on the ordering of the atomic groups at the surface [129]. Hexagonally packed CF_3 with a surface energy of 6.7 mJ/m^2 , which was assumed to be the lowest possible surface free energy of any solid material, was thus suggested as a model system [127, 128]. Furthermore, the surface energy and wetting of hydrocarbon surfaces have been found to decrease in the order CH_2 groups $>$ CH_3 groups $>$ CF_2 groups $>$ CF_3 groups [129]. The radius of the fluorine atom is small and F has a high electronegativity, which contributes to a strong covalent bond formation with carbon [128]. Siloxanes and fluoropolymers in general have low surface energies [127], and fluorine substitution is considered a viable chemical approach to reducing the surface energy of a material (e.g. coating) due to the low surface energy.

Figure 3.20 displays the measured surface energy which has been obtained for different material systems. It is quite clear that the research is approaching the desired value of 6.7 mJ/m^2 , and thus this limit should be attainable in the near future.

3.5.4 Important parameters for prevention of wax deposition

Wax deposits on the pipe wall at the WAT, and wax deposition is usually counteracted by mechanical methods or by the addition of chemicals. Although methods

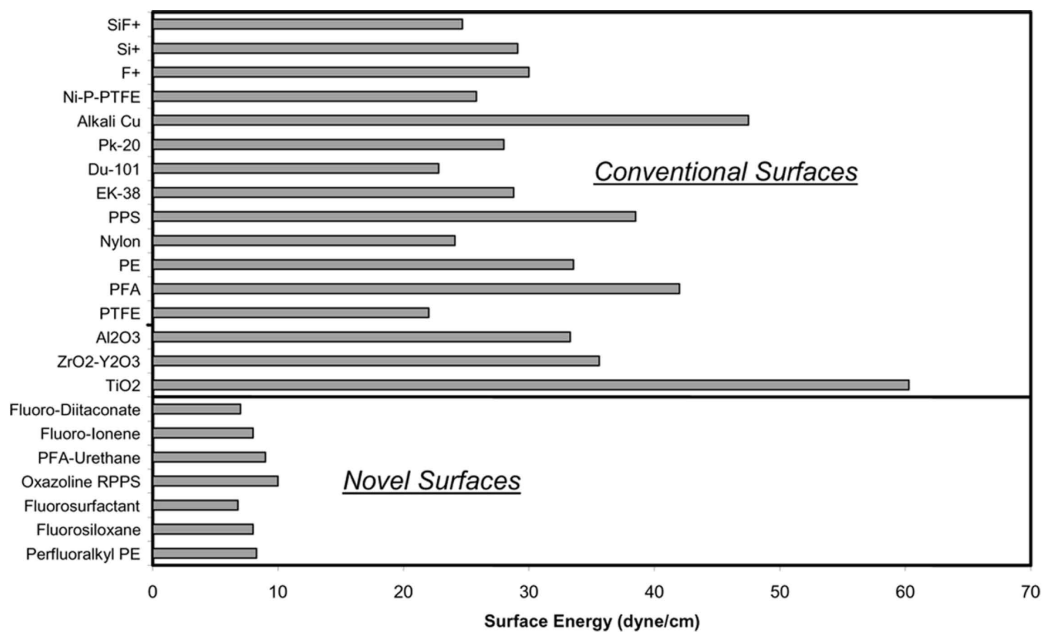


Figure 3.20: Surface energies of conventional and novel coating surfaces, adapted from [127].

have been found that chemically alter the appearance of the wax through addition of surface modifiers to the crude oil, no universal method exists that will successfully prevent wax from depositing on the pipeline. However, tailoring of the pipeline surface with inorganic-organic coatings is an interesting prospect and can potentially be applied to any crude oil regardless of the paraffin composition. As the pipeline walls are usually rough, there are many sites for the wax to adhere. Thus Paso et al. [127] suggested tailoring of smooth surfaces, which should be able to assist in the prevention of wax deposition. Furthermore, hydrophobicity should be promoted at the surface of the pipeline as a high water contact angle will simultaneously reduce the surface tension. Pipeline coatings would benefit from consisting of a significant fraction of CF_3 groups as they have shown to display low surface energy.

Chapter 4

Extended summary of the work

4.1 Preliminary studies

4.1.1 Alkoxide-based silica coatings

Sol-gel synthesis of alkoxide-based silica sols was conducted as a preliminary study of the PhD work according to the acid-catalyzed preparation route (A1) described by Brinker et al. [34]. Tetraethoxysilane (TEOS) was used as precursor, which was dissolved in ethanol and hydrolyzed. Hydrochloric acid was added as catalyst. The sol was applied (1 layer, 4 layers and 6 layers) to stainless steel and carbon steel substrates by dip coating.

Table 4.1 presents the thickness, roughness and contact angle with water values measured for the coated layers of the alkoxide-based silica sol. The measured thickness was the same regardless of the number of layers, and it was suggested that only the first layer adhered to the substrate and the subsequent layers had no effect and could thus be considered parallels of the 1-layered alkoxide-based silica coating. Hence only 1-layered coatings were analyzed with respect to surface roughness and contact angle with water. The 1-layered coating was smooth with a roughness of 4 nm. Furthermore, the contact angle was 39 °, which signified the hydrophilic character of the coating.

Table 4.1: Thickness, roughness and the measured contact angle with water for alkoxide-based silica coatings.

Parallel #	Thickness, μm	Roughness, nm	Contact angle, °
1	0.138 ± 0.005	4 ± 5	39 ± 0.8
2	0.140 ± 0.005	-	-
3	0.141 ± 0.005	-	-

AFM images of the 1-layered alkoxide-based silica coating is displayed in Figure 4.1. The surface was homogeneous (Figure 4.1 (a)) and smooth (Figure 4.1 (b)).

The alkoxide-based silica coatings were characterized with respect to dry abrasion as presented in Figure 4.2. The profiles of the parallels of the 1-layered coating appeared to behave similarly during the dry abrasion test.

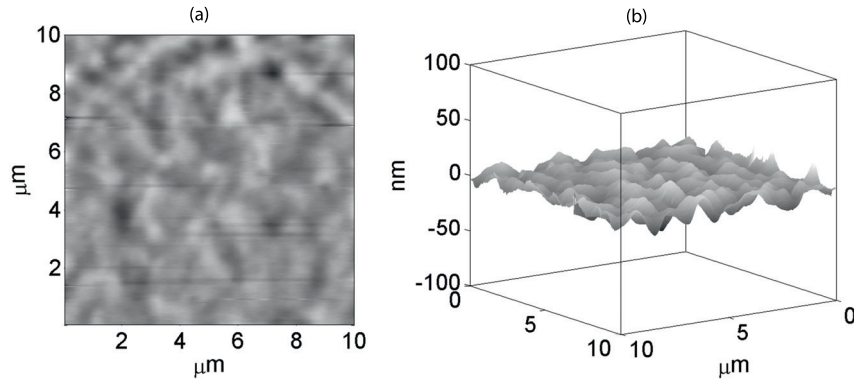


Figure 4.1: AFM images displaying the surface and surface roughness of the 1-layered alkoxide-based silica coating. The images have been smoothed by applying a second degree polynomial fit.

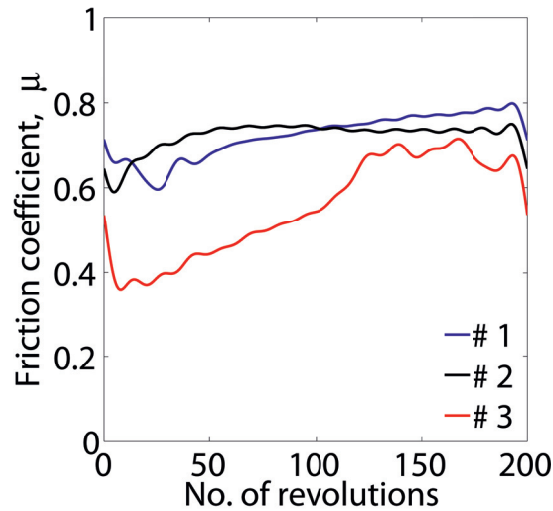


Figure 4.2: Dry abrasion profiles of alkoxide-based silica coatings.

Additionally, the appearance of the tracks developed during dry abrasion were characterized using scanning electron microscopy (SEM). The resulting images of the tracks are provided in Figure 4.3. Figure 4.3 (a), (b) and (c) identify the dry abrasion tracks of the parallels of the 1-layered coatings by parallels number 1, 2 and 3, respectively. The width and features of the tracks resembled each other, which corresponded with the measured dry abrasion profiles in Figure 4.2.

Furthermore, the application of coatings on the surface of steel pipelines require coatings, which can improve the corrosion resistant properties of carbon steel (St52) steel. Figure 4.4 shows the polarization curves recorded for parallels 1 and 3 of the alkoxide-based silica coating on St52 compared with bare St52. It is evident that the

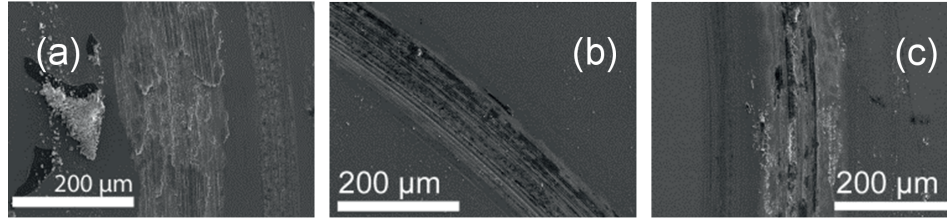


Figure 4.3: SEM images of dry abrasion tracks of alkoxy-based silica coatings constituting (a) 1 layer, (b) 4 layers and (c) 6 layers.

polarization curves of the coatings are similar to the bare St52 both in the cathodic (below -550 mV) and anodic (above -550 mV) regions and thus do not display a shift to lower current density, which is required for anti-corrosion coatings.

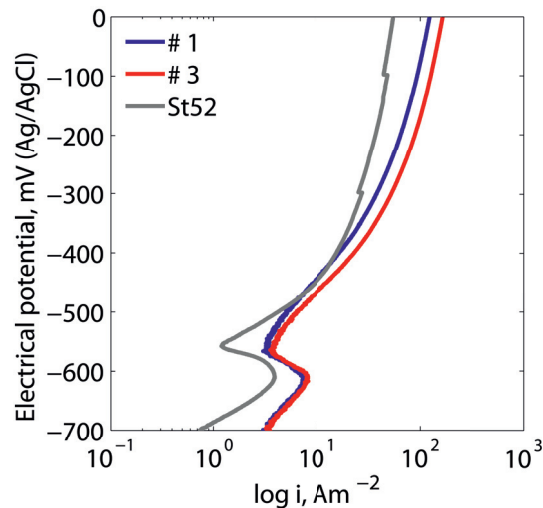


Figure 4.4: Cathodic and anodic polarization curves of two alkoxy-based silica coatings on carbon steel (St52) compared with bare St52.

Corrosion resistant properties of the coatings was deemed essential to the success of the PhD work as part of the Smoothpipe project. Therefore, studies of hybrid inorganic-organic aminopropyl silane-based coatings was initiated.

4.2 Structure of the hybrid aminopropyl silane sols

Sol-gel synthesis of hybrid aminopropyl silane-based sols was conducted as part of the PhD work. γ -APS was used as precursor, which was dissolved in 1-propoxy-2-propanol and subsequently hydrolyzed. The hydrolysis parameters were varied with respect to water/silane ratio, R (R=1.6, 3 and 5), solvent/silane ratio, S (S=0.6, 3 and 6) and pH (0.8 and 6.2). Furthermore, the sols were abbreviated h-xR-yS, where

h refers to a hybrid inorganic-organic sol or coating, x represents the water/silane ratio, R, and y denotes the solvent/silane ratio, S. An additional HCl suffix signified sols (or coatings) synthesized with acidic hydrolysis water (pH=0.8). These sols are also described as acidic sols (or coatings), whereas neutral sols (or coatings) refer to sols (or coatings) synthesized with neutral hydrolysis water. The composition of the sols is provided in Figure 4.5, and a description of all the sols is presented in Table 4.2.

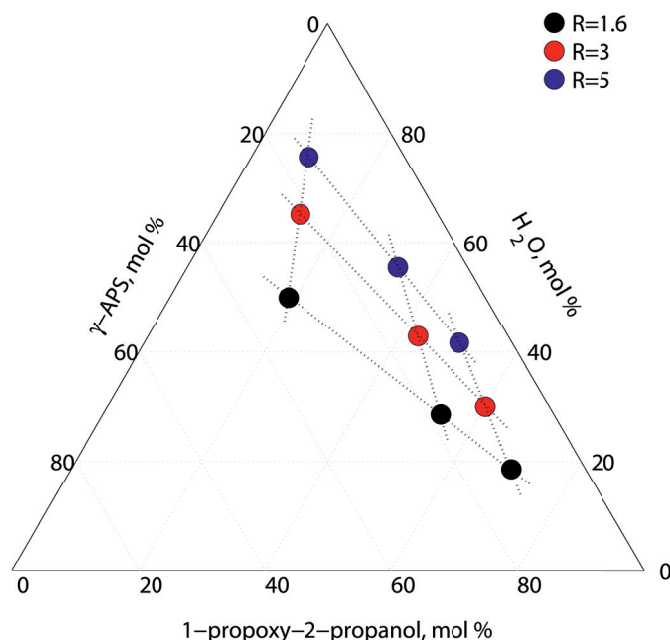


Figure 4.5: Ternary diagram displaying the compositions used for the synthesis of the hybrid inorganic-organic aminopropyl silane-based sols.

Silanes and water are immiscible [22], and the immiscibility of the hybrid aminopropyl silanes was evidenced by the formation of a cloudy sol when the silane was initially mixed with water. A reaction time at elevated temperature (80 °C) was required to dissolve the silane in the aqueous phase rendering the sol transparent. All the sols initially displayed phase separation. The reaction time it took for the phase separation to occur decreased with increasing water/silane ratio, R. This was further reflected by the time it took for the sol to turn transparent; higher water/silane ratio promoted a quicker dissolution reaction. Furthermore, decreasing the pH of the hydrolysis water, which was the case in the acidic sols, increased the reaction time before phase separation was observed, and the acidic sols also required higher temperatures (90 °C) and longer reaction time in order to turn transparent. This behavior reflected the kinetic reactions of the hybrid aminopropyl silane sols as described in Equations 3.1- 3.3. As the amount of water increased, Equation 3.3 shifted to the right and thus increased the solubility of the silane due to more available solvent. In addition, the hydrolysis reaction also produced sol-

Table 4.2: Overview of the variation in the synthesized hydrolyzed aminopropyl silane sols. R is the water/silane ratio, S denotes the solvent/silane ratio and pH refers to the pH of the hydrolysis water, which is also identified by the descriptions of acidic and neutral sols, respectively.

Sol code	R	S	pH	Description
h-1.6R-0.6S-HCl	1.6	0.6	0.8	Acidic hypostoichiometric
h-1.6R-3S-HCl	1.6	3	0.8	Acidic hypostoichiometric
h-1.6R-6S-HCl	1.6	6	0.80	Acidic hypostoichiometric
h-3R-0.6S-HCl	3	0.6	0.8	Acidic stoichiometric
h-3R-3S-HCl	3	3	0.8	Acidic stoichiometric
h-3R-6S-HCl	3	6	0.8	Acidic stoichiometric
h-1.6R-0.6S	1.6	0.6	6.2	Neutral hypostoichiometric
h-1.6R-3S	1.6	3	6.2	Neutral hypostoichiometric
h-1.6R-6S	1.6	6	6.2	Neutral hypostoichiometric
h-3R-0.6S	3	0.6	6.2	Neutral stoichiometric
h-3R-3S	3	3	6.2	Neutral stoichiometric
h-3R-6S	3	6	6.2	Neutral stoichiometric
h-5R-0.6S	5	0.6	6.2	Neutral hyperstoichiometric
h-5R-3S	5	3	6.2	Neutral hyperstoichiometric
h-5R-6S	5	6	6.2	Neutral hyperstoichiometric

vent (Equation 3.1). Furthermore, it is proposed that the acidic hypostoichiometric sols (water/silane ratio less than 2) condense via water-producing condensation as described in Equation 3.2 producing more water as the reaction proceeds thus decreasing the solubility. Additionally, the local pH decrease would also decrease the silane solubility according to Brinker and Scherer [22]. The kinetic mechanisms of the hydrolysis and condensation reactions therefore explain the difference in reaction time in order to obtain transparent sols.

In order to further study the initial hydrolysis and condensation reactions, ^1H nuclear magnetic resonance (NMR) spectroscopy was conducted on a selection of the sols. Two types of sol synthesis procedures were studied; the chemicals were either mixed with immediate spectrum acquisition (fresh sols), or the chemicals were mixed and reacted at 80 °C for 1 h followed by cooling (approximately 2 h) before spectra were recorded (aged sols). The hybrid aminopropyl silane sols studied by NMR are listed in Table 4.3.

Table 4.3: Description of the sols studied by NMR spectroscopy.

Sol code	Water/silane ratio	Description
h-1.6R-0.6S-HCl	1.6	Acidic hypostoichiometric
h-1.6R-0.6S	1.6	Neutral hypostoichiometric
h-3R-0.6S	3	Neutral stoichiometric
h-5R-0.6S	5	Neutral hyperstoichiometric

Figure 4.6 shows the ^1H NMR spectra that were acquired of the fresh sols, and the spectrum of pure γ -APS is displayed along with the assigned signals (Figure 4.6 (a)). The initial behavior of the sol reaction was different in the acidic (and neutral) hypostoichiometric sol compared to the stoichiometric and hyperstoichiometric sols as illustrated in Figure 4.6. By inspection of the spectra of the fresh sols in Figure 4.6, it can be seen that the stoichiometric and hyperstoichiometric sols (Figure 4.6 (d) and (e)) early developed a significant peak at 4.4-4.6 ppm, which was ascribed to OH groups, whereas the distinct signal arising from CH_3 in $\text{Si}-\text{O}-\text{CH}_2-\text{CH}_3$ was initially present with a high intensity in the hypostoichiometric sols (Figure 4.6 (b) and (c)), which reflected a significant fraction of γ -APS. The absence of the γ -APS signal suggested a fast hydrolysis and condensation reaction in the stoichiometric and hyperstoichiometric sols. After 24 h of reaction time, a signal in the range of 4.4-4.8 ppm was detected in all the fresh sols, but the signal was located at higher chemical shifts with increasing water/silane ratio.

Furthermore, the ^1H NMR spectra of the aged sols are provided in Figure 4.7. The spectra of the aged sols appear similar regardless of the water/silane ratio. However, as was observed for the fresh sols (Figure 4.6), the spectra in Figure 4.7 clearly displayed a strong signal in the range of 4.5-4.7 ppm, which was also detected at higher chemical shift values with increasing water/silane ratio.

The hydrolysis and condensation reactions of the hybrid aminopropyl silane sols were further studied by ^{29}Si NMR, and spectra of the fresh hybrid aminopropyl silane sols are presented in Figure 4.8. The acquired spectrum of pure γ -APS, which has a distinct signal at -45 ppm (T_{R}^0), is displayed in Figure 4.8 (a), and the feature is ascribed to the presence of unhydrolyzed ethoxy groups. In ^{29}Si NMR, hydrolyzed γ -APS (T_{H}^0) should be detected at -43 ppm.

T_{R}^0 is initially present in all the fresh sols at $t=0$ h (Figure 4.8 (b)-(e)), which reflects a slow hydrolysis and/or fast condensation reaction. However, as distinct signals were detected for more condensed species (i.e. T^1 , T^2 and T^3), it can be assumed that the condensation reaction was fast thus compromising hydrolysis. Furthermore, Figure 4.8 (b) displays ^{29}Si NMR spectra of the acidic hypostoichiometric sol. It is apparent that a signal at -43 ppm (T_{H}^0) was detected in this acidic sol. The presence of T_{H}^0 demonstrated hydrolysis of γ -APS, which in turn indicated a slower condensation reaction compared to the neutral sols (Figure 4.8 (c)-(e)).

Figure 4.8 also demonstrates that more condensed species (T^1 , T^2 and T^3) were formed as the reaction time of the sols increased. After 24 h the stoichiometric and hyperstoichiometric sols were generally composed of T^2 and T^3 (Figure 4.8 (d) and (e)), while the hypostoichiometric sols mainly constituted T_{R}^0 (acidic sol), T^1 , T^2 and T^3 (Figure 4.8 (b) and (c)).

^{29}Si NMR spectra of the aged sols are displayed in Figure 4.9. The ^{29}Si NMR spectra of the stoichiometric and hyperstoichiometric sols are shown in Figure 4.9 (c) and (d). Starting at $t=3$ h, these sols were mainly composed of T^2 and T^3 species. A prolonged reaction time up to 4 months did not decrease the fraction of T^2 on behalf of T^3 as was the case for the hypostoichiometric sols. The hypostoichiometric sols in Figure 4.9 (a) and (b) were composed of T_{R}^0 (acidic sol), T^1 and T^3 at $t=24$ h. A minor contribution from T^2 was also detected. However, when the reaction time

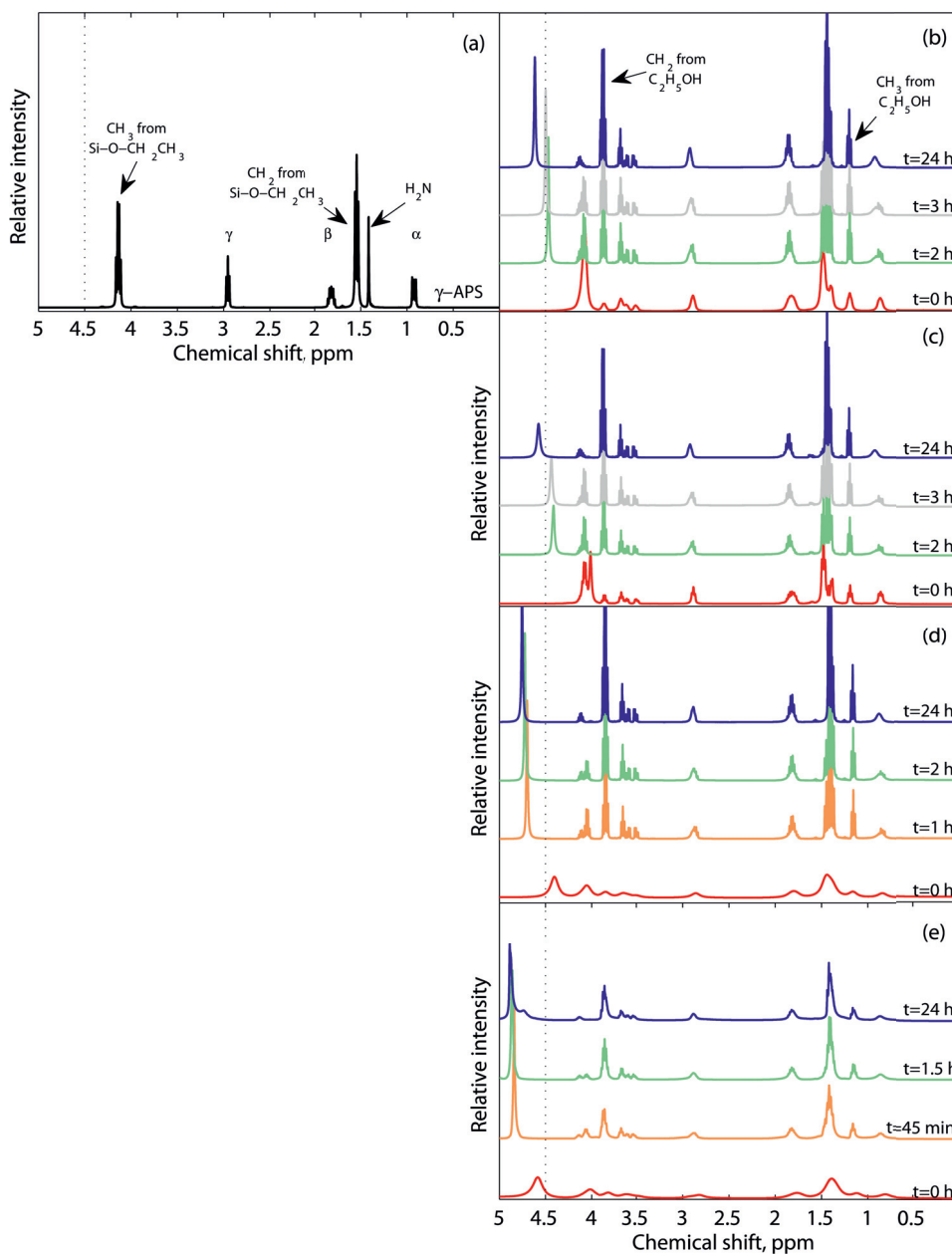


Figure 4.6: ^1H NMR spectra of a selection of fresh hybrid aminopropyl silane-based sols in Figure 4.5. (a) Pure γ -APS, (b) acidic hypostoichiometric sol, (c) neutral hypostoichiometric sol, (d) neutral stoichiometric sol, and (e) neutral hyperstoichiometric sol. The dotted line at 4.5 ppm serves as a guide to the eye.

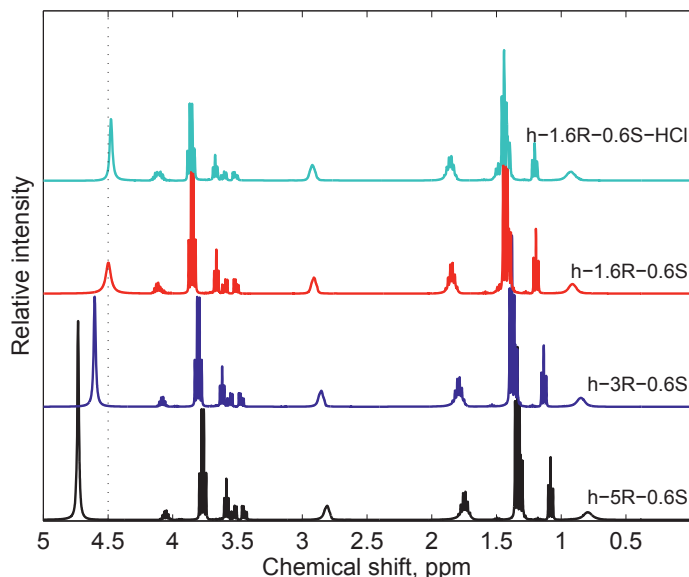


Figure 4.7: ^1H NMR spectra of a selection of aged hybrid aminopropyl silane-based sols in Figure 4.5. The dotted line serves as a guide to the eye.

was increased to 4 months, the less condensed species were found to have reacted and formed T^3 species.

The relative distribution of T^n species in the fresh and aged sols as the hydrolysis and condensation reactions proceeded is illustrated in Figure 4.10. At first, at $t=1$ h the fresh neutral sols were all composed of a large fraction of T_R^0 as displayed in Figure 4.10 (a). The condensation reaction ensured that the neutral stoichiometric and hyperstoichiometric sols were mainly composed of T^2 and T^3 species after 24 h (Figure 4.10 (b)). The condensation of the aged neutral sols is similarly provided in Figure 4.10 (c) and (d). Initially, T_R^0 constituted a significant fraction in the aged sols, but after 24 h, more condensed species such as T^2 and T^3 were formed. Furthermore, the acidic hypostoichiometric sol constituted a larger fraction of T_R^0 and T^1 compared to the neutral hypostoichiometric sol, as displayed in Figure 4.10 (d).

An important piece of the puzzle was thus found by ^1H and ^{29}Si NMR spectroscopy. However, Fourier transform infrared (FTIR) spectroscopy was also found to be a useful tool. FTIR transmission spectra of the aged neutral hybrid aminopropyl silane sols with varying water/silane ratio, R , are shown in Figure 4.11. Bands at 882, 959, 1050, 1380 and 2970 cm^{-1} were assigned to ethanol, which increased with increasing water/silane ratio. Unhydrolyzed ethoxy groups in γ -APS were detected at 959 and 1359 cm^{-1} . The intensity of these bands decreased with increasing water/silane ratio, which indicated an extended condensation reaction of γ -APS in the hyperstoichiometric aged sol ($R=5$) compared to the hypostoichiometric aged

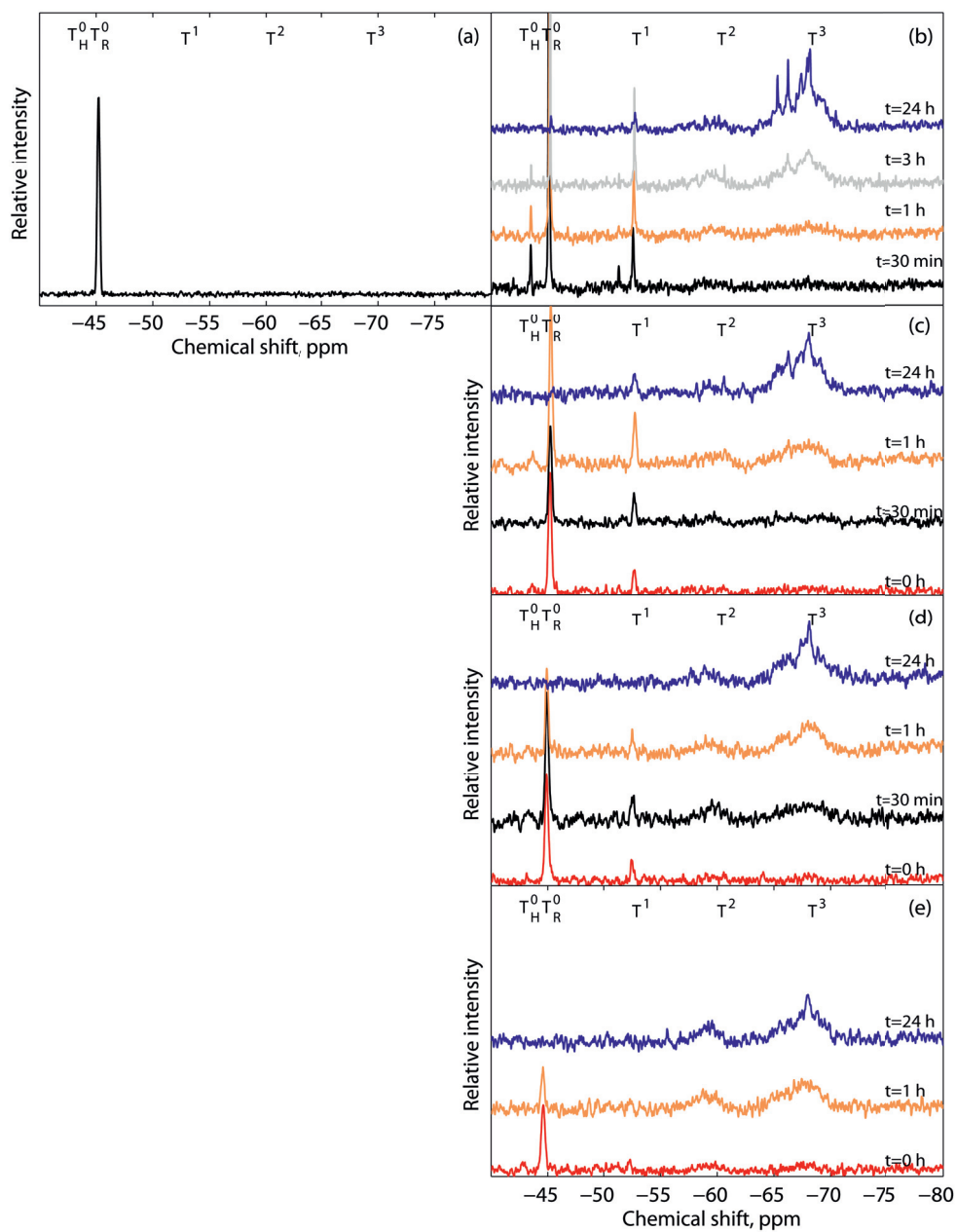


Figure 4.8: ^{29}Si NMR spectra of fresh hybrid aminopropyl silane-based sols in Figure 4.5. (a) Pure γ -APS, (b) acidic hypostoichiometric sol, (c) neutral hypostoichiometric sol, (d) neutral stoichiometric sol and (e) neutral hyperstoichiometric sol.

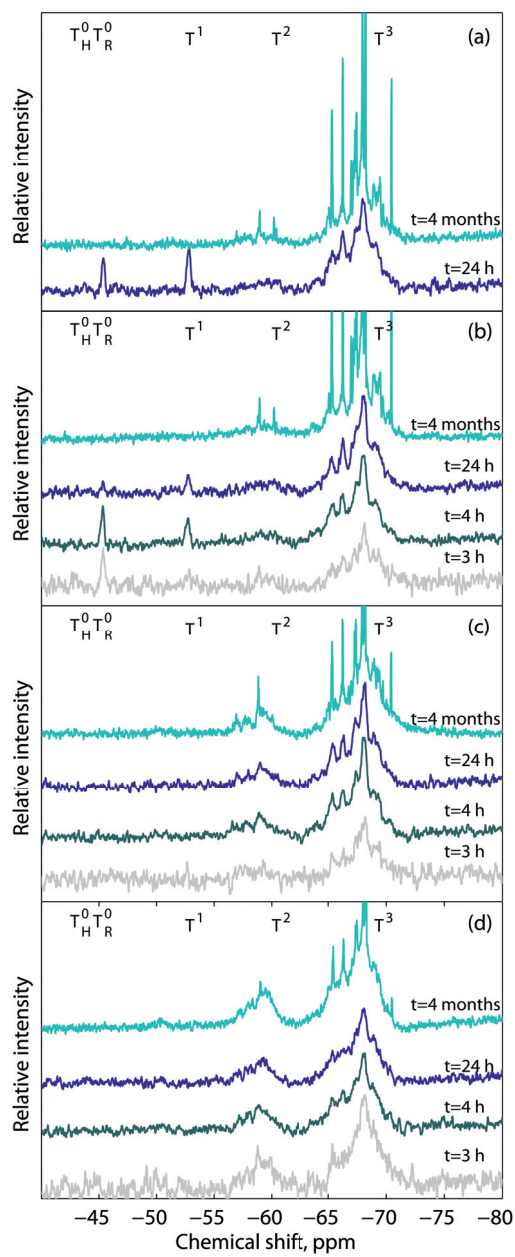


Figure 4.9: ^{29}Si NMR spectra of aged hybrid aminopropyl silane-based sols in Figure 4.5. (a) acidic hypostoichiometric sol, (b) neutral hypostoichiometric sol, (c) neutral stoichiometric sol and (d) neutral hyperstoichiometric sol.

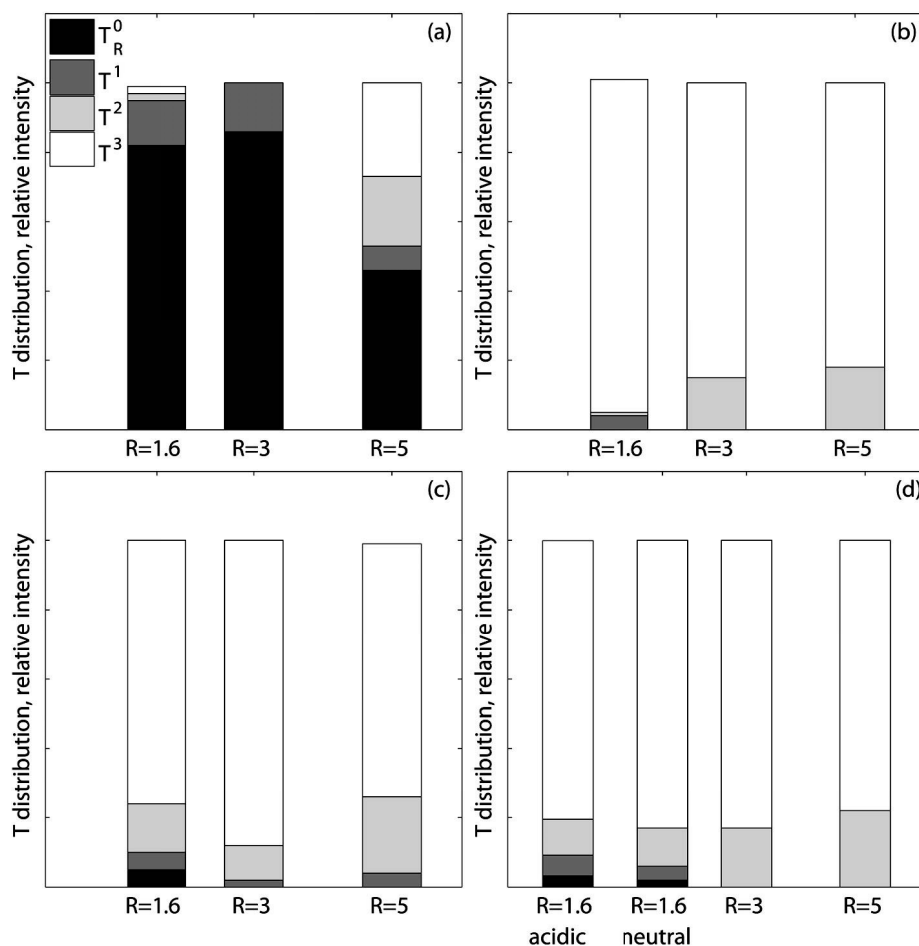


Figure 4.10: T^n species distribution of fresh sols at (a) $t=1$ h and (b) $t=24$ h and aged sols at (c) $t=3$ h and (d) $t=24$ h with varying water/silane ratio, R , derived from the respective ^{29}Si NMR spectra of the hybrid aminopropyl silane-based sols.

sol ($R=1.6$).

Si-O bands appeared in the range from 930 to 1200 cm^{-1} . The Si-O band at 930 cm^{-1} decreased in intensity with increasing water/silane ratio. Strong bands ascribed to siloxane (Si-O-Si) stretching were detected in the range 1095 to 1125 cm^{-1} . At 1650 cm^{-1} , a water band was observed, which augmented with increasing water/silane ratio. Methylene stretching in γ -APS was observed at 2875 , 2930 and 2970 cm^{-1} . The band at 1380 cm^{-1} was related to methylene deformation modes in the propylamine groups [44]. Bands due to amine groups were detected at several frequencies (789 , 1600 , 3290 and 3359 cm^{-1}). The band near 1600 cm^{-1} was attributed to the NH_2 of a primary amine [130]. As Equation 3.3 demonstrated the formation of alcohol (ethanol) during condensation, it can be assumed that the

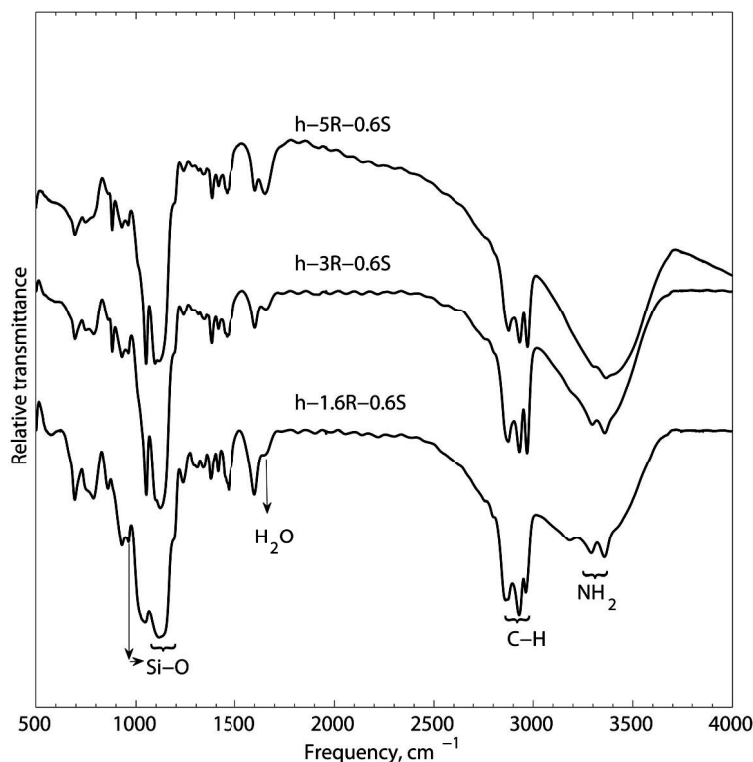


Figure 4.11: FTIR spectra of aged neutral aminopropyl silane-based sols.

ethanol signal arose as a result of the condensation reaction, which would have formed more Si-O-Si bonds. The evolution of Si-O-Si bonds was signified by the presence of T^2 and T^3 species in the ^{29}Si NMR spectra. Thus FTIR showed similar behavior in the sols as NMR.

^{29}Si NMR spectroscopy has shown that the extent of hydrolysis and condensation reactions in hybrid aminopropyl silane sols were related to the water/silane ratio and the pH of the hydrolysis water. The hydrolysis of the acidic hypostoichiometric sol was evidenced by a signal arising from hydrolyzed silane, which also suggested a slower condensation reaction, whereas the condensation reaction in the neutral sols was fast compared to hydrolysis. Furthermore, the condensation rate of the neutral stoichiometric and hyperstoichiometric sols was fast as signified by the early development of T^2 and T^3 species. The condensation rate in the acidic and neutral hypostoichiometric sols was slower, and less condensed species such as T^1 remained in the sols for at least 24 h. The acidic hypostoichiometric sol also displayed unhydrolyzed γ -APS even after 24 h of reaction, which clearly demonstrated the slower hydrolysis and condensation reactions in this sol.

4.3 Rheological properties of the hybrid aminopropyl silane-based sols

The rheological properties of the hybrid aminopropyl silane sols were studied with respect to the effect of water/silane ratio, solvent/silane ratio and hydrolysis pH. Table 4.4 relates the measured viscosity to the sol parameters and the structural composition of aged sols.

Table 4.4: Viscosity of aged sols correlated with the degree of condensation as detected (assigned Tⁿ Si species) by ²⁹Si NMR spectroscopy of 4 months aged sols.

Sol code	Water/silane ratio	Viscosity, Pas	²⁹ Si NMR species
h-1.6R-0.6S-HCl	1.6	0.035 ± 0.0004	Mainly T ³
h-1.6R-0.6S	1.6	0.046 ± 0.0006	Mainly T ³
h-1.6R-6S	1.6	0.011 ± 0.0005	-
h-5R-0.6S	5	0.089 ± 0.0005	T ² and T ³
h-5R-6S	5	0.015 ± 0.0002	-

The viscosity of the hybrid aminopropyl silane-based sols is provided in Figure 4.12. Figure 4.12 (a) displays the viscosity as a function of shear rate, while in Figure 4.12 (b) the effect of shear rate on the shear stress is elaborated. Figure 4.12 (a) demonstrates that three parameters significantly influenced the sol viscosity. For one, increasing the amount of solvent (solvent/silane ratio, S) reduced the viscosity as was seen by comparing h-1.6R-0.6S with h-1.6R-6S and h-5R-0.6S with h-5R-6S, which was as expected due to a decrease in the silane concentration. Furthermore, increasing the water/silane ratio, increased the viscosity significantly (h-1.6R-0.6S vs. h-5R-0.6S). The difference in viscosity (0.046 vs. 0.089 Pas) signified a more cross-linked structure for the highest water/silane ratio, which was in correlation with the observed presence of a large fraction of T² in addition to T³ species in the aged hyperstoichiometric sol after 4 months as was demonstrated with ²⁹Si NMR spectroscopy in Figure 4.9 (d). Furthermore, Figure 4.12 demonstrates that a decreasing sol pH was able to reduce the viscosity, 0.046 vs. 0.035 Pas, which indicates a more linear sol structure with decreasing pH. A linear sol structure is in accordance with the recorded ²⁹Si NMR spectra of the aged acidic hypostoichiometric sol (Figure 4.9 (b)), which displayed T³ species as the main constituent in the aged acidic sol after 4 months. Furthermore, a linear dependence of the shear rate on the shear stress is evident in Figure 4.12 (b), which demonstrated Newtonian behavior in the aged sols. Additionally, for a given water/silane ratio, R, the silane concentration was shown to affect the viscosity as depicted in Figure 4.12 (c). Decreasing pH in combination with the mol % silane was also shown to decrease the viscosity.

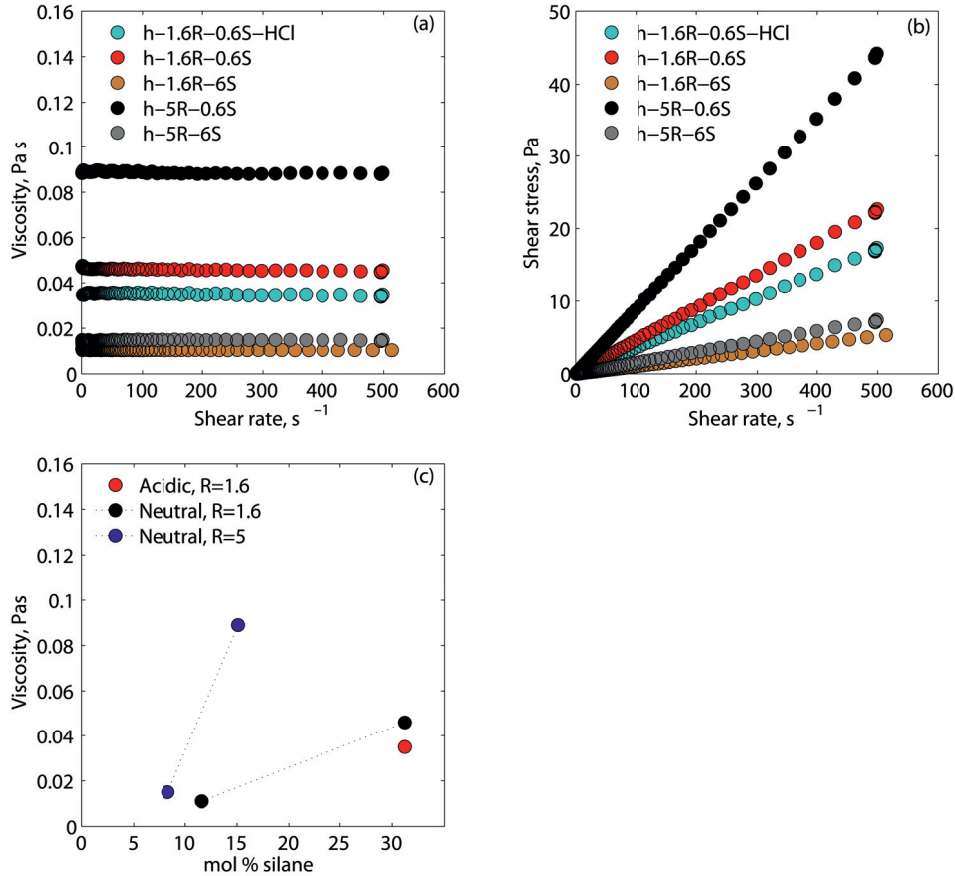


Figure 4.12: Viscosity of the hybrid aminopropyl silane-based sols as a function of (a) shear stress and (c) mol % silane. (b) shows the shear stress as a function of shear rate.

4.4 Coating thickness of the hybrid aminopropyl silane-based coatings

The acidic and neutral hybrid aminopropyl silane-based sols were deposited on stainless steel substrates by dip coating. A thermal treatment at 160 °C for 3 h was then conducted in order to evaporate water and solvent from the deposited coatings. The dry thickness of the hybrid aminopropyl silane coatings on stainless steel is shown in Figure 4.13. Figure 4.13 (a) displays the thickness dependence of the acidic coatings on the silane concentration, whereas Figure 4.13 (b) illustrates the neutral coating thickness as a function of the silane concentration. The thickness variation with increasing viscosity and mol % silane is illustrated in Figure 4.13 (c) and (d), respectively. The coating thickness was related to the sol viscosity (Figure 4.13 (c)), and the thickness increased with increasing viscosity for a given water/silane ra-

tio. The acidic coatings (Figure 4.13 (d)) were generally thinner than the neutral coatings for the same silane concentration, which supports the assumption that the acidic coatings were dense as a result of a linearly chained sol structure deduced from ^{29}Si NMR.

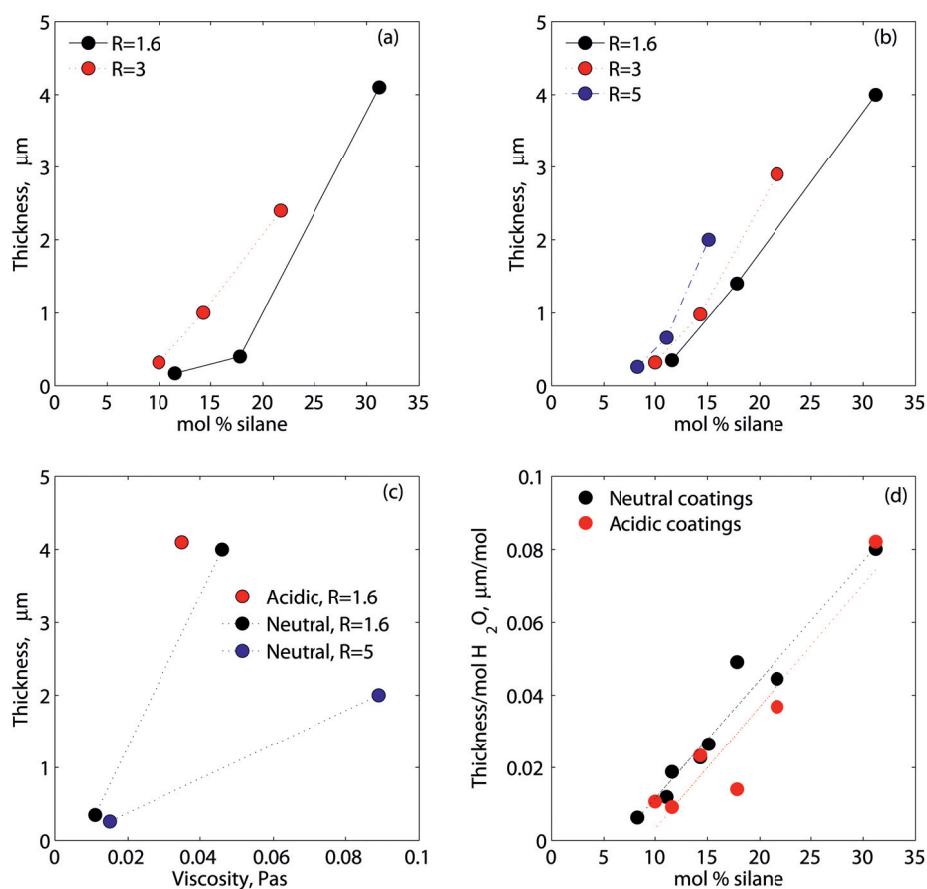


Figure 4.13: Thickness of the hybrid aminopropyl silane-based coatings on stainless steel AISI 304 substrates as a function of mol % silane for the (a) acidic and (b) neutral coatings. (c) reflects the coating thickness as a function of viscosity, while (d) presents the thickness/mol H_2O vs. mol % silane.

Based on the findings, it can be concluded that the thickness of the coatings can be tailored within the range 0.3 to approximately 4 μm .

4.5 Physical properties of the hybrid aminopropyl silane-based coatings

The BET surface area of a selection of the hybrid aminopropyl silane-based gels and their respective cumulative pore volumes are reported in Table 4.5. The gels displayed a low surface area and a low pore volume. Additionally, the nitrogen adsorption and desorption isotherms of the same silane-based gels are provided in Figure 4.14. The isotherms of the gels were characteristic of a non-porous solid (probably a type 2 isotherm), which is typical for a non-porous silica [85]. Although the detected pore volume was low, the adsorption-desorption hysteresis isotherms indicated the presence of pores. However, since the pore volume and surface area were low, it was assumed that the acidic and neutral hybrid aminopropyl silane-based coatings were dense.

Table 4.5: A selection of hybrid aminopropyl silane-based gels and their respective BET surface areas and BJH adsorption cumulative volume of pores between 1.7 and 300 nm diameter. In addition, the standard deviation of the surface area and pore volume is provided.

Gel code	BET surface area, m ² /g	Pore volume ($\cdot 10^{-4}$), cm ³ /g
h-1.6R-0.6S-HCl	0.0970 \pm 0.02	0.767 \pm 0.04
h-1.6R-6S-HCl	0.1808 \pm 0.01	5.31 \pm 0.4
h-3R-0.6S-HCl	0.417 \pm 0.09	6.85 \pm 1
h-3R-6S-HCl	0.1652 \pm 0.03	1.30 \pm 0.04
h-5R-0.6S	0.0975 \pm 0.009	7.20 \pm 6
h-5R-6S	0.1778 \pm 0.06	4.81 \pm 3

Surface roughness of the hybrid aminopropyl silane-based coatings was evaluated using atomic force microscopy (AFM). Figure 4.15 shows the surface and the surface roughness of a selection of the coatings. Figures 4.15 (a) and (b) display the surface and the surface roughness, respectively, of two acidic hybrid aminopropyl silane-based coatings. The corresponding neutral coatings are illustrated in Figure 4.15 (c) and (d). The coatings were generally smooth, homogeneous and crack-free. Due to the organic moiety the thickness of the coatings was able to exceed the limit of 1 μ m, which is generally the case for pure inorganic coatings [18, 22, 43].

The contact angle with water of the hybrid aminopropyl silane-based coatings is displayed in Figure 4.16, and the contact angle was seen to vary from 65 to 80 $^{\circ}$. Water contact angles below 90 $^{\circ}$ are identified as hydrophilic. However, pentadecane was shown to wet the coatings, which demonstrated that the coatings also exhibited a hydrophobic character.

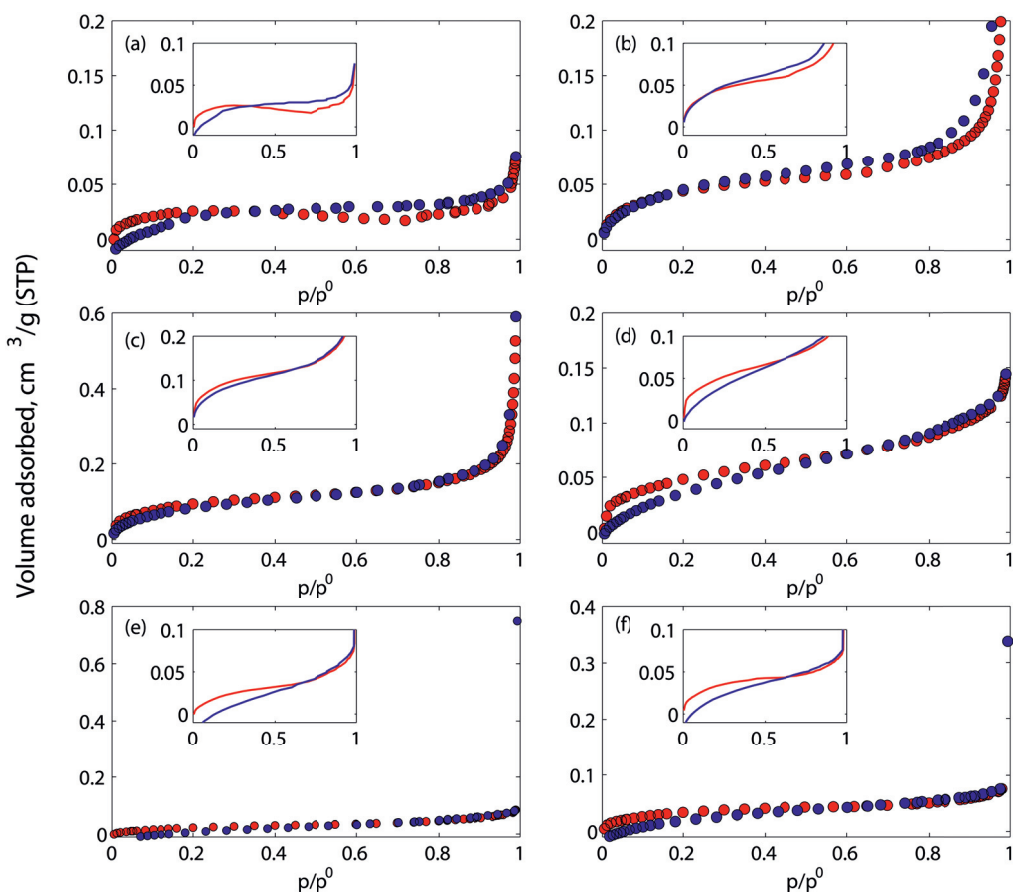


Figure 4.14: Adsorption and desorption isotherms for gels of (a) h-1.6R-0.6S-HCl, (b) h-1.6R-6S-HCl, (c) h-3R-0.6S-HCl, (d) h-3R-6S-HCl, (e) h-5R-0.6S and (f) h-5R-6S. The red dots and lines reflect adsorption isotherms whereas the blue dots and lines represent desorption isotherms. The insets disclose a close-up of the adsorption-desorption hysteresis.

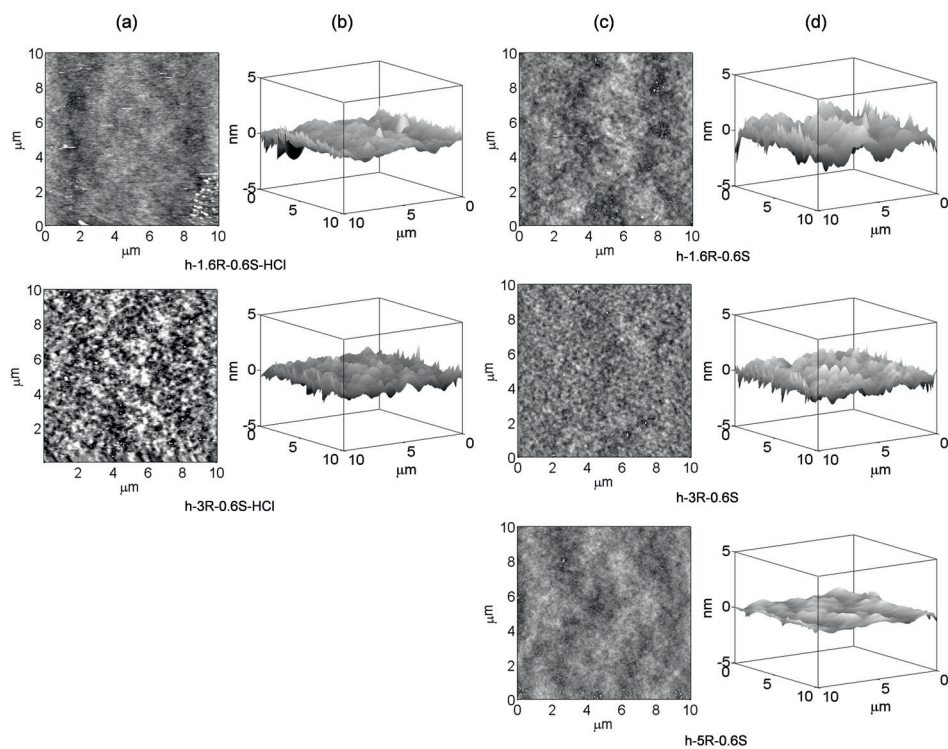


Figure 4.15: AFM images displaying the surface of the acidic (a) and neutral (c) hybrid aminopropyl silane-based coatings. The images of the corresponding surface roughness in (b) and (d) have been smoothed using a second degree polynomial fit.

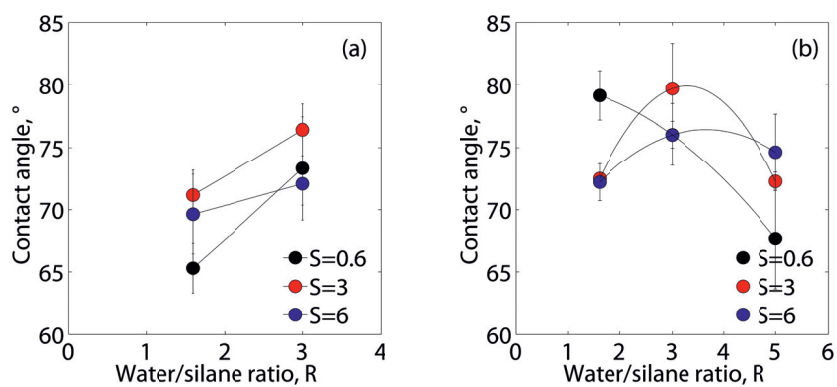


Figure 4.16: Contact angle of the neutral hybrid aminopropyl silane-based coatings. (a) acidic coatings and (b) neutral coatings.

4.6 Abrasion characterization of the hybrid aminopropyl silane-based coatings

Pin-on-disc tribology was used to study the dry abrasion properties of the hybrid aminopropyl silane-based coatings. During the dry abrasion studies, abrasion tracks were induced in the coatings, and the appearance of these tracks are provided in Figure 4.17 for a selection of the coatings. The dry abrasion studies showed two different types of behavior in the hybrid aminopropyl silane coatings; smearing (Figure 4.17 (a)) and delamination (Figure 4.17 (b)). The observed type of behavior for each coating is summarized in Table 4.6.

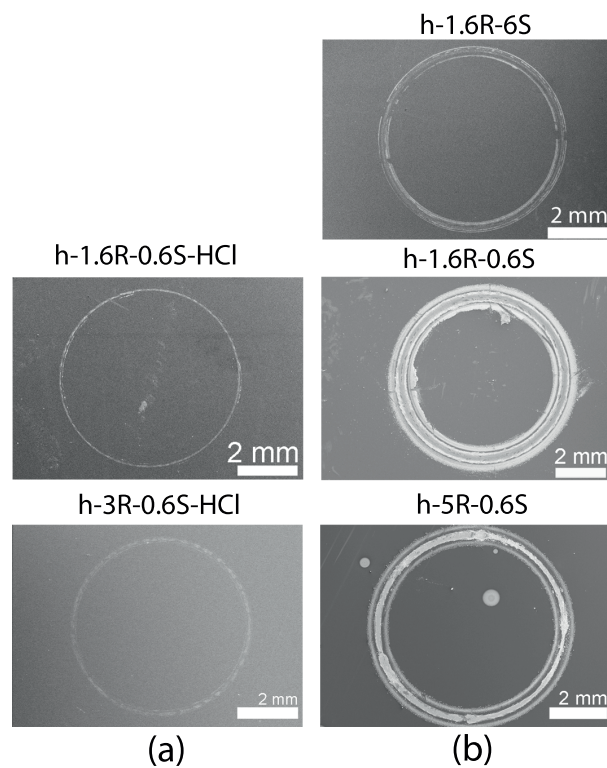


Figure 4.17: Appearance of abrasion tracks of the coatings that were exposed to dry abrasion. (a) and (b) display smearing and delaminating behavior, respectively.

The smearing type behavior was characterized by the limited removal of material after the dry abrasion shown by the thin circles in Figure 4.17 (a). The coatings categorized with a delaminating type of behavior (Figure 4.17 (b)) were removed from the substrate after the dry abrasion, and the substrate was visible. The acidic coatings generally displayed smearing type behavior.

Examples of typical dry abrasion profiles are provided in Figure 4.18. The shape of the dry abrasion profile was similar for the three coatings, but the value of the

Table 4.6: Abrasion appearance of selected hybrid aminopropyl silane-based coatings. The thickness of the coatings in addition to surface roughness (Ra) is provided as well.

Coating code	Abrasion appearance	Thickness, μm	Ra, nm
h-1.6R-0.6S-HCl	Smearing	4.1 ± 0.6	0.67
h-1.6R-3S-HCl	Partial delamination	0.40 ± 0.02	5.5
h-1.6R-6S-HCl	Delamination	0.17 ± 0.05	0.60
h-3R-0.6S-HCl	Smearing	2.4 ± 0.3	0.44
h-3R-3S-HCl	-	1.0 ± 0.07	0.57
h-3R-6S-HCl	Smearing	0.32 ± 0.004	0.51
h-1.6R-0.6S	Delamination	4.0 ± 0.09	0.67
h-1.6R-3S	-	1.4 ± 0.06	9.3
h-1.6R-6S	Smearing	0.35 ± 0.05	0.60
h-3R-0.6S	Smearing	2.9 ± 0.4	0.60
h-3R-3S	-	0.98 ± 0.02	1.1
h-3R-6S	Partial delamination	0.32 ± 0.002	1.0
h-5R-0.6S	Delamination	2.0 ± 0.05	0.21
h-5R-3S	Smearing	0.66 ± 0.06	0.39
h-5R-6S	Partial delamination	0.26 ± 0.02	0.36

friction coefficient varied. The appearance of the tracks after the dry abrasion are inserted in Figure 4.18. The SEM images show the abrasion tracks after 500 revolutions. The dry abrasion profiles correlated with the appearance of the tracks; the highest friction profile (h-5R-0.6S) displayed delamination, whereas smearing was observed for the lowest friction profile (h-5R-3S). The last coating displayed a friction behavior in between the other two and consequently was partially delaminated.

The smearing and delaminating types of behavior will serve different purposes as coatings. Whereas a smearing type coating can still offer chemical protection if the coating is covering the whole surface of the substrate, the delaminated coating will not be able to provide any further protection of the steel substrate.

^{29}Si NMR demonstrated a difference in structural composition between the acidic and neutral coatings as well as a structural dependence of the water/silane ratio (hypostoichiometric vs. hyperstoichiometric). The acidic hypostoichiometric aged sol was composed of mainly T^3 , whereas both T^2 and T^3 were present in the aged neutral hyperstoichiometric sol. As shown in Figure 3.5, the structural difference in the sols will also significantly affect the structural features in the respective coatings. The acidic hypostoichiometric sol was shown to be composed of linear chains (Figures 4.9 and 4.12) and was assumed to result in a dense coating, whereas the neutral hyperstoichiometric sol demonstrated a cross-linked behavior owing to the large fraction of T^2 and T^3 species and the significantly higher viscosity (Figures 4.9 and 4.12). Cross-linked sols are usually the starting point for obtaining porous coatings [19]. The acidic hypostoichiometric and neutral hyperstoichiometric sols are proposed to have been two extremities of the studied hybrid aminopropyl silane sols (or coatings), and the neutral hypostoichiometric and neutral stoichiometric

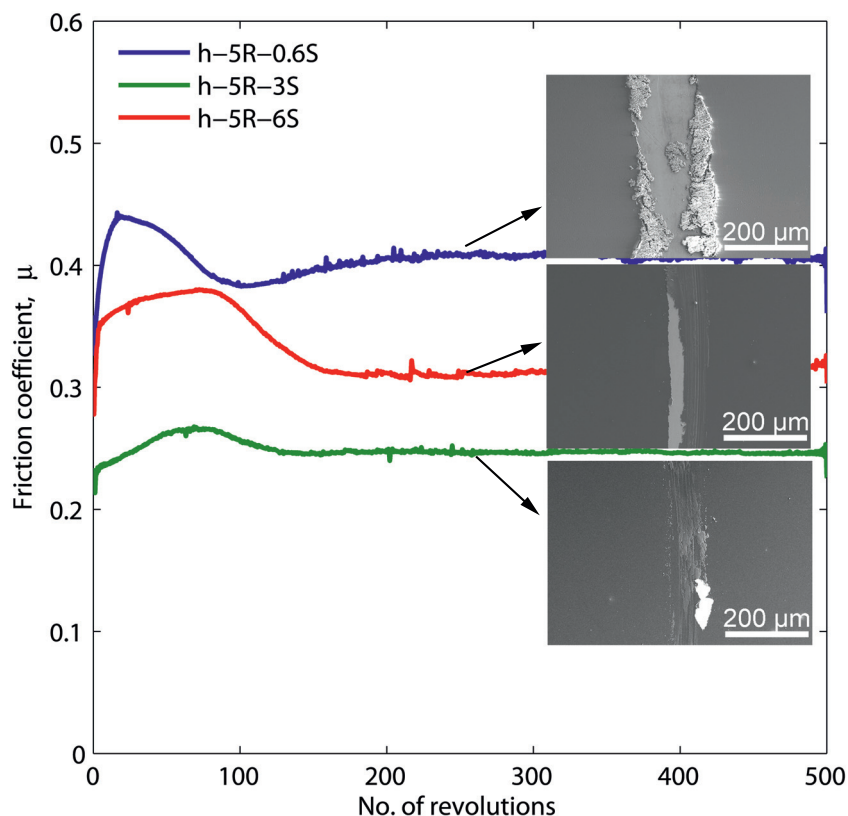


Figure 4.18: Dry abrasion profiles for neutral hybrid aminopropyl silane-based coatings with constant water/silane ratio, $R=5$, and varying solvent/silane ratio, S . Periodic noise has been removed by a Fourier transform low pass filter.

sols are located in between these two as far as coating structure is concerned. The dense coating (h-1.6R-0.6S-HCl) arising from the acidic sol was demonstrated by a smearing type abrasion track appearance whereas the hyperstoichiometric neutral sol (h-5R-0.6S) exhibited delamination during dry abrasion.

4.7 Corrosion protection of hybrid aminopropyl silane coatings on carbon steel

4.7.1 Electrochemical polarization studies

Crude oil in subsea pipelines is subjected to corrosion by the fluid either due to particle impact (abrasion) or due to the electrolyte. For long-term operation of pipelines it is therefore a prerequisite that the pipelines can sustain the environmental impact from the ambient surroundings.

Electrochemical polarization studies were initiated in order to study the possibility of long-term corrosion protection of the hybrid aminopropyl silane coatings on carbon steel. Figure 4.19 shows the polarization curves of the hybrid aminopropyl silane coatings on carbon steel (St52). Corrosion protection is achieved for coatings with a smaller current density than St52 in Figure 4.19.

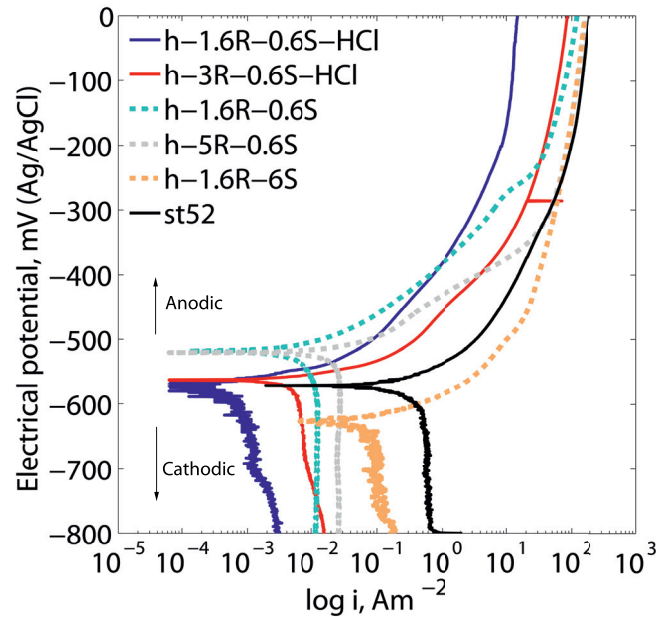


Figure 4.19: Electrochemical polarization plots of the hybrid aminopropyl silane-based coatings compared with carbon steel (St52).

All the coatings displayed smaller current density than St52 in the cathodic region (below -550 mV) in Figure 4.19. The anodic region (above -550 mV) can be divided in two. Below -250 mV, the coatings displayed less current density than carbon steel, but above -250 mV, the neutral coatings were either approaching (h-1.6R-0.6S) or were displaying the same current density values as carbon steel. In this region, the neutral coatings were not able to protect the carbon steel from corrosion. However, the acidic coatings behaved differently. Above -250 mV, these coatings were still at lower current density compared to St52, and the acidic coatings were thus able to offer corrosion protection in the anodic region.

Figure 4.20 displays images of the coatings after the polarization study in Figure 4.19. Figure 4.20 indicates three types of behavior of the coating exposed to electrolyte during the polarization. Figure 4.20 identifies the behaviors as (a) localized spots of corrosion in the acidic coatings, (b) partial neutral coating disruption and (c) neutral coating delamination. The neutral coatings were either partially or fully delaminated (Figure 4.20 (b) and (c)), which is in accordance with the high registered current density in the anodic region in Figure 4.19. Judging from the polarization curves (Figure 4.19), it is thus apparent that the acidic coatings can

increase the corrosion resistance of carbon steel, though the protection will be limited as demonstrated by the localized corrosion spots that occurred in the acidic coatings during polarization (Figure 4.20 (a)).

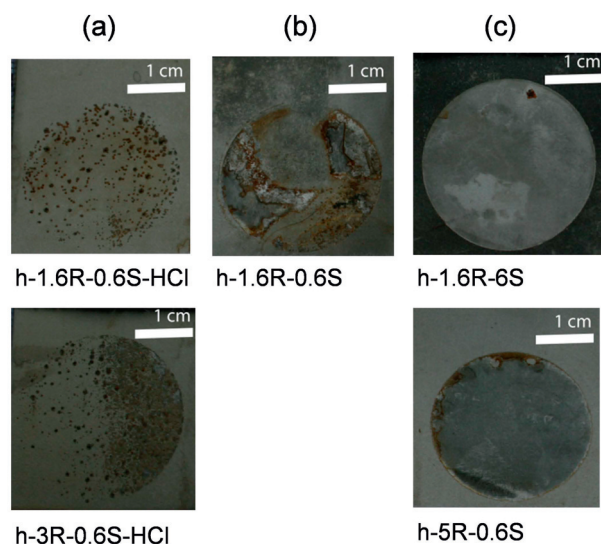


Figure 4.20: Appearance of the coatings after electrochemical polarization and electrolyte exposure. (a) displays localized corrosion spots in the coatings after electrolyte exposure, while (b) depicts a partially delaminated coating. The coatings in (c) are completely delaminated.

A low pore volume of gels of the acidic and neutral bond coats (Table 4.5) indicated dense coatings. A low pore volume in combination with a linearly chained structure could thus be an explanation for the observed corrosion resistance of the acidic bond coats.

4.7.2 Ageing resistance studies

Structural materials are typically exposed to climate changes. Ageing resistance testing of materials assists in determining a material's (or coating's) ability to withstand thermal cycling (winter vs. summer, etc.). In the PhD study, ageing resistance studies were conducted on combination coatings consisting of a top coat in addition to acidic hybrid bond coats, and the formulations tested are provided in Table 4.7. A bond coat consisting of one of the hybrid aminopropyl silane coatings listed in Table 4.7 was deposited on carbon steel substrates by dip coating. A subsequent top coat of polyaspartic paint was applied to dry bond coated carbon steel substrates. A scribe ($2 \cdot 32 \text{ mm}^2$) was introduced in these bond coat-top coat combination coatings, and they were then exposed to ageing resistance testing, which constituted a thermal cycling in alternate salt fog and UV environments for five weeks.

Table 4.7: Formulation of the coating combinations used in the ageing resistance studies.

Bond coat	Top coat	Thickness, μm
-	Polyaspartic paint	104 ± 12
h-1.6R-0.6S-HCl	Polyaspartic paint	119 ± 12
h-3R-0.6S-HCl	Polyaspartic paint	93 ± 4.5

Figure 4.21 shows coated substrates prior to (Figure 4.21 (a)), and after (Figure 4.21 (b)-(d)) ageing resistance testing. Figure 4.21 (c) and (d) provide examples of a bad and good coating, respectively, with regards to corrosion protection. The bad coating consisted of the top coat alone, while the good coating was an acidic bond coat-top coat combination coating. The improved corrosion resistance offered by the combination coatings compared to the top coat alone is further elaborated in Figure 4.21 (e), which shows the scribe creep corrosion. The scribe creep corrosion displayed the total width (over and beneath the scribe) of corrosion on the steel substrate after the ageing resistance test. After five weeks of thermal cycling, no significant corrosion around the scribe was detected in the combination coatings.

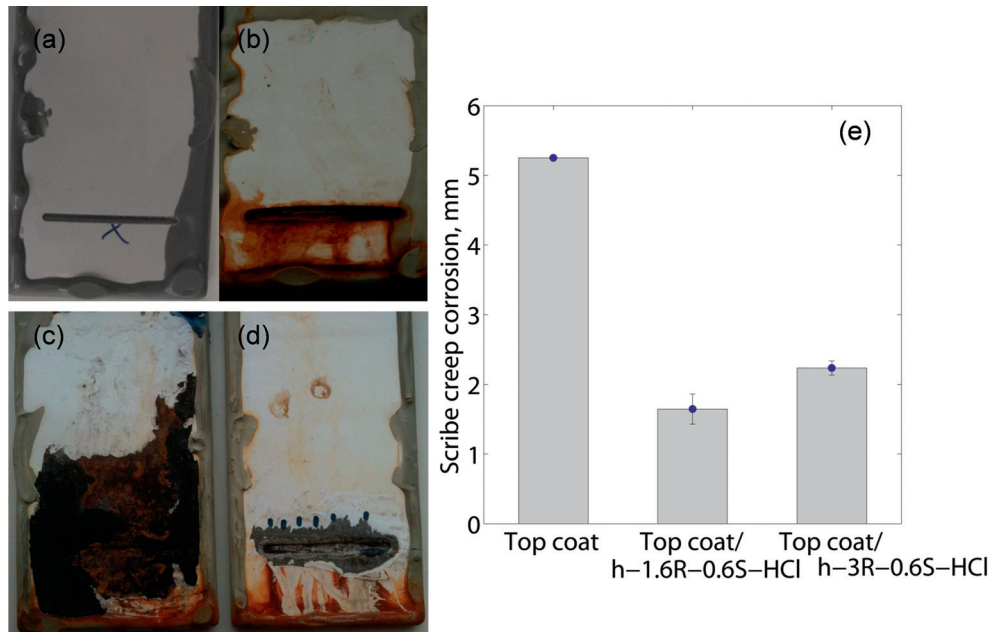


Figure 4.21: Example of the appearance of (a) a typical coating sample prior to ageing resistance exposure, (b) a general appearance of the samples after exposure, (c) example of a bad coating (top coat alone), (d) a good coating (acidic bond coat-top coat) and (e) scribe creep corrosion of the coating combinations after ageing resistance exposure.

4.7.3 Summary of the corrosion protective properties of the hybrid aminopropyl silane-based coatings

Electrochemical and ageing resistance (salt spray and thermal cycling) studies provided evidence that acidic hybrid bond coats alone could offer some protection against corrosion of steel, but as these coatings corroded in localized spots, long-term protection was not obtained. However, a significant corrosion protection was observed when combination coatings consisting of acidic bond coat and a polyaspartic top coat were applied. Weathering and thermal cycling for five weeks rendered the steel almost uncorroded. The corrosion resistant properties of the combination coatings could be ascribed to the excellent bonding of the silane-based coating to the steel. The role of a silane-based bond coat on metals is to promote adhesion, which has previously been documented by several authors [61, 62, 131, 132].

4.8 Prevention of wax deposition by hybrid aminopropyl silane-based coatings

The study with respect to wax deposition was conducted in a pilot tank, which contained four baffles mounted on a propeller/rotating device. As part of the study, this tank was filled with a test fluid, which was a mixture of n-decane and n-tetracosane with carbon numbers of 10 and 24, respectively. Furthermore, the carbon steel (St52) baffles were either dip coated in a neutral hybrid aminopropyl silane-based sol, h-1.6R-6S, or they remained bare. The parameters that were studied included test duration (15, 30 or 60 min) and propeller velocity (150 or 250 rpm). The wax deposition was then evaluated with respect to the amount of tetracosane that precipitated from the test fluid and deposited on the baffle wall. A detailed description of the study and the set-up of the wax deposition is provided in the Appendix. Figure 4.22 shows the average amount of tetracosane that deposited on the baffle wall during the tests, which demonstrates that less tetracosane deposited on the baffles coated with the hybrid aminopropyl silane compared to the baffles with bare carbon steel.

One important aspect that is worth mentioning is that while more tetracosane deposited on the bare carbon steel baffles with increased duration of the trial, the deposits that formed on the baffles coated with the hybrid aminopropyl silane remained constant regardless of the duration. One plausible explanation is surface roughness. Generally, interfacial adhesion is promoted when the surface roughness increases [97]. The average roughness of the hybrid aminopropyl silane-based coating was low (0.60 nm, Table 4.6), and this low roughness would have prevented wax deposition. Furthermore, the wax deposited on the hybrid aminopropyl silane coated baffle was also easier to remove, which indicated poorer adhesion of the wax to the coating as opposed to the adhesion of the wax directly on the carbon steel baffle. This phenomenon was probably caused by the smooth surface that the hybrid aminopropyl silane provided, and thus a sloughing-type effect was observed.

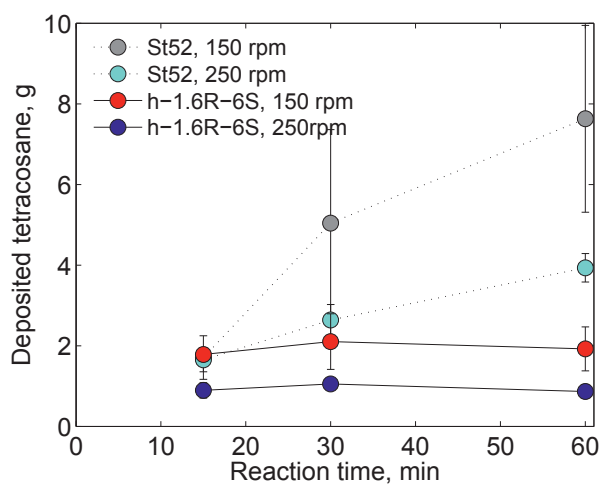


Figure 4.22: Average deposited tetracosane of four baffles constituting either bare St52 or St52 coated with h-1.6R-6S during a wax deposition study.

Chapter 5

Conclusions

Hydrolysis and condensation reactions of the hybrid aminopropyl silane-based sols have been studied, and the kinetics and the structure of the sols have been identified. The rate of the condensation reaction of γ -APS in 1-propoxy-2-propanol was demonstrated to be fast, and the rate increased with increasing water/silane ratio and temperature. The hydrolysis and condensation rates were shown to be suppressed by altering the pH of the hydrolysis water. Furthermore, the presence of T² and T³ units, which the aged sols were composed of, signified the presence of cage structures (T₈ or T₁₀) partly connected together. It was proposed that these cages were cross-linked in the neutral hyperstoichiometric sols due to the higher viscosity and T²/T³ ratio, whereas the acidic hypostoichiometric sol was proposed to be composed of cages in linear chains.

Smooth and homogeneous hybrid inorganic-organic silica-based coatings were synthesized by sol-gel chemistry using an aminopropyl silane as precursor at acidic or neutral hydrolyzing conditions. The inorganic part of the hybrid material caused the coatings to be thermally stable up to 350 °C. Gels of the hybrid aminopropyl silane-based sols displayed a low pore volume and a low surface area. The coating thickness was in the range 0.17-4.1 μm with roughness in the nm range. The thickness and the roughness of the aminopropyl silane-based coatings could be tailored depending on the water/silane ratio. Delamination during dry abrasion was less pronounced in the coatings prepared at acidic hydrolysis conditions compared to coatings of similar thickness prepared at neutral hydrolysis conditions. The coatings displayed hydrophobic character as demonstrated by the wetting of liquid pentadecane. Furthermore, a general observation led to the assumption that higher water/silane ratios, R, would yield thinner coatings with a higher sol viscosity for a given solvent/silane ratio, S. Conversely, lower water/silane ratios should provide thicker coatings. In addition, it was proposed that higher solvent/silane ratios should result in thin, abrasion resistant coatings with a low sol viscosity.

The ability of γ -APS-based bond coats to improve the anti-corrosion performance of carbon steel has been presented. Furthermore, the γ -APS-based bond coats displayed good adhesion towards the carbon steel substrates. In addition, the corrosion protective effect of the γ -APS-based bond coats behaved differently for the acidic and neutral bond coats. Whereas the γ -APS-based acidic bond coats significantly improved corrosion protection of carbon steel as identified by a reduction in the

current density in the anodic region, the neutral bond coats did not offer any protection from corrosion of the carbon steel in the anodic region. However, localized corrosion spots were observed in the acidic bond coats after the test. Acidic bond coats alone were thus considered insufficient for long-term corrosion protection of carbon steel. Nevertheless, the acidic bond coat-top coat combination coatings were able to provide long-term protection as was demonstrated by the ageing resistance studies.

The PhD study has shown that the fabrication of hybrid inorganic-organic amino-propyl silane-based coatings on steel is feasible. However, for optimal performance with respect to anti-corrosion and dry abrasion resistance, further modification of the coatings is required. Even though more optimized systems, such as the use of a larger fraction of amino groups for corrosion protection, remains to be studied, it is believed that further modification of organofunctional silanes will enable long-term substrate protection.

Chapter 6

Outlook

With regards to the hydrolysis and condensation of γ -APS, ^{29}Si NMR has shown that acidic sols are able to slow down the rate of the condensation reaction during the sol synthesis. To better understand the hydrolysis and condensation reactions which occur in γ -APS-derived sols, a non-functionalized alkoxide such as methyl triethoxysilane should be studied by ^{29}Si NMR and FTIR, and the rheological properties would determine the degree of cross-linking in the sol. pH-adjustment of methyl triethoxysilane with HCl will enable understanding of the hydrolysis and condensation reaction mechanisms which occur without presence of the very basic amino group in γ -APS. Furthermore, the effect of different molar ratios of water and silane of acidified γ -APS-derived sols on the hydrolysis and condensation reactions should be studied. The influence of the amount of solvent on the hydrolysis and condensation reaction rates of γ -APS-derived sols should be pursued.

Corrosion resistant coatings are believed to originate from a high content of amino groups in addition to being dense. Thus when regarding corrosion protection of steel, the possibility of increasing the amount of amino groups in the alkoxy silane should be pursued. The combination of bis-silane functionalized with amino groups should also be investigated as a potential method of improving the corrosion protection of steel. Furthermore, dense coatings are fabricated with longer carbon chains, and coatings with a larger organic fraction should be evaluated.

With respect to prevention of wax deposition, superhydrophobic coating surfaces with low surface energy need to be addressed. Low surface tension can be achieved by increasing the organic content in the hybrid inorganic-organic coating. Alternatively, fluorination (low surface energy) should be able to provide optimal surface tension properties of coatings on steel. In order to make these coatings industrially applicable, pressure studies also need to be addressed. Furthermore, the coatings also have to be able to withstand rough handling and thus should have good abrasion resistant properties. Abrasion is most likely the main obstacle to hybrid coatings as the main coat due to a reduction in hardness of the coating when the organic content in the hybrid material is increased. Thus abrasion resistant coatings, which can withstand great pressure and temperature variations/gradients, are required.

The polarization trials conducted as part of the thesis work disclosed limited long-term corrosion protection of γ -APS-derived coatings on steel. Nevertheless, the hybrid coatings displayed excellent corrosion protection properties as bond coats

with a polyaspartic paint as top coat. Bond coat (primer)-top coat combination coatings are familiar to the coating industry, and the use of γ -APS (silane-based primer solutions) as primer has long been utilized. However, the use of hybrid silane-based coatings as the main coat needs further work before this technology can be commercialized.

The present work has shown a potential for developing metal coatings based on hybrid inorganic-organic sol-gel technology. The results have still shown that the technology is in its infancy, and that further optimization is necessary in order to develop coatings which could be commercialized.

Chapter 7

References

- [1] Oljedirektoratet. Faktaheftet 2012. Online, 2012.
- [2] R. Venkatesan and H. S. Fogler. Comments on analogies for correlated heat and mass transfer in turbulent flow. *Aiche J.*, 50(7):1623–1626, 2004.
- [3] D. Merino-Garcia and S. Corraera. Cold flow: A review of a technology to avoid wax deposition. *Pet. Sci. Technol.*, 26(4):446–459, 2008.
- [4] R. Hoffmann and L. Amundsen. Single-phase wax deposition experiments. *Energy Fuels*, 24(2):1069–1080, 2010.
- [5] C. Martos, B. Coto, J. J. Espada, M. D. Robustillo, J. L. Peña, and D. Merino-Garcia. Characterization of Brazilian crude oil samples to improve the prediction of wax precipitation in flow assurance problems. *Energy Fuels*, 24(4):2221–2226, 2010.
- [6] M. A. San-Miguel and P. M. Rodger. The effect of corrosion inhibitor films on deposition of wax to metal oxide surfaces. *J. Mol. Struct-Theochem*, 506:263–272, 2000.
- [7] Q. Wang, C. Sarica, and T. X. Chen. An experimental study on mechanics of wax removal in pipeline. *J. Energ. Resour.-ASME*, 127(4):302–308, 2005.
- [8] B. Coto, C. Martos, J. J. Espada, M. D. Robustillo, J. L. Peña, and S. Gómez. Assessment of a thermodynamic model to describe wax precipitation in flow assurance problems. *Energy Fuels*, 23(3):1294–1298, 2009.
- [9] M. Fukushima, E. Yasuda, H. Kita, H. Hyuga, K. Osumi, H. Kawabata, Y. Hoshikawa, and Y. Tanabe. Oil wettability and sliding properties of organic and inorganic hybrid coating films prepared from methyltriethoxysilane and various metal alkoxides. *J. Ceram. Soc. Jpn.*, 114(1330):580–582, 2006.
- [10] M. Qian, A. McIntosh Soutar, X. H. Tan, X. T. Zeng, and S. L. Wijesinghe. Two-part epoxy-siloxane hybrid corrosion protection coatings for carbon steel. *Thin Solid Films*, 517(17):5237–5242, 2009.

- [11] W. J. van Ooij, D. Zhu, V. Palanivel, J. A. Lamar, and M. Stacy. Overview: The potential of silanes for chromate replacement in metal finishing industries. *Silicon Chem.*, 3(1-2):11–30, 2006.
- [12] M.-A. Chen, X.-B. Lu, Z.-H. Guo, and R. Huang. Influence of hydrolysis time on the structure and corrosion protective performance of (3-mercaptopropyl)triethoxysilane film on copper. *Corros. Sci.*, 53(9):2793–2802, 2011.
- [13] V. H. V. Sarmiento, M. G. Schiavetto, P. Hammer, A. V. Benedetti, C. S. Fugivara, P. H. Suegama, S. H. Pulcinelli, and C. V. Santilli. Corrosion protection of stainless steel by polysiloxane hybrid coatings prepared using the sol-gel process. *Surf. Coat. Tech.*, 204(16-17):2689–2701, 2010.
- [14] F. Shan, G. Qi, and C. Liu. Corrosion protection and composition of galvanized steel substrates by bis-[3-(triethoxysilyl)-propyl]tetrasulfide and γ -aminopropyltriethoxysilane. *Adv. Mater. Res.*, 299-300:333–336, 2011.
- [15] R. Zandi Zand, K. Verbeken, and A. Adriaens. The corrosion resistance of 316L stainless steel coated with a silane hybrid nanocomposite coating. *Prog. Org. Coat.*, 72(4):709–715, 2011.
- [16] C. Sanchez, B. Julián, P. Belleville, and M. Popall. Applications of hybrid organic-inorganic nanocomposites. *J. Mater. Chem.*, 15(35-36):3559–3592, 2005.
- [17] J. D. Mackenzie and E. P. Bescher. Physical properties of sol-gel coatings. *J. Sol-Gel Sci. Technol.*, 19(1-3):23–29, 2000.
- [18] D. Wang and G. P. Bierwagen. Sol-gel coatings on metals for corrosion protection. *Prog. Org. Coat.*, 64(4):327–338, 2009.
- [19] D. Gallagher and T. A. Ring. Sol-Gel Processing of Ceramic Films. *Chimia*, 43:298–304, 1989.
- [20] Smoothpipe, The Research Council of Norway, Project No. 180038/S60.
- [21] F. Männle, T. R. Tofteberg, M. Skaugen, H. Bu, T. Peters, P. D. C. Dietzel, and M. Pilz. Polymer nanocomposite coatings based on polyhedral oligosilsesquioxanes: Route for industrial manufacturing and barrier properties. *J. Nanopart. Res.*, 13(10):4691–4701, 2011.
- [22] C. J. Brinker and G. W. Scherer. *Sol-Gel Science: The Physics and Chemistry of Sol-Gel Processing*. Academic Press, Inc., San Diego, 1990.
- [23] J. D. Wright and N. A. J. M. Sommerdijk. *Sol-Gel Materials Chemistry and Applications*. Taylor and Francis Books Ltd, Great Britain, 2003.
- [24] C. Sanchez and F. Ribot. Design of hybrid organic-inorganic materials synthesized via sol-gel chemistry. *New J. Chem.*, 18:1007–1047, 1994.

-
- [25] J. Wen and G. L. Wilkes. Organic-inorganic hybrid network materials by the sol-gel approach. *Chem. Mater.*, 8:1667–1681, 1996.
- [26] M. J. Paterson and B. Ben-Nissan. Multilayer sol-gel zirconia coatings on 316L stainless steel. *Surf. Coat. Technol.*, 86-87:153–158, 1996.
- [27] D. A. Lucca, M. J. Klopstein, R. Ghisleni, A. Gude, A. Mehner, and W. Datchary. Investigation of Sol-Gel Derived ZrO_2 Thin Films by Nanoindentation. *CIRP Annals: Manufacturing Technol.*, 53:475–478, 2004.
- [28] D. W. Schaefer. Polymers, Fractals, and Ceramic Materials. *Polym. Fractals Ceram. Mater.*, 243:1023–1027, 1989.
- [29] D. W. Richerson. *Modern Ceramic Engineering: Properties, Processing and Use in Design*. Marcel Dekker, Inc., second edition, 1992.
- [30] D. W. Johnson. Sol-gel processing of ceramics and glass. *Am. Ceram. Soc. Bull.*, 64(12):1597–1602, 1985.
- [31] R. Aelion, A. Loebel, and F. Eirich. Hydrolysis of ethyl silicate. *J. Am. Chem. Soc.*, 72(12):5705–5712, 1950.
- [32] G. B. Alexander. The Polymerization of Monosilicic Acid. *J. Am. Chem. Soc.*, 76(8):2094–2096, 1954.
- [33] R. K. Iler. *The chemistry of silica: solubility, polymerization, colloid and surface properties, and biochemistry*. Wiley, New York, 1979.
- [34] C. J. Brinker, K. D. Keefer, D. W. Schaefer, and C. S. Ashley. Sol-gel transition in simple silicates. *J. Non-Cryst. Solids*, 48(1):47–64, 1982.
- [35] C. J. Brinker, K. D. Keefer, D. W. Schaefer, R. A. Assink, B. D. Kay, and C. S. Ashley. Sol-gel transition in simple silicates II. *J. Non-Cryst. Solids*, 63(1-2):45–59, 1984.
- [36] J. C. Pouxviel, J. P. Boilot, J. C. Beloeil, and J. Y. Lallemand. NMR study of the sol/gel polymerization. *J. Non-Cryst. Solids*, 89(3):345–360, 1987.
- [37] A. J. Vega and G. W. Scherer. Study of structural evolution of silica gel using ^1H and ^{29}Si NMR. *J. Non-Cryst. Solids*, 111(2-3):153–166, 1989.
- [38] S. Y. Chang and T. A. Ring. Map of gel times for three phase region tetraethoxysilane, ethanol and water. *J. Non-Cryst. Solids*, 147-148(C):56–61, 1992.
- [39] K.C. Chen, T. Tsuchiya, and J.D. Mackenzie. Sol-gel processing of silica: I. the role of the starting compounds. *J. Non-Cryst. Solids*, 81(1-2):227–237, 1986.
- [40] E.J.A. Pope and J.D. Mackenzie. Sol-gel processing of silica: II. The role of the catalyst. *J. Non-Cryst. Solids*, 87(1-2):185–198, 1986.

- [41] F. Mammeri, E. LeBourhis, L. Rozes, and C. Sanchez. Mechanical properties of hybrid organic-inorganic materials. *J. Mater. Chem.*, 15:3787–3811, 2005.
- [42] C. J. Brinker. Hydrolysis and condensation of silicates: Effects on structure. *J. Non-Cryst. Solids*, 100(1-3):31–50, 1988.
- [43] G. W. Scherer. Recent progress in drying of gels. *J. Non-Cryst. Solids*, 147-148(C):363–374, 1992.
- [44] F. J. Boerio, L. Armogan, and S. Y. Cheng. the structure of γ -aminopropyltriethoxysilane films on iron mirrors. *J. Colloid Interface Sci.*, 73(2):416–424, 1980.
- [45] L.D. White and C.P. Tripp. Reaction of (3-Aminopropyl)dimethylethoxysilane with Amine Catalysts on Silica Surfaces. *J. Colloid Interface Sci.*, 232(2):400–407, 2000.
- [46] H. Schmidt, H. Scholze, and A. Kaiser. Principles of Hydrolysis and Condensation Reaction of Alkoxysilanes. *J. Non-Cryst. Solids*, 63(1-2):1–11, 1984.
- [47] B. M. Novak. Hybrid nanocomposite materials-between inorganic glasses and organic polymers. *Adv. Mater.*, 5(6):422–433, 1993.
- [48] U. Schubert and N. Hüsing. *Synthesis of Inorganic Materials*. Wiley-VCH, Weinheim, 2000.
- [49] H.-H. Huang, B. Orler, and G. L. Wilkes. Structure Property Behavior of New Hybrid Materials Incorporating Oligomeric Species Into Sol-Gel Glasses .3. Effect of Acid Content, Tetraethoxysilane-Content, and Molecular-Weight of Poly(dimethylsiloxane). *Macromolecules*, 20(6):1322–1330, 1987.
- [50] H.-H. Huang and G. L. Wilkes. Structure-property behavior of new hybrid materials incorporating oligomeric poly(tetramethylene oxide) with inorganic silicates by a sol-gel process - 3. effect of oligomeric molecular weight. *Polym. Bull.*, 18(5):455–462, 1987.
- [51] J. D. Mackenzie, Y. J. Chung, and Y. Hu. Rubbery ormosils and their applications. *J. Non-Cryst. Solids*, 147-148(C):271–279, 1992.
- [52] Y. Hu, Y. J. Chung, and J. D. Mackenzie. Gelation kinetics of an organically modified silicate. *J. Mater. Sci.*, 28(24):6549–6554, 1993.
- [53] J. D. Mackenzie, Q. Huang, and T. Iwamoto. Mechanical properties of ormosils. *J. Sol-Gel Sci. Technol.*, 7:151–161, 1996.
- [54] C. Sanchez, F. Ribot, and B. Lebeau. Molecular design of hybrid organic-inorganic nanocomposites synthesized via sol-gel chemistry. *J. Mater. Chem.*, 9:35–44, 1999.

-
- [55] C. Sanchez, F. Ribot, L. Rozes, and B. Alonso. Design of Hybrid Organic-Inorganic Nanocomposites Synthesized Via Sol-Gel Chemistry. *Mol. Cryst. Liq. Cryst. A*, 354(1):143–158, 2000.
- [56] C. Sanchez, L. Rozes, F. Ribot, C. Laberty-Robert, D. Grosso, C. Sassoie, C. Boissiere, and L. Nicole. "Chimie Douce": A land of opportunities for the designed construction of functional inorganic and hybrid organic-inorganic nanomaterials. *CR Chim.*, 13(1-2):3–39, 2010.
- [57] S. Hofacker, M. Mechtel, M. Mager, and H. Kraus. Sol-gel: A new tool for coatings chemistry. *Prog. Org. Coat.*, 45(2-3):159–164, 2002.
- [58] M. Pagliaro, R. Ciriminna, and G. Palmisano. Silica-based hybrid coatings. *J. Mater. Chem.*, 19(20):3116–3126, 2009.
- [59] S. Zheng and J-Li. Inorganic-organic sol gel hybrid coatings for corrosion protection of metals. *J. Sol-Gel Sci. Technol.*, 54:174–187, 2010.
- [60] M. Murakami, K. Izumi, T. Deguchi, A. Morita, N. Tohge, and T. Minami. SiO₂ Coating on Stainless Steel Sheets from CH₃Si(OC₂H₅)₃. *J. Ceram. Soc. Jpn.*, 97(1121):91–94, 1989.
- [61] M.-C. Brochier Salon and M. N. Belgacem. Competition between hydrolysis and condensation reactions of trialkoxysilanes, as a function of the amount of water and the nature of the organic group. *Colloid Surface A*, 366(1-3):147–154, 2010.
- [62] F. Beari, M. Brand, P. Jenkner, R. Lehnert, H. J. Metternich, J. Monkiewicz, and H. W. Siesler. Organofunctional alkoxy silanes in dilute aqueous solution: New accounts on the dynamic structural mutability. *J. Organomet. Chem.*, 625(2):208–216, 2001.
- [63] R. M. Pasternack, S. R. Amy, and Y. J. Chabal. Attachment of 3-(Aminopropyl)triethoxysilane on Silicon Oxide Surfaces: Dependence on Solution Temperature. *Langmuir*, 24(22):12963–12971, 2008.
- [64] M.-C. Brochier Salon, M. Abdelmouleh, S. Boufi, M. N. Belgacem, and A. Gandini. Silane adsorption onto cellulose fibers: Hydrolysis and condensation reactions. *J. Colloid Interface Sci.*, 289(1):249–261, 2005.
- [65] L. Bisticric, V. Volovsek, V. Dananic, and I. M. Sopic. Conformational stability and vibrations of aminopropylsilanol molecule. *Spectrochim. Acta, Part A*, 64:327, 2006.
- [66] R. Peña-Alonso, F. Rubio, J. Rubio, and J. Oteo. Study of the hydrolysis and condensation of γ -Aminopropyltriethoxysilane by FT-IR spectroscopy. *J. Mater. Sci.*, 42:595–603, 2007.

- [67] M.-C. Brochier Salon, G. Gerbaud, M. Abdelmouleh, C. Bruzzese, S. Boufi, and M. N. Belgacem. Studies of interactions between silane coupling agents and cellulose fibers with liquid and solid-state NMR. *Magn. Reson. Chem.*, 45(6):473–483, 2007.
- [68] M.-C. Brochier Salon, P.-A. Bayle, M. Abdelmouleh, S. Boufi, and M. N. Belgacem. Kinetics of hydrolysis and self condensation reactions of silanes by NMR spectroscopy. *Colloid Surface A*, 312(2-3):83–91, 2008.
- [69] V. Roche, F. X. Perrin, D. Gignes, F. Vacandio, F. Ziarelli, and D. Bertin. Tracking the state of γ -aminopropyltriethoxysilane from the sol state to the dried film state. *Thin Solid Films*, 518:3640–3645, 2010.
- [70] D. A. Loy, B. M. Baugher, C. R. Baugher, D. A. Schneider, and K. Rahimian. Substituent effects on the sol-gel chemistry of organotrialkoxysilanes. *Chem. Mater.*, 12(12):3624–3632, 2000.
- [71] A. A. El Hadad, D. Carbonell, V. Barranco, A. Jimenez-Morales, B. Casal, and J. C. Galvan. Preparation of sol-gel hybrid materials from γ -methacryloxypropyltrimethoxysilane and tetramethyl orthosilicate: Study of the hydrolysis and condensation reactions. *Colloid Polym. Sci.*, 289(17-18):1875–1883, 2011.
- [72] J. F. Brown, L. H. Vogt, and P. I. Prescott. Preparation and characterization of the lower equilibrated phenylsilsesquioxanes. *J. Am. Chem. Soc.*, 86(6):1120–1125, 1964.
- [73] P. Eisenberg, R. Erra-Balsells, Y. Ishikawa, J. C. Lucas, A. N. Mauri, H. Nonami, C. C. Riccardi, and R. J. J. Williams. Cagelike Precursors of High-Molar-Mass Silsesquioxanes Formed by the Hydrolytic Condensation of Trialkoxysilanes. *Macromolecules*, 33(6):1940–1947, 2000.
- [74] X. Zhang, L. Hu, D. Sun, and W. Zhao. Study of three-dimensional configurations of organic/inorganic hybrid nanostructural blocks: A quantum chemical investigation for cage structure of (γ -glycidoxypropyl)silsesquioxanes. *J. Mol. Struct.*, 872(2-3):197–204, 2008.
- [75] R. H. Baney, M. Itoh, A. Sakakibara, and T. Suzuki. Silsesquioxanes. *Chem. Rev.*, 95(5):1409–1430, 1995.
- [76] D. B. Cordes, P. D. Lickiss, and F. Rataboul. Recent developments in the chemistry of cubic polyhedral oligosilsesquioxanes. *Chem. Rev.*, 110(4):2081–2173, 2010.
- [77] M. Z. Asuncion and R. M. Laine. Fluoride Rearrangement Reactions of Polyphenyl- and Polyvinylsilsesquioxanes as a Facile Route to Mixed Functional Phenyl, Vinyl T₁₀ and T₁₂ Silsesquioxanes. *J. Am. Chem. Soc.*, 132(11):3723–3736, 2010.

-
- [78] T. Gunji, T. Shioda, K. Tsuchihira, H. Seki, T. Kajiwara, and Y. Abe. Preparation and properties of polyhedral oligomeric silsesquioxane-polysiloxane copolymers. *Appl. Organomet. Chem.*, 24(8):545–550, 2010.
- [79] Y. Kawakami. Structural control and functionalization of oligomeric silsesquioxanes. *React. Funct. Polym.*, 67(11 Spec. Iss.):1137–1147, 2007.
- [80] F. Ribot and C. C. Sanchez. Organically Functionalized Metallic Oxoclusters: Structurally Well-Defined Nanobuilding Blocks for the Design of Hybrid Organic-Inorganic Materials. *Comment Inorg. Chem.*, 20(4-6):327–371, 1999.
- [81] C. H. Li and G. L. Wilkes. The mechanism for 3-aminopropyltriethoxysilane to strengthen the interface of polycarbonate substrates with hybrid organic-inorganic sol-gel coatings. *J. Inorg. Organomet. Polym.*, 7(4):203–216, Dec. 1997.
- [82] M.A. Aegerter, R. Almeida, A. Soutar, K. Tadanaga, H. Yang, and T. Watanabe. Coatings made by sol-gel and chemical nanotechnology. *J. Sol-Gel Sci. Technol.*, 47:203–236, 2008.
- [83] Y. Wei, D. Jin, G. Wei, D. Yang, and J. Xu. Novel organic-inorganic chemical hybrid fillers for dental composite materials. *J. Appl. Polym. Sci.*, 70(9):1689–1699, 1998.
- [84] J.-M. Yang, C.-H. Lu, Y.-G. Hsu, and C.-H. Shih. Mechanical properties of acrylic bone cement containing PMMA-SiO₂ hybrid sol-gel material. *J. Biomed. Mater. Res.*, 38(2):143–154, 1997.
- [85] P. C. Hiemenz and R. Rajagopalan. *Principles of colloid and surface chemistry*. New York: Marcel Dekker, 3rd edition, 1997.
- [86] C. J. Brinker, A. J. Hurd, G. C. Frye, P. R. Schunk, and C. S. Ashley. Sol-gel thin film formation. *J. Ceram. Soc. Jpn.*, 99(1154):862–877, 1991.
- [87] G. W. Scherer. Theory of Drying. *J. Am. Ceram. Soc.*, 73(1):3–14, 1990.
- [88] M. Guglielmi, P. Colombo, and S. Zenezini. Influence of the H₂O Teos ratio on the preparation of SiO₂ thin coatings by the sol-gel dipping method. *Mater. Chem. Phys.*, 23(4):453–463, 1989.
- [89] I. Strawbridge and P. F. James. Thin silica films prepared by dip coating. *J. Non-Cryst. Solids*, 82(1-3):366–372, 1986.
- [90] I. Strawbridge and P. F. James. The factors affecting the thickness of sol-gel derived silica coatings prepared by dipping. *J. Non-Cryst. Solids*, 86(3):381–393, 1986.
- [91] M. Faustini, B. Louis, P. A. Albouy, M. Kuemmel, and D. Grosso. Preparation of sol-gel films by dip-coating in extreme conditions. *J. Phys. Chem. C*, 114(17):7637–7645, 2010.

- [92] F. Doumenc and B. Guerrier. Drying of a solution in a meniscus: A model coupling the liquid and the gas phases. *Langmuir*, 26(17):13959–13967, 2010.
- [93] M. Le Berre, Y. Chen, and D. Baigl. From convective assembly to Landau-Levich deposition of multilayered phospholipid films of controlled thickness. *Langmuir*, 25(5):2554–2557, 2009.
- [94] A. D. Wilson, J. W. Nicholson, and H. J. Prosser. *Surface Coatings*. Elsevier Applied Science Publishers Ltd., 1987.
- [95] A. B. Brennan and G. L. Wilkes. Structure-property behaviour of sol-gel derived hybrid materials: effect of a polymeric acid catalyst. *Polymer*, 32(4):733–739, 1991.
- [96] P. Jussila, H. Ali-Löytty, K. Lahtonen, M. Hirsimäki, and M. Valden. Effect of surface hydroxyl concentration on the bonding and morphology of amino-propylsilane thin films on austenitic stainless steel. *Surf. Interface Anal.*, 42(3):157–164, 2010.
- [97] T. A. Ring. *Fundamentals of Ceramic Powder Processing and Synthesis*. Academic Press, Inc., San Diego, 1996.
- [98] T. J. Chotard, A. Smith, D. Rotureau, D. Fargeot, and C. Gault. Acoustic emission characterisation of calcium aluminate cement hydration at an early stage. *J. Eur. Ceram. Soc.*, 23(3):387–398, 2003.
- [99] C.J. Brinker, G.W. Scherer, and E.P. Roth. Sol \rightarrow gel \rightarrow glass: II. Physical and structural evolution during constant heating rate experiments. *J. Non-Cryst. Solids*, 72(2-3):345–368, 1985.
- [100] D. Raps, T. Hack, J. Wehr, M. L. Zheludkevich, A. C. Bastos, M. G. S. Ferreira, and O. Nuyken. Electrochemical study of inhibitor-containing organic-inorganic hybrid coatings on AA2024. *Corros. Sci.*, 51(5):1012–1021, 2009.
- [101] V. Subramanian and W. J. Van Ooij. Effect of the Amine Functional Group on Corrosion Rate of Iron Coated with Films of Organofunctional Silanes. *Corrosion*, 54(3):204–215, 1998.
- [102] W. Trabelsi, L. Dhouibi, E. Triki, M. G. S. Ferreira, and M.F. M. F. Montemor. An electrochemical and analytical assessment on the early corrosion behaviour of galvanised steel pretreated with aminosilanes. *Surf. Coat. Tech.*, 192(2-3):284–290, 2005.
- [103] B. C. Dave, X. Hu, Y. Devaraj, and S. K. Dhali. Sol-gel-derived corrosion-protection coatings. *J. Sol-Gel Sci. Technol.*, 32(1-3):143–147, 2004.
- [104] X. M. Zhang, J. J. Wang, C. M. Liu, and Y. J. Ying. Effects of cure temperature on corrosion property of vinyltriethoxysilane films on carbon steel surfaces. *Appl. Mech. Mater.*, 52-54:1947–1952, 2011.

-
- [105] T. P. Chou, C. Chandrasekaran, S. J. Limmer, S. Seraji, Y. Wu, M. J. Forbess, C. Nguyen, and G. Z. Cao. Organic-inorganic hybrid coatings for corrosion protection. *J. Non-Cryst. Solids*, 290(2-3):153–162, 2001.
- [106] T. P. Chou, C. Chandrasekaran, S. Limmer, C. Nguyen, and G. Z. Cao. Organic-inorganic sol-gel coating for corrosion protection of stainless steel. *J. Mater. Sci. Lett.*, 21:251–255, 2002.
- [107] T. P. Chou, C. Chandrasekaran, and G. Z. Cao. Sol-gel-derived hybrid coatings for corrosion protection. *J. Sol-Gel Sci. Technol.*, 26(1-3):321–327, 2003.
- [108] Y. Castro, B. Ferrari, R. Moreno, and A. Durán. Corrosion behaviour of silica hybrid coatings produced from basic catalysed particulate sols by dipping and EPD. *Surf. Coat. Tech.*, 191(2-3):228–235, 2005.
- [109] A. Pepe, P. Galliano, M. Aparicio, A. Durán, and S. Ceré. Sol-gel coatings on carbon steel: Electrochemical evaluation. *Surf. Coat. Tech.*, 200(11):3486–3491, 2006.
- [110] J.-M. Yeh, C.-J. Weng, W.-J. Liao, and Y.-W. Mau. Anticorrosively enhanced PMMA-SiO₂ hybrid coatings prepared from the sol-gel approach with MSMA as the coupling agent. *Surf. Coat. Tech.*, 201(3-4):1788–1795, 2006.
- [111] N. Kumar, A. Jyothirmayi, K.R.C. Soma Raju, and R. Subasri. Effect of functional groups (methyl, phenyl) on organic-inorganic hybrid sol-gel silica coatings on surface modified SS 316. *Ceram. Int.*, 2012. <http://dx.doi.org/10.1016/j.ceramint.2012.05.040>.
- [112] D. Zhu and W. J. van Ooij. Corrosion protection of AA 2024-T3 by bis-[3-(triethoxysilyl) propyl]tetrasulfide in sodium chloride solution. Part 2: Mechanism for corrosion protection. *Corros. Sci.*, 45(10):2177–2197, 2003.
- [113] B. Chico, D. De La Fuente, M. L. Pérez, and M. Morcillo. Corrosion resistance of steel treated with different silane/paint systems. *J. Coat. Technol. Res.*, 9(1):3–13, 2012.
- [114] Y.-S. Li and A. Ba. Spectroscopic studies of triethoxysilane sol-gel and coating process. *Spectrochim. Acta, Part A*, 70:1013–1019, 2008.
- [115] P. C. Banerjee and R.K. S. Raman. Electrochemical impedance spectroscopic investigation of the role of alkaline pre-treatment in corrosion resistance of a silane coating on magnesium alloy, ZE41. *Electrochim. Acta*, 56(11):3790–3798, 2011.
- [116] B. F. Towler, O. Jaripatke, and S. Mokhatab. Experimental Investigations of the Mitigation of Paraffin Wax Deposition in Crude Oil Using Chemical Additives. *Pet. Sci. Technol.*, 29(5):468–483, 2011.

- [117] H.-Y. Ji, B. Tohidi, A. Danesh, and A. C. Todd. Wax phase equilibria: Developing a thermodynamic model using a systematic approach. *Fluid Phase Equilibr.*, 216(2):201–217, 2004.
- [118] K. S. Pedersen and H. P. Rønningsen. Influence of wax inhibitors on wax appearance temperature, pour point, and viscosity of waxy crude oils. *Energy Fuels*, 17(2):321–328, 2003.
- [119] P. Singh, H. S. Fogler, and N. Nagarajan. Prediction of the wax content of the incipient wax-oil gel in a pipeline: An application of the controlled-stress rheometer. *J. Rheol.*, 43(6):1437–1459, 1999.
- [120] S. G. Johnsen, S. M. Hanetho, P. Tetlie, S. T. Johansen, M.-A. Einarsrud, I. Kaus, and C. R. Simon. Paraffin Wax Deposition Studies on Coated and Non-Coated Steel Surfaces. In *Heat Exchanger Fouling and Cleaning IX - 2011, Crete, Greece, June 06 - June 10*, 2011.
- [121] P. Singh, R. Venkatesan, H. S. Fogler, and N. R. Nagarajan. Morphological evolution of thick wax deposits during aging. *Aiche J.*, 47(1):6–18, 2001.
- [122] O. Adeyanju and L. Oyekunle. An experimental study of rheological properties of nigerian waxy crude oil. *Pet. Sci. Technol.*, 30(11):1102–1111, 2012.
- [123] H. S. Lee, P. Singh, W. H. Thomason, and H. S. Fogler. Waxy oil gel breaking mechanisms: Adhesive versus cohesive failure. *Energy Fuels*, 22(1):480–487, 2008.
- [124] P. Singh, R. Venkatesan, H. S. Fogler, and N. Nagarajan. Formation and aging of incipient thin film wax-oil gels. *Aiche J.*, 46(5):1059–1074, 2000.
- [125] A. Matzain, M. S. Apte, H.-Q. Zhang, M. Volk, J. P. Brill, and J. L. Creek. Investigation of paraffin deposition during multiphase flow in pipelines and wellbores - part 1: Experiments. *J. Energ. Resour.-ASME*, 124(3):180–186, 2002.
- [126] Z. Guozhong and L. Gang. Study on the wax deposition of waxy crude in pipelines and its application. *J. Pet. Sci. Eng.*, 70(1-2):1–9, 2010.
- [127] K. Paso, T. Kompalla, N. Aske, H. P. Rønningsen, G. Øye, and J. Sjöblom. Novel surfaces with applicability for preventing wax deposition: A review. *J. Disper. Sci. Technol.*, 30(6):757–781, 2009.
- [128] T. Nishino, M. Meguro, K. Nakamae, M. Matsushita, and Y. Ueda. The Lowest Surface Free Energy Based on $-CF_3$ Alignment. *Langmuir*, 15(13):4321–4323, 1999.
- [129] E. F. Hare, E. G. Shafrin, and W. A. Zisman. Properties of Films of Adsorbed Fluorinated Acids. *J. Phys. Chem.*, 58(3):236–239, 1954.

- [130] S. R. Culler, H. Ishida, and J. L. Koenig. The silane interphase of composites: Effects of process conditions on γ -aminopropyltriethoxysilane. *Polym. Composite.*, 7(4):231–238, 1986.
- [131] R. Bailey and J. E. Castle. XPS study of the adsorption of ethoxysilanes on iron. *J. Mater. Sci.*, 12(10):2049–2055, 1977.
- [132] S. Kranias, C. Bureau, D. P. Chong, V. Brenner, I. George, P. Viel, and G. Lecayon. Evidencing Intermolecular Effects with Core-Level Photoelectron Spectroscopy via the Accurate Density Functional Calculation of Core-Electron Binding Energies on Model Systems: γ -APS as a Test. *J. Phys. Chem. B*, 101(49):10254–10261, 1997.

Papers

Paper I: Structural Characterization of Hybrid Aminopropyl Silane-based Sols

Is not included due to copyright

Paper II: Synthesis and Characterization of Hybrid Aminopropyl Silane-based Coatings on Stainless Steel Substrates

Is not included due to copyright

Paper III: Corrosion Protective
Aminopropyl Silane-based Coatings on
Carbon Steel

Is not included due to copyright

Appendix

Paraffin Wax Deposition Studies on Coated and Non-Coated Steel Surfaces

PARAFFIN WAX DEPOSITION STUDIES ON COATED AND NON-COATED STEEL SURFACES

S.G. Johnsen¹, S.M. Hanetho², P. Tetlie¹, S.T. Johansen¹, M.A. Einarsrud², I. Kaus¹ and C.R. Simon¹

¹ SINTEF Materials and Chemistry, 7465 TRONDHEIM, NORWAY, E-mail: sverre.g.johnsen@sintef.no

² Norwegian University of Science and Technology, dept. of Mat. Sci. and Eng., 7491 TRONDHEIM, NORWAY

ABSTRACT

A novel cold baffle wax deposition (CoBWaD) reactor is developed for studying deposition from wax rich hydrocarbon liquids. The Reactor consists of a heated jacket, to maintain the bulk temperature of the test fluid, and four PVC baffles positioned perpendicular to the cylindrical vessel wall. The baffles have a section with an exchangeable cooled surface. Fouling may thus be studied at different solid surfaces, under variable heat transfer regimes. In addition, due to the wide range of impeller rotational velocities, Reynolds numbers in the range from laminar to highly turbulent are accessible. The apparatus is designed to enable easy and low-cost assessment of the effect of surface coatings, on paraffin wax fouling of cold surfaces.

Fouling results and observations are reported for a binary test-fluid consisting of n-decane (nC10) and n-tetracosane (nC24), on non-coated and coated steel surfaces, for different flowing conditions and exposure times.

Parameters affecting wax deposition in the CoBWaD apparatus were coating thickness (wall temperature/heat transfer), flow velocity, and surface properties. For one coating, tested in different thicknesses, the effect of thickness was more important than hydrophilicity. Evidence was given that the deposition rate-flow velocity relationship is non-monotonous. Furthermore, it was demonstrated that surface coatings may both inhibit and promote wax deposition. In addition aging effects were observed in the sense that the amount of deposits increased with time, and indications were given that the deposit layer wax content increased with time. Effects of temperature, pressure or test-fluid composition were not investigated.

INTRODUCTION

Petroleum wax crystals and precipitates in crude oil predominantly consist of n-paraffinic components. Wax crystallizes when changes in pressure and/or temperature result in super saturation. Decreased pressure will cause loss of light-end components, which act as natural solvents for the waxes, and decreased temperature gives a decreased solubility of wax molecules in the oil. Paraffin wax fouling of oil production pipelines is a costly and common problem in the petroleum industry. The wax crystallization poses three main problems, in the oil industry, higher viscosity,

higher yield stress for restarts after shut-in periods, and fouling of solid surfaces such as tubing, pipelines, tanks, process equipment and sucker rods.

In this paper, the focus is on wax fouling of cold surfaces due to decreased liquid temperatures close to the wall. Subsea gas and oil production pipelines may typically be exposed to water temperatures below the wax appearance temperature (WAT), giving crystal and agglomerate formation of wax particles in the bulk and potentially a wax deposition problem. The WAT is defined as the temperature at which wax precipitation takes place and the oil becomes cloudy. Several methods for establishing the WAT exist, (Lira-Galeana and Hammami, 2000), e.g. the standardized ASTM D2500 for petroleum oils and ASTM D3117 for distillate fuels, the cold finger method, viscometry, calorimetry, microscopy, and others. The pour point (PP) is defined as the temperature at which the oil ceases to flow.

In Figure 1 a schematic of the temperature profile of a waxy oil-cold wall system is shown; the temperature steadily increases from the cold side of the wall to the bulk of liquid; a solid, but porous, wax layer forms at the cold wall, and the solid wax layer surface is at the pour-point

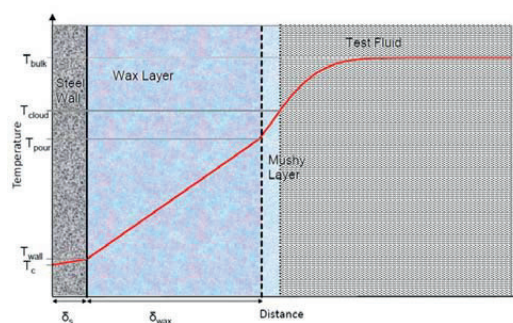


Figure 1. The temperature profile, from the coolant, through the steel wall, through a wax deposit layer, and through the thermal boundary layer of the test fluid. Close to the solid wax layer there is a mushy zone where the temperature is higher than the pour point, but lower than the wax appearance temperature.

temperature; between the PP and the wax appearance temperature there is a mushy zone of gel-like properties; outside the mushy zone, the wax is dissolved in the oil.

Fouling may occur either by wax crystal growth directly on the cold surface (crystallization fouling) or by solid wax particles, precipitating from a supersaturated fluid, being transported to the wall (particulate fouling). To mitigate wax precipitation/deposition related issues, several remediation techniques exist; removal of deposits by mechanical means (pigging) or fouling prevention by heating or chemical treatment (inhibitors) are common techniques, and surface treatment of the pipeline, e.g. by painting/coating, is a method that can provide improved insulation of the pipeline, reduced wall friction and reduced adhesive forces between the wall and the foulant. Finding economically feasible as well as environmentally acceptable solutions have become a key element to development of deep-water petroleum reserves. The literature includes a vast number of published papers on surface treatment, chemical treatment, paraffin thermodynamics, precipitation, transport processes and fouling. Recent reviews on paraffin wax topics include (Azevedo and Teixeira, 2003; Elsharkawy et al., 2000; Lira-Galeana and Hammami, 2000; Merino-Garcia and Corraera, 2008; Misra et al., 1995; Paso et al., 2009).

In this work an experimental apparatus is described. The apparatus is designed for testing coatings on solid surfaces, with respect to wax deposition, and experimental results are given from deposition experiments on different types of surfaces under various flowing and heat transfer conditions. The apparatus is an example of a batch experimental apparatus. Several authors (Hamouda, 1993; Hunt, 1962; Jorda, 1966; Newberry, 1984; Patton and Casad, 1970; Wu et al., 2002) have published their results from experiments in similar devices. Zougari et al. (2006) give a short review of the main conclusions of wax (and asphaltene) deposition studies in batch set-ups (as well as flow-through set-ups).

Wu et al. (2002) performed wax deposition experiments in a Cold Disk Deposition Apparatus using a binary test fluid consisting of n-tetracosane (nC24) and n-decane (nC10). The Wu et al. wax deposition apparatus consists of a cylindrical tank with an impeller in the middle. A cold disk, onto which wax is deposited, is embedded in the circular tank wall. Wu et al. report that the wax deposition results from their apparatus are comparable to those from pipe loop experiments, and that the deposition results using a binary decane-tetracosane mixture are comparable to North Sea crude oil experimental results.

The motivation for designing and building the CoBWaD reactor tank was mainly to have an apparatus where the fouling resistance of different internal surface treatments of oil pipelines, with respect to wax deposition, can be assessed. In addition it was desired to be able to study the heat flux and flow velocity dependency and the effect of turbulence on the wax deposition process. Key adjustable parameters of the wax deposition experiments are the flow velocity of the test fluid, the test-surface and test- fluid temperatures, in addition to the surface treatment

of the test-sections and the duration of the experiment. This study focused on varying the impeller velocity and experiment duration, as well as the surface coating.

THE EXPERIMENTAL APPARATUS

The reactor tank consists of a water heated stainless steel jacket and four PVC baffles positioned perpendicular to the cylindrical vessel wall, as shown in Figure 2. An impeller mounted in the middle of the tank, enables a wide range of flowing velocities and Reynolds numbers ranging from laminar to highly turbulent. The baffles have a section with an exchangeable cooled surface, as is shown in Figure 3. In the current wax deposition experiments coated and non-coated steel test-sections were employed. The test-sections are exposed to coolant flowing through a zigzag patterned cavity in the baffle, making it possible to adjust the test-section wall temperature. Fouling may thus be studied at different solid surfaces, under variable heat transfer regimes, and due to the symmetry of the apparatus and the positioning of the baffles it is possible to perform

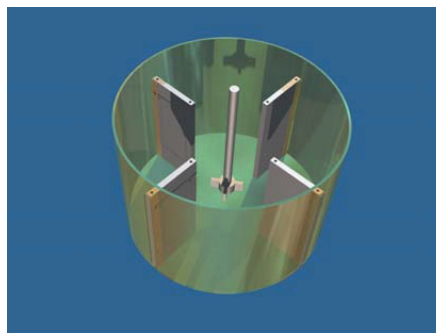


Figure 2. The CoBWaD apparatus, a cylindrical reactor tank with a water heated jacket, four water cooled baffles and a centrally positioned impeller.

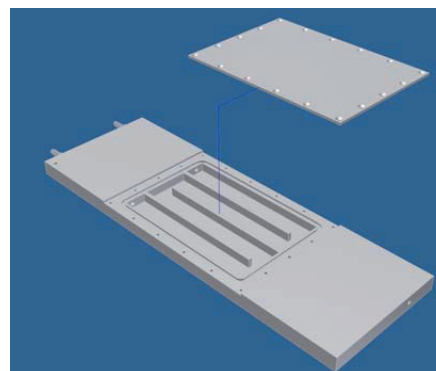


Figure 3. Schematic of a baffle with a water cooled, exchangeable test surface.

multiple screening tests in the same experimental run. The coolant temperatures are measured at the in- and outlets of all baffles, giving a measure of the heat transport through the test surface.

The inner tank diameter is 500 mm, and the height is 600 mm. The baffles are 20 mm thick, 170 mm wide and 500 mm tall, and are mounted perpendicular to and 10 mm apart from the vessel wall, to avoid direct contact with the heating jacket. The exchangeable steel test-sections are 3 mm thick, 170 mm wide and 240 mm tall, and they are attached in the middle of the baffles using 18 screws along the edge. A rubber o-ring prevents the coolant from contaminating the test-fluid. The test-section area directly exposed to the coolant measures 130 by 200 mm².

The impeller consists of four flat blades mounted vertically, in an x configuration, onto the circular axel. The Rotor blades are 20 mm thick and 200 mm tall, and the rotor diameter, including the blades and the axel, is 100 mm. The rotor- baffle spacing thus becomes 20 mm. The rotor is mounted 15 cm from the bottom of the vessel, such that it is aligned with the water cooled test sections. The impeller rotates so that the test-fluid is pushed towards the cooled test-section giving a high wall shear stress at the test surface.

Resting on top of the baffles, there is a lid to avoid splashing and to minimize evaporation of the test fluid. The apparatus is, however, not pressurized at the current stage. The baffles and the impeller are mounted in a submersible framework, thus it is easy to lift them in and out of the test fluid. Deposited material is easily and quickly removed from the test-sections by lifting the baffles out of the test fluid. Hence, additional accumulation of wax on the test-sections after the test is finished is minimized.

CFD SIMULATION OF THE COBWAD APPARATUS

Simulations of the internal flow of the CoBWaD geometry were performed in the commercially available CFD code Ansys Fluent to evaluate the heat transfer and flow velocities in the apparatus, as the impeller rotational velocity was varied. Due to the symmetry of the problem, only one quarter of the apparatus was modeled. A range of different impeller velocities were employed to study the effect on liquid velocity homogeneity and magnitude close to the test section, the wall heat flux and the homogeneity of temperature in the test-fluid.

Impeller velocities of 200, 400, 600, 800 and 1000 rpm were studied. Liquid velocities were recorded in a plane 1 cm outside the baffle, as indicated in Figure 4. The locations are 25 cm from the bottom, at 1) 10 cm, 2) 15 cm and 3) 20 cm distance from the centre axis. In Figure 5 it is seen how the test fluid velocity increases linearly for increasing impeller velocities in the three specific locations indicated by circles in Figure 4.

The simulations reveal that the flowing pattern does not change significantly by varying the impeller rotational velocity, although the velocity magnitude changes. In Figure 6, velocity vectors colored by velocity magnitude are shown for impeller rotational velocities of (a) 200 rpm and (b) 1000 rpm, and in Figure 7 velocity contours and vectors

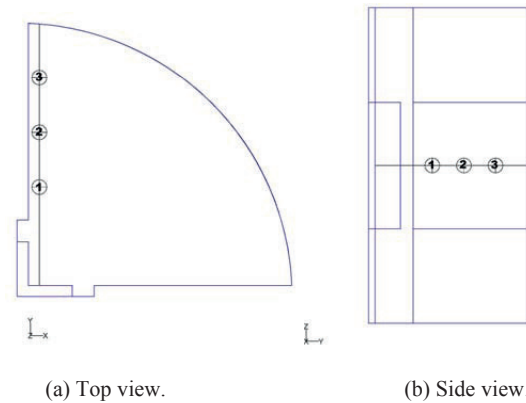


Figure 4. One quarter of the experimental apparatus. Simulation velocity measurement plane and locations.

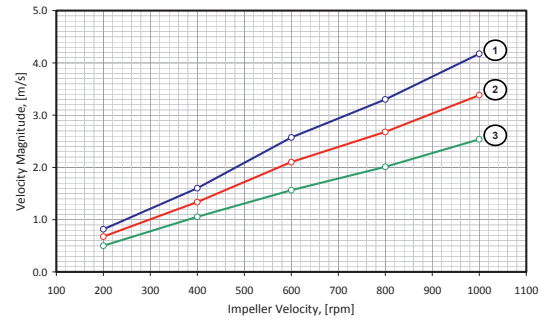


Figure 5. Test fluid velocity as a function of position and impeller velocity. The Velocities are taken 1 cm outside the cooled test section, as indicated in Figure 4.

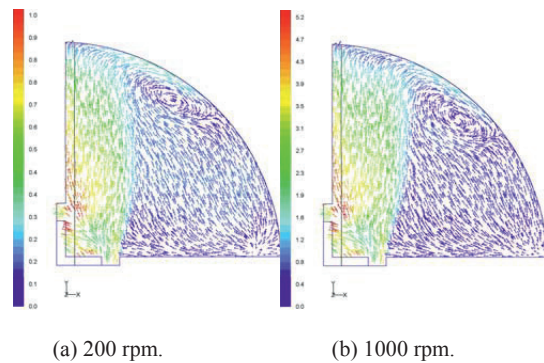


Figure 6. Simulation velocity vectors, in the horizontal symmetry plane, colored by velocity magnitude (m/s), for 200 and 1000 rpm impeller rotational velocities.

are drawn on the vertical plane 1 cm outside the test section. The flow pattern is essentially the same for the 200 and

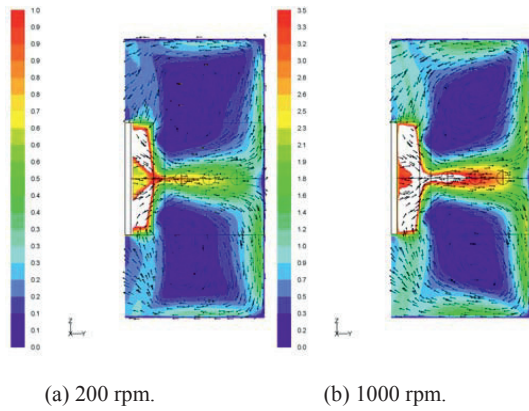


Figure 7. Simulation velocity contours (m/s) and directional vectors 1cm outside the test section, for 200 and 1000 rpm impeller rotational velocities.

1000 rpm models. It can be seen that although the flow direction along the test sections is fairly homogeneous, the velocity magnitude is much higher in the middle of the test section than along the edges. In the actual experiments, however, only occasional topographical variations in the deposit layers were observed, and no further investigation of the deposit layer thickness distribution was performed.

TEST-FLUID

Following Wu et al. (2002), the deposition experiments were performed with a binary test-fluid consisting of a paraffinic solvent, Sigma-Aldrich n-decane ($\text{CH}_3(\text{CH}_2)_8\text{CH}_3$) of Reagent Plus (99+ %) purity, and a paraffin wax solute, Aldrich n-tetracosane ($\text{CH}_3(\text{CH}_2)_{22}\text{CH}_3$) of 99 + % purity. The n-tetracosane content in the test-fluid was ca. 6 wt.-%, and the WAT was at ca. 15°C . In the following, we will refer to the tetracosane as wax and the decane as oil.

COATINGS

In addition to bare steel surfaces, three different coatings were tested. These are referred to as coatings 1,

2 and 3. Coatings 1 and 2 were commercially available coatings while Coating 3 was developed as part of this study. The coating thicknesses are reported in Table 1. The coatings were applied to st52 steel.

Coating 1 was a hydrophilic (80° contact angle) coating that was tested in two different thicknesses. In addition, the coating was modified by adding 3 wt.-% commercially available nano-particles, to make it hydrophobic (100° contact angle), and tested at an intermediate thickness. We will refer to these coatings as *1.thick*, *1.thin* and *1.mod*, respectively. The *1*-coatings were applied to the steel sections by paintbrush, resulting in an unpredictable thickness with a high macro roughness. The thickness was measured by an *Elcometer 256FN T2 Coating Thickness Gauge*.

Coating 2 was applied to the steel test-sections by spray by the manufacturer, giving a very smooth and uniform coating layer.

Coating 3 was an inorganic-organic hybrid coating based on (Aldrich) aminopropylsilane (Männle et al., 2005), with a water-silane ratio of 1.6 and a solvent-silane ratio of 6. The coating was applied to the test-sections by dipping into a bath of the aminopropylsilane based sol. The coating was thermally cured in air, at 160°C for three hours, and the coating thickness was measured by a *Veeco Dektak 150 profilometer*.

EXPERIMENTAL METHOD

During the deposition experiments, the test fluid was kept at a constant temperature above the WAT, by the heating jacket. The test-sections were kept at a low temperature by the cooling circuit. We have no knowledge of the actual wall temperature, but the coolant temperature was measured at both the in- and outlets of each baffle. The increase in temperature from the in- to the outlet is a measure of the amount of heat going from the test fluid through the test section wall.

The different phases of the experiments are;

1. *Heating phase*: The test-fluid is heated to a temperature well above the WAT ($\sim 20^\circ\text{C}$) under a high impeller velocity (750 rpm).
2. *Cooling phase*: Cooling of the baffles is commenced, at 8°C inlet temperature. The test-fluid temperature is reduced to the desired set point of $15.5\text{--}16^\circ\text{C}$ while maintaining the high impeller velocity, to avoid deposition.
3. *Deposition phase*: When stabilized at the desired test-fluid temperature, the impeller velocity is reduced to the desired value, to allow for deposition.
4. *Recovery phase*: After the specified deposition experiment duration, the baffles are lifted out of the test-fluid, and after a five minute period of evaporation/drainage, the deposits are collected from each baffle.

The deposits were harvested after three different deposition phase durations (exposure times), 60, 30 and 15 minutes. Initial bare steel attempts at 5 minutes exposure times were rejected; it was suspected that the deposits forming while stopping the impeller and lifting the baffles

Table 1. Coating thicknesses for the coatings applied in the wax deposition experiments.

Coating	Coating Thickness [μm]				
	Baffle 1	Baffle 2	Baffle 3	Baffle 4	Avg
Bare Steel	0	0	0	0	0
1.thin	66± 8	60± 20	68± 7		65
1.mod	281± 63	194± 23	169±16		215
1.thick	563±148	526±105	426±96		505
2	75± 5	75± 5	75± 5		75
3	0.4±0.01	0.4±0.01	0.4±0.01		0.4

out were comparable to the deposits forming during the actual deposition phase.

Experiments were performed with three different impeller velocities (350, 250 and 150 rpm), but the fouling of the coated surfaces, for the 350 rpm velocity, was minuscule and is reported only for bare steel.

In Figure 8, the temperature log from an experimental run is shown; the bulk test-fluid temperature is shown along with each baffle in- and outlet temperatures for all the experimental phases, for a specific impeller velocity. The different experimental phases can be recognized in the temperature plot.

EVALUATION OF THE DEPOSIT LAYER

To evaluate the amount of wax deposited, several methods have been suggested. Chen et al. (1997) give a review of existing methods; these include indirect measurements by pressure drop or temperature (heat transfer) measurements, their own method, the Liquid Displacement-Level Detection Method, as well as direct measurements by weighing. In addition a method using ultra-sound has been proposed by Andersen et al. (1997). Most of these are developed for pipe-flow experiments but could be adapted to the current experiments.

Indirect deposit layer thickness measurement by monitoring the baffle coolant outlet temperature, initially seemed like an attractive method, but the outlet temperature decreased too rapidly to reveal the transient behavior. In Figure 9 the outlet-inlet temperature difference of the four baffles are shown at the end of the cooling period (2), as the deposition phase (3) begins. Baffles 1-3 were coated while Baffle 4 was non-coated. It can be seen that this results in a higher outlet temperature for Baffle 4 than the others, due to the thermal insulation of the coating, during the cooling phase, where no deposits are forming. As the impeller velocity is reduced, and the deposit layer is allowed to form, the Baffle 4 temperature difference immediately drops and becomes close to the Baffle 1-3 outlet temperature differences. No further transient behavior of the temperature differences were observed. In agreement with the hypothesis of Figure 1, this indicates that a wax deposit layer immediately forms, so that the surface temperature is at the pour-point temperature, and that the combined thermal insulation effect of the deposit layer and the coating is identical for all baffles. It is therefore proposed that the transient behavior of the deposit layer is not with respect to thickness, but deposit layer wax-to-oil ratio. It is, however, noticed, from Figure 9, that the deposit layer thickness is varying strongly in time.

The deposits were removed from the test-sections by mechanical scraping, as shown in Figure 10. The harvested deposits were weighed and analyzed by gas chromatography (GC) to establish the amount of wax deposited.

EXPERIMENTAL RESULTS

The experimental results are reported as either amount of wax, in grams, accumulated on the test-sections or as an *average deposition rate* (amount of wax harvested divided

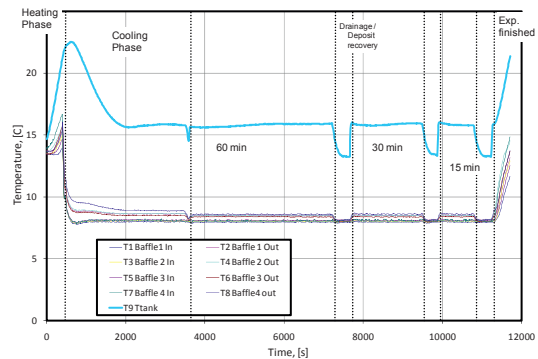


Figure 8. Temperature log from a wax deposition experiment. The different phases of the experiment are influencing the temperatures and are recognized in the temperature plot. The different phases are (1) an initial *heating phase* to dissolve any residual wax deposits in the apparatus; (2) a *cooling phase* to reach the target bulk temperature; (3) *wax deposition phases* (60min, 30min, 15min) separated by (4) *drainage/recovery phases*.

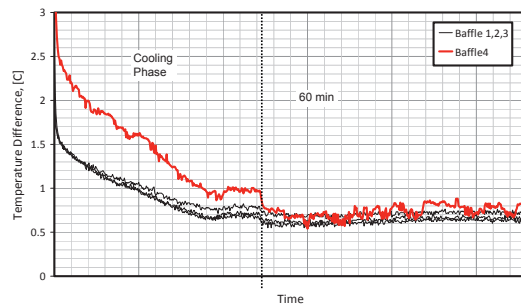


Figure 9. Outlet-inlet temperature difference versus time, during the *cooling phase* and 60 min *deposition phase* for baffles 1-3 (black) coated with *Coating 1.mod*, and non-coated bare steel Baffle 4 (red).



Figure 10. Mechanical removal of wax deposit layer from a cold bare steel test-section.

by exposure time), in grams per minute. The amount of wax was calculated based on the mass-fraction obtained by GC and the mass of deposits removed from each baffle.

Due to the high number of experiments performed and the high number of curves produced, only a few representative curves are presented here.

By visual inspection, the deposit layer forming on *Coating 2* had quite different characteristics from the deposit layers forming on the other surfaces. Whereas the deposit layer forming on bare steel or *Coatings 1* and *3* was moist and porous, the deposit layer forming on *Coating 2* seemed drier, denser and brittle. The GC analyzes revealed that the wax content in the *Coating 2* deposits were more than twice the amount in the other deposits.

Velocity Dependency

For the bare steel and *I*-coatings, the amount of deposits increased for decreasing impeller velocities, independent of the exposure time. *Coating 3* followed the same trend as the bare steel and *Coating 1*, but it was less affected by the exposure time, so that the longer the exposure time the better it performed, with respect to fouling prevention, compared to the others. For *Coating 2*, however, it was observed that the amount of wax deposits was increasing with the impeller velocity, as seen in Figure 11.

Exposure Time Dependency

For the bare steel and *I*-coatings it was evident that the amount of deposits increased for increasing exposure times, but *Coating 3* had a very weak exposure time dependency. *Coating 2* gave an increased amount of deposits, with time, for 250 rpm, but a decreased amount for 150 rpm.

Deposit Layer Aging

In the literature it is reported that the wax deposit layer is subject to an aging effect; e.g. Wu et al. (2002) demonstrate that the tetracosane content in the deposit layer increases with time. Singh et al. (2000) explain how the porous wax deposit structure, saturated with solvent, gradually hardens as wax molecules diffuse into the porous structure and oil counter diffuses out of the deposit layer, resulting in a time-dependent composition of the deposit.

In the current experiments it was seen that the influence of the flow velocity decreased with increasing exposure times, as the deposit amount seemed to approach a steady state. Furthermore it was seen that the GC-reported deposit wax content was increasing for increasing exposure times. Since we do not have control of the *drainage phase* evaporation and drainage of oil, however, the deposit layer wax content is uncertain.

Coating Thickness Dependency

Since *Coating 1* was tested in three different thicknesses, we had the opportunity to study the effect of the coating thickness on the deposition of wax. In general, one would expect that a thicker coating will give a higher wall temperature, resulting in a thinner thermal boundary layer and a thinner deposit layer; ultimately, a thick coating

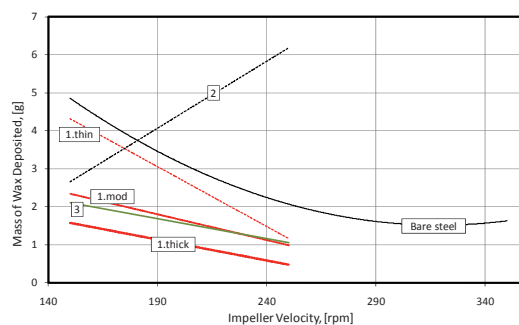


Figure 11. 2nd order polynomial trend-lines for measured amounts of wax deposit recovered after 30 minutes exposure time, as functions of impeller velocity (rpm), for bare steel (solid black), *I*-coatings (black), and *Coating 3* (green).

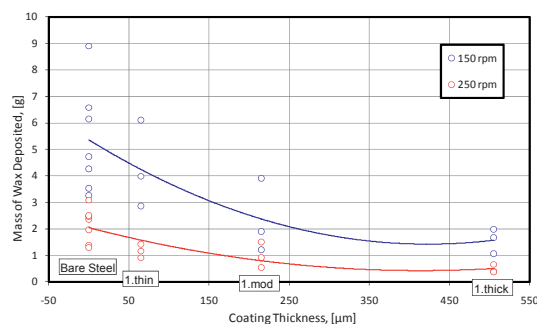


Figure 13. Measured amounts of wax deposit recovered, on bare steel and the *I*-coatings, with 2nd order polynomial trend-lines, after 30 minutes exposure time as functions of average coating thickness (μm), for different impeller velocities (rpm).

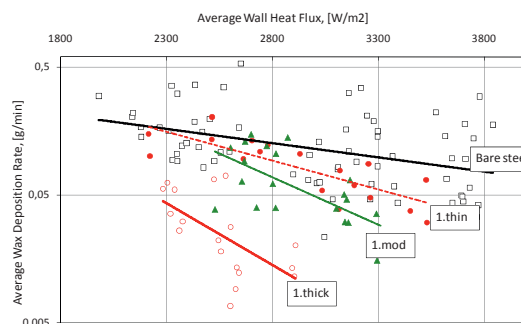


Figure 12. Measured average wax deposition rates, with exponential trend-lines, as functions of the average wall heat flux, for bare steel and the *I*-coatings.

may raise the wall temperature above the pour-point. Indeed this kind of behavior is shown in Figure 13. In fact, it seems that the coating thickness is more important, for *Coating 1* than the modification of the wetting properties.

Wall Heat Flux Dependency

The baffle inlet-outlet temperature increase is a measure of the heat-flux from the test-fluid to the coolant. An explanation for the apparent coating thickness dependency of the deposition rate might be that the wall heat flux is impeded by the coating layer, suggesting that the deposition rate is a function of the wall heat flux. In Figure 12 the average deposition rate is shown as a function of average wall heat-flux for the bare steel and *Coating 1* surfaces.

The wall heat flux depends on the bulk and wall temperatures, the over-all wall heat conductivity, and the flow velocity. Thus, the heat flux dependency of the deposition rate may be masked by these factors.

DISCUSSION

The CoBWaD reactor tank is a novel apparatus for studying wax fouling on cold surfaces. Although the apparatus is not directly comparable to field-scale pipe flow, the apparatus has some advantages over traditional flow-loop experiments; small liquid volumes are required; the test-surfaces are easily accessible and exchangeable; different turbulence regimes are easily accessible, and a wide range of Reynolds numbers is accessible at no additional cost; there is no need for extensive compressor power; good temperature control of the bulk test-fluid and walls is achieved; an experimental series is typically performed in a matter of hours; low building and maintenance costs. In the present design, the main disadvantages are that neither the flow velocity nor the heat transfer rate is homogeneous across the test-surfaces; we cannot measure the flow velocities; we cannot measure the wall temperature; and there is no possibility of performing pressurized experiments.

Ideally, to ensure experiment repeatability, each baffle should give the same amount of deposit, under the same conditions, and also give the same amount of deposit if the experiment is repeated. Currently, no repeatability studies has been done for baffles 1-3, but for all experimental runs, Baffle 4 was kept non-coated, for reference. Thus, the Baffle 4 data give insight into the repeatability. The scatter is significant, even between identical surfaces (bare steel), in the same experiment. Due to the turbulent nature of the experiment, reproducibility is not expected on individual experiment basis, but it is expected that a stable ensemble average will be established after a large number of experiments are performed. Although not enough experiments have currently been run, it can be seen that the cumulative moving average amount of deposited wax is fairly stable. As is seen in Figure 9, the outlet-inlet temperature difference, which is a direct measure of the heat transfer through the test-sections, is oscillating in a stepwise, erratic manner. It is believed that this is due to the variations in the over-all heat transfer coefficient, of the test-section, because of sudden re-entrainment of chunks of deposits. It is thus evident that the resulting "amount of wax deposited" is strongly dependent on the timing of the harvest relative to the oscillatory amount of wax deposited.

By visual assessment of the wax layer, it seemed that there was a difference in the way the wax layer was growing on the bare steel and the coated surfaces. Whereas the bare steel wax layer seemed quite homogeneous and smooth, patches of wax were growing on the coated surfaces. If the wax-wall adhesive forces are weak, wax molecules will not easily attach to the wall, to build the first layer of wax molecules. When some wax molecules have attached, however, more wax will readily grow on the existing wax deposit. Thus, patches of wax deposit may grow from separated nucleation sites. Eventually, the patches may cover the entire surface.

Net deposition rate will generally increase with increasing flow velocity until a point where the wall shear stress becomes so great that the re-entrainment rate becomes similar, in magnitude, to the gross deposition rate. After this point, the net deposition rate will decrease for increasing velocity, such that there is a critical velocity/shear stress for which a maximum net deposition rate exists. This point will, in general, depend on the surface properties (adhesive forces between deposit and wall), deposit material yield strength and thickness, and the temperature gradient. Thus, the critical velocity will depend on the surface treatment/coating employed, since this will affect both the deposit-wall adhesion force and the wall heat flux/temperature gradient. If *Coating 2* has a significantly higher critical velocity than the other test surfaces, such a non-monotonous behavior versus flow velocity may explain why the *Coating 2* deposit amount increases with impeller velocity, while the deposit amount decreases with velocity on the other test surfaces.

For *Coating 1* it seemed that the effect of coating thickness and thermal insulation was more important than the wetting property modification, but it is evident that surface properties also play a role. For the extremely thin *Coating 3*, for which the wall temperature is expected to be equal to that of bare steel, a significant improvement in the fouling resistance was observed, implying a strong effect of the surface properties, on the deposit growth.

The coating thickness affects the wall heat flux, and it was shown in Figure 12 that there is a relationship between the deposition rate and the wall heat flux. It is evident, however, that also the wall temperature is of importance, else the *1.thick* and *1.thin* curves in Figure 12, would have coincided. Future studies should consider the coating thickness and roughness as experimental parameters, and better control of thickness/roughness/wall temperature and heat flux should be enforced to yield conclusive results on the significance of surface properties.

The current studies have shown that factors directly affecting the deposit growth are flow velocity, coating thickness, and surface properties. It was seen that at high enough flow velocities, deposition was avoided, and indications were given that the deposition rate-flow velocity relationship is non-monotonous. The coating thickness will affect the wall temperature and the wall heat-flux. It was seen that there is a relationship between the deposition rate and the wall heat flux. Although the effect of bulk and wall temperatures have not been studied, it is reasonable to

assume that these are also important contributors to the deposition mechanism. Finally, it was seen that the surface properties may alter the deposition regime significantly, by both increasing and decreasing deposition. It was seen, however, that an initial improved fouling resistance is forfeit as soon as the deposit layer starts to grow, as *Coating 1.thin* had a delayed deposition problem, but caught up to the bare steel surface with time.

There are still many things we do not understand about the wax deposition mechanism and how the use of a coating may inhibit, or even promote, wax deposition. To what extent are thermal insulation, surface smoothness/roughness, and surface activation energy responsible for wax deposit reduction? Open questions are if the focus should be on hydrophilicity or hydrophobicity, or if other surface properties such as lipophobicity or oleophobicity are more relevant. Further questions concern the structure/ morphology of the wax deposits as parameters like flow velocity, wall heat flux or surface properties are changed, and how these affect the adhesion of the wax.

CONCLUSIONS

1. A novel apparatus has been designed to study wax deposition from wax-rich hydrocarbon oils onto cold surfaces when subject to a constant bulk temperature above the wax appearance temperature, and flow velocity. The test-surfaces are easily exchanged, so that deposition onto different types of surfaces may be studied.
2. Due to the stochastic nature of deposition under turbulent conditions, experimental repeatability is not to be expected on individual scale; a large number of experiments should be performed to establish ensemble averages.
3. Although measured data are subject to severe scatter, clear trends have been observed.
4. The current studies have shown that the factors directly affecting the deposit growth are flow velocity, coating thickness, and surface properties.
5. While an increasing deposition rate for increasing flow velocity was observed for the majority of the surfaces tested, one of the coatings had the opposite behavior. Furthermore, at high flow rates no deposition occurred on any of the surfaces. Thus, the deposition rate-flow velocity relationship is non-monotonous.
6. An aging effect has been observed in the sense that the accumulated amount of deposit increases with time. Preliminary results indicate that the amount of deposit approaches a steady state, and that the wax content in the deposit layer is increasing with time.

ACKNOWLEDGEMENTS

This work was funded by The Research Council of Norway, SINTEF Materials and Chemistry, and nine industrial companies. The authors thank the funding organizations.

REFERENCES

- Andersen, M. I., Isaksen, Ø. and Urdahl, O., 1997, Ultrasonic instrumentation for on-line monitoring of solid deposition in pipes, *SPE37437*.
- Azevedo, L. F. A. and Teixeira, A. M., 2003, A Critical Review of the Modeling of Wax Deposition Mechanisms, *Petroleum Science and Technology*, Vol. 21, pp. 393-408.
- Chen, X. T., Butler, T., Volk, M. and Brill, J. P., 1997, Techniques for Measuring Wax Thickness During Single and Multiphase Flow.
- Elsharkawy, A. M., Al-Sahhaf, T. A. and Fahim, M. A., 2000, Wax deposition from Middle East crudes, *Fuel*, Vol. 79, pp. 1047-1055.
- Hamouda, A. A., 1993, Wax Deposition Mechanism Under High-Pressure and in Presence of Light Hydrocarbons
- Hunt, E. B., 1962, Laboratory Study of Paraffin Deposition, *Journal of Petroleum Technology*, Vol. 14, pp. 1259-1269.
- Jorda, R. M., 1966, Paraffin Deposition and Prevention in Oil Wells *Journal of Petroleum Technology*, Vol. 18, pp. 1605-1612.
- Lira-Galeana, C. and Hammami, A., 2000, Wax Precipitation in Petroleum Fluids: A Review.
- Merino-Garcia, D. and Corraera, S., 2008, Cold Flow: A Review of a Technology to Avoid Wax Deposition, *Petroleum Science and Technology*, Vol. 26, pp. 446 - 459.
- Misra, S., Baruah, S. and Singh, K., 1995, Paraffin problems in crude oil production and transportation: A review, *SPE Production and Facilities*, Vol. 10, pp. 50-54.
- Männle, F., Simon, C., Beylich, J., Redford, K., Sommer, B., Hinrichsen, E., Andreassen, E., Olafsen, K. and Didriksen, T., 2005, Method for the Manufacture of Polybranched Organic/Inorganic Hybrid Polymers *PCT/NO2005/000126*.
- Newberry, M. E., 1984, Chemical Effects on Crude Oil Pipeline Pressure Problems *Journal of Petroleum Technology*, Vol. 36, pp. 779-786.
- Paso, K., Kompalla, T., Aske, N., Rønningsen, H. P., Øye, G. and Sjöblom, J., 2009, Novel Surfaces with Applicability for Preventing Wax Deposition: A Review, *Journal of Dispersion Science and Technology*, Vol. 30, pp. 757 - 781.
- Patton, C. C. and Casad, B. M., 1970, Paraffin Deposition from Refined Wax-Solvent Systems *SPE Journal*, Vol. 10, pp. 17-24.
- Singh, P., Venkatesan, R., Fogler, H. S. and Nagarajan, N., 2000, Formation and aging of incipient thin film wax-oil gels.
- Wu, C.-H., Wang, K.-S., Shuler, P. J. and Tang, Y., 2002, Measurement of Wax Deposition in Paraffin Solutions, *AIChE Journal*, Vol. 48, pp. 2107-2110.
- Zougari, M., Jacobs, S., Ratulowski, J., Hammami, A., Broze, G., Flannery, M., Stankiewicz, A. and Karan, K., 2006, Novel Organic Solids Deposition and Control Device for Live-Oils: Design and Applications, *Energy & Fuels*, Vol. 20, pp. 1656-1663.

